Czech Technical University in Prague
Faculty of Nuclear Sciences and Physical Engineering

Department of Physics

Radiation Monitoring Systems for the CMS Experiment

Master Thesis

Written by: Bc. David Gančarčík
Supervisor: Ing. Miroslav Myška, Ph.D.
Consultant: Anne Evelyn Dabrowski, Ph.D.
Year: 2021

České vysoké učení technické v Praze
Fakulta jaderná a fyzikálně inženýrská

Katedra Fyziky

Monitorovací systém radiace experimentu CMS

Diplomová práce

Autor:	Bc. David Gančarčík
Školitel:	Ing. Miroslav Myška, Ph.D.
Konzultant:	Anne Evelyn Dabrowski, Ph.D.
Akademický rok:	2021

ČESKÉ
VYSOKÉ UČENÍ
TECHNICKÉ V PRAZE

Fakulta jaderná
a fyzikálně
inženýrská

Břehová 7 115 19 Praha 1

Název katedry

Akademický rok: rrrr/rrrr

ZADÁNÍ BAKALÁŘSKÉ PRÁCE

Student: **Jméno Příjmení**

Studijní program: Název programu

Obor: Název oboru

Název práce česky: **Název česky**

Název práce anglicky: Name in English language

Pokyny pro vypracování:

1. Úkol 1
2. Úkol 2
3. Úkol 3
4. Úkol 4

Doporučená literatura:

[1]

[2]

[3]

[4]

[5]

[6]

[7]

[8]

Jméno a pracoviště vedoucího práce: **Supervisor Name**
Supervisor institution

Jméno a pracoviště konzultanta: **Consultant Name**
Consultant institution

Datum zadání bakalářské práce: Date of issue

Datum odevzdání bakalářské práce: Deadline

Doba platnosti zadání je dva roky od data zadání.

V Praze dne Date

Speciaization supervisor Name

Signature

Department director Name

Signature

Stamp

Dean Name

Signature

Prohlášení

Prohlašuji, že jsem svou diplomovou práci vypracoval samostatně a použil jsem pouze podklady (literaturu, projekty, SW atd.) uvedené v přiloženém seznamu.

V Praze dne .....

.....
Bc. David Gančarčík

Acknowledgement

I would like to express my sincere gratitude to Sophie Mallows, which taught me basically everything I know about simulation of radiation and FLUKA business. Her guidance was key for this thesis. Then I am deeply grateful to Ing. Miroslav Myška, Ph.D. for all those things he did for me and would not fit inside this short paragraph. Mainly for inspiration and for having my back over last three years. I would like to offer my special thanks to Anne Evelyn Dabrowski Ph.D. for being more guardian angel then my boss. I would like to also thank Arkady Lokhovitskiy and Igor Azhgirey for many useful comments on my work. I also want to thank Alexandre Ershov for helping with HF RadMon benchmark study and Andrei Gribushin for providing me data.

My thanks and appreciation also goes to my wife Tereza and my daughter Isabel for support during writing of this thesis. I am also grateful for my parent's help and support during whole studies (read: whole life). I also want to thank my sister Jane for helping me with submission of thesis to my university. Last but not least thank you goes to my 2L friends for pushing me forward.

Bc. David Gančarčík

Název práce:
Monitorovací systém radiace experimentu CMS

Autor: Bc. David Gančarčík

Studijní program: Aplikace přírodních věd
Obor:
Druh práce: Master Thesis

Vedoucí práce: Ing. Miroslav Myška, Ph.D.
Katedra fyziky
Fakulta jaderná a fyzikálně inženýrská, ČVUT v Praze
Konzultant: Anne Evelyn Dabrowski, Ph.D.
CMS Experiment, CERN

Abstrakt: Simulace radiačního pozadí klade požadavky na přístroje v experimentální hale, které musí být schopné odolat toku nabitých i neutrálních částic. Simulace ionizačního záření je prováděna s pomocí Monte Carlo generátorů. V této práci je použit program FLUKA. V něm jsou implementovány zjednodušené modely CMS detektoru i dalších komponent v podzemní hale. Cílem této práce je přispět do návrhů detektorů (TDR) v rámci projektu CMS BRIL provedenými simulacemi radiačního pole v místech, kde jsou detektory měřící toto pole v detektorové hale. Každý z detektorů monitoruje jinou skupinu částic nebo jinou část spektra, proto je důležité je strategicky umístit, na základě výsledků simulací a zkušeností z minulých běhů urychlovače. Dále jsou srovnány naměřená data detektorem HF RadMon, v letech 2017 a 2018 se simulacemi s geometrickým modelem detektoru pro Run 2.
Klíčová slova: CERN, CMS, BRIL, Simulace radiačního pozadí

Title:
Radiation Monitoring Systems for the CMS Experiment

Author: Bc. David Gančarčík

Abstract: Simulation of radiation background gives requirements on devices in the experimental hall, which have to withstand enormous fluxes of both charged and neutral particles. Simulation of the ionizing radiation relies on Monte Carlo generators, in this work FLUKA transport code is used. Here a simplified model of CMS experiment is implemented. Goal of this thesis is contribute to Technical Design Report, which is currently being finalised by CMS BRIL group. Each detector investigates different quantity or different part of spectra, so they have to be strategically distributed based on the simulation results and experience from previous Runs. Moreover, data measured in 2017 and 2018 from HF RadMon detector are benchmarked to simulations with CMS geometry model in Run 2.
Key words: CERN, CMS, BRIL, Radiation simulation

Contents

Introduction

The Standard Model, which is theory of particle physics was tested in last decades and its reliability was confirmed. But even through this a deviations could be observed in some usually rare processes. To investigate these a bigger and more powerful accelerators have to be build. The LHC is foreseeing a new upgrade to HL-LHC shortly. It will deliver much more collisions, because bunches of particles circulating around in accelerator will be almost twice more populated and beam will be squeezed to have smaller cross section. Leveling of luminosity goes together with background radiation in CMS cavern. Higher fluxes of particles in experimental hall can cause serious damage to detector sensitive elements. So it has to be estimated and taken into account in design of devices.

The first part of thesis introduces the CERN, the LHC and experiments based on it. Then the CMS detector is properly described in sense of describing CMS subdetectors and their working principles. Also the CMS BRIL group and its responsibilities are introduced. The second part deals with propagation of particles through the matter. It starts with describing of different particles interactions and then relevant quantities for describing of radiation field and its effect to material are defined. Short description of defects caused by ionization particles follows and then finally solving radiation transport problem with Monte Carlo generators is summed up. In this work particle transport code FLUKA is used and its description is at the end of second chapter. In the third chapter information about radiation monitors proposed for Phase 2 could be found.

Last part of the thesis aims to introduce general aspects of radiation field in CMS cavern and to describe changes between geometry versions for Run 2, Run 3 and Run 4. Main goal of this thesis should be characterising radiation field in proposed locations of radiation monitors in Run 3 and Run 4. Also energy spectra in these location should be found. Last aim is to benchmark simulations with measured data in Run 2.

Chapter 1

Experimental facility

1.1 CERN

The European Organisation for Nuclear Research was established in 1954 by the war destroyed European states after World War II. There were 12 member states from western Europe at the start of CERN. Later more states from all over the world joined the organisation. The Czech Republic became a member in 1993. Today, CERN has 23 member states, 6 associate member states, Cyprus, Estonia and Slovenia are in the pre-stage to membership and Japan, the Russian Federation, the United States, the European Union, JINR and UNESCO currently have observer status. The organisation must not work for militarily requirements and all results shall be generally available. The goal is to provide a wide range of particle accelerator facilities that allow a research of fundamental physics on world-class level and also connect people from all over the world and push limits of science and technology for the benefit of all.

The highest authority of the organization is the CERN Council. It is head of the organization that determines the policy in technical, scientific and administrative matters. It leads all strategic programmes and also approves the budget. Funding of CERN for the year 2020 is in Fig. 1.1. Director-General (currently Fabiola Gianotti) is appointed by the council. Each member state has two delegates for representation of government and national scientific interests. Equally, there is a single vote for every member state. The CERN Council meets usually four times a year. Scientific Policy Committee and Finance Committee assist the council. There is around $2,500$ staff members plus around $13,000$ users from all around the world who help with the preparation of experiments and analyse measured data. CERN is situated at Franco-Swiss border. To study sub-nuclear physics, one needs particles with energy higher than could be delivered from the decay of radioactive elements. Cosmic radiation has this ability, but the intensity is not sufficient for the charged particles (except widely used cosmic muons). Because of this fact, particle accelerators are needed.

Particle accelerators in CERN could be sorted to linear and circular ones. Currently there are three operating LINACs (LINear ACcelerators) at CERN, namely, LINAC2, LINAC3, LINAC4. The oldest active LINAC2 was built in 1978, as a substitution for LINAC1. It was able to deliver higher intensity beams then its forerunner. Protons come to LINAC2 from hydrogen bottle. Hydrogen passes through the stripping foil, where the electron is stripped and proton persists. Proton beam passes through the conductors charged by radio-frequency cavities. Small quadrupole magnets ensure the beam is tight. LINAC2 speed up protons to energy 50 MeV. LINAC3 was constructed inside the former tunnel of LINAC1 [1]. LINAC3 is the source of ions for the LHC (mainly lead, also might be substituted by xenon). It works on same principle as LINAC2, only the magnets focusing the beam needs to be more powerful. LINAC4, the key component for the HL-LHC (High-Luminosity Large Hadron Collider), will replace LINAC2 this year [2]. Instead of directly accelerating protons it uses H^- as a source. Accelerating has four stages, it starts with radio-frequency quadrupole, then drift tube linacs are used, coupled-cavity drift tube linacs come after that and finally Pi-mode structures boost protons to energy 160 MeV. Hydrogen ions are stripped of their electrons during injection to PSP (Proton Synchrotron Booster). CLEAR is a research development study accelerator for existing and possible future machines at CERN [3].

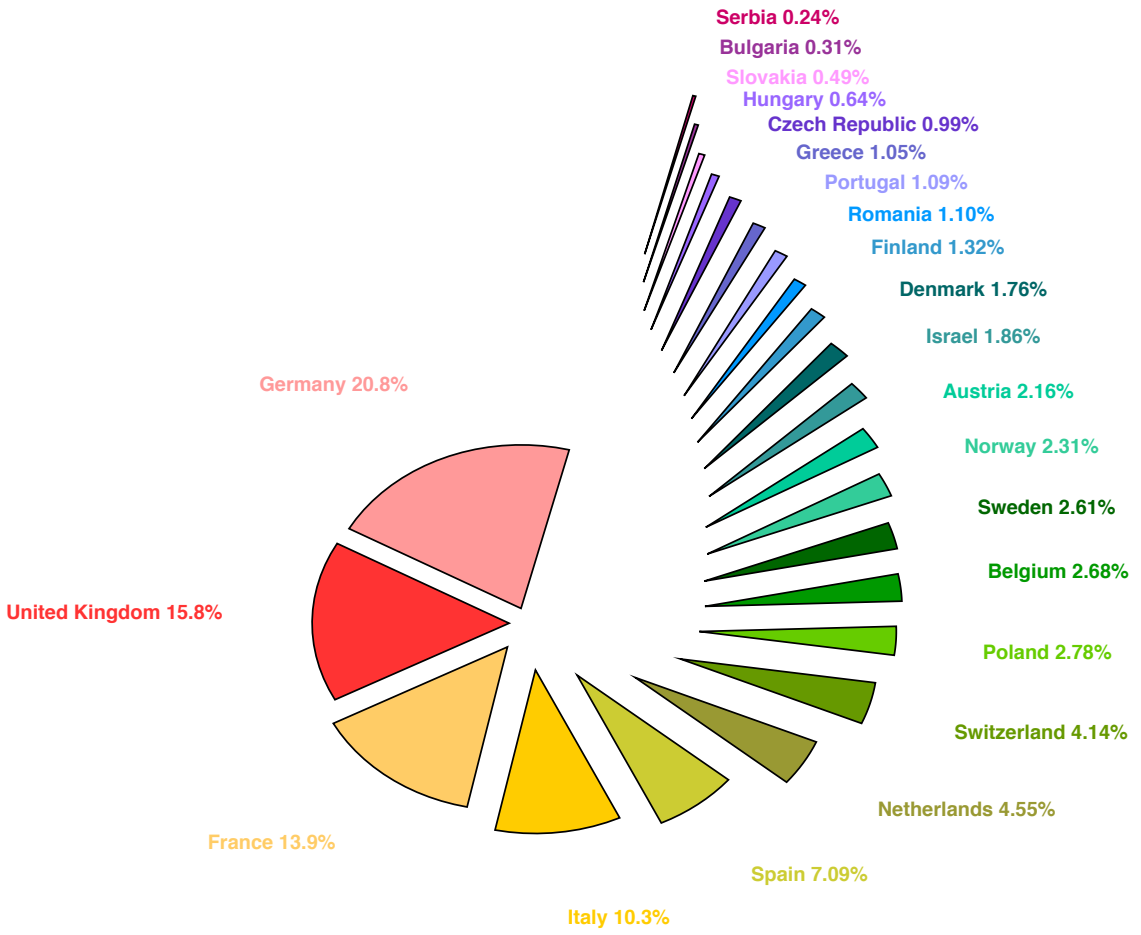

Figure 1.1: 2020 annual contributions to CERN budget.

The Proton Synchrotron Booster (PSB) is made up of four synchrotron rings. It is filled by protons from the LINAC2 at 50 MeV and it boosts them to energy 1.4 GeV. The PSB allows the PS (Proton Synchrotron) to accept over 100 times more protons compared to the situation before PSB was build and the proton beams were injected straight to the PS from LINACs. The PS at CERN facility is a circular proton or ion synchrotron, that has been working since 1959 [4]. With a radius of 100 m, the PS has 277 room-temperature electromagnets, including 100 dipoles to bend the particles. It could accelerate many types of particles (protons, alpha particles, oxygen or sulphur nuclei, electrons, positrons, or anti-protons). Using a neutrinos produced by a proton beam from PS, the GARGAMELLE experiment discovered the weak neutral current and thus indirectly proved the existence of a neutral particle to carry the weak fundamental force in 1973 [5]. The LEIR (Low Energy Ion Ring) was first proposed in 1993 as an extension of a then-existing machine LEAR (Low Energy Antiproton Ring) [6]. It receives long pulses of lead ions from LINAC3 and transforms them into the short, dense bunches suitable for injection in to the PS (Proton Synchrotron). The AD (Antiproton Decelerator) is a unique machine producing anti-protons with low energy. It uses the beam from PS and smashes it into a block of metal [7]. This induces many particles including anti-protons, which are separated. ELENA is a ring dedicated to slow down anti-protons gained from AD. Those decelerated anti-protons are forced to mix with positrons to make an anti-hydrogen. Goal is to perform anti-hydrogen spectroscopy and explore the effect of the gravitational force on matter and the antimatter.

The Super Proton Synchrotron (SPS) is the 7 km long circular accelerator active since 1976. Particles from the PS are filled to SPS, where they are accelerated to the energy of 450 GeV. There is 1317 room-temperature electromagnets in SPS, including 744 dipoles for bending. SPS could be turned to $p\overline{p}$ (proton-antiproton) collider. This setting won a Nobel price in 1983 for the discovery of W and Z particles. So far SPS provide beams for the LHC (Large Hadron Collider), the NA61/SHINE and NA62 experiments, the COMPASS and AWAKE experiment. NA61/SHINE experiment studies the hadron production properties using proton or pion beam in collisions with many different types of fixed targets. NA62 studies how to charged kaons (produced by proton beam from SPS fired into block of beryllium) decays into a charged pion and a neutrino-antineutrino pair. The COMPASS uses beam of muons to explore hadrons are created from quarks and gluons. AWAKE experiment investigates the accelerating of charged particles by plasma wakefields [8]. It uses proton beams from SPS and injects them into a plasma to gain strong wakefields. A second beam is then accelerated by the wakefields, up to several GeV energy. The transition between hadrons and so-called quark-gluon plasma is studied in SHINE experiment. The CLOUD experiment uses special cloud chamber that can make a temperature and conditions the same as in the atmosphere. It looks for a possible link between cosmic rays and cloud formation. CAST experiment is equipped with a telescope to search for theoretical particles called axions. The telescope is built of the LHC dipole magnet acting as a viewing tube. All of the accelerators, decelerators and particle detectors are located in Geneva region except AMS (Alpha Magnetic Spectrometer). AMS is situated on ISS (International Space Station) and measures antimatter in cosmic rays.

1.2 LHC

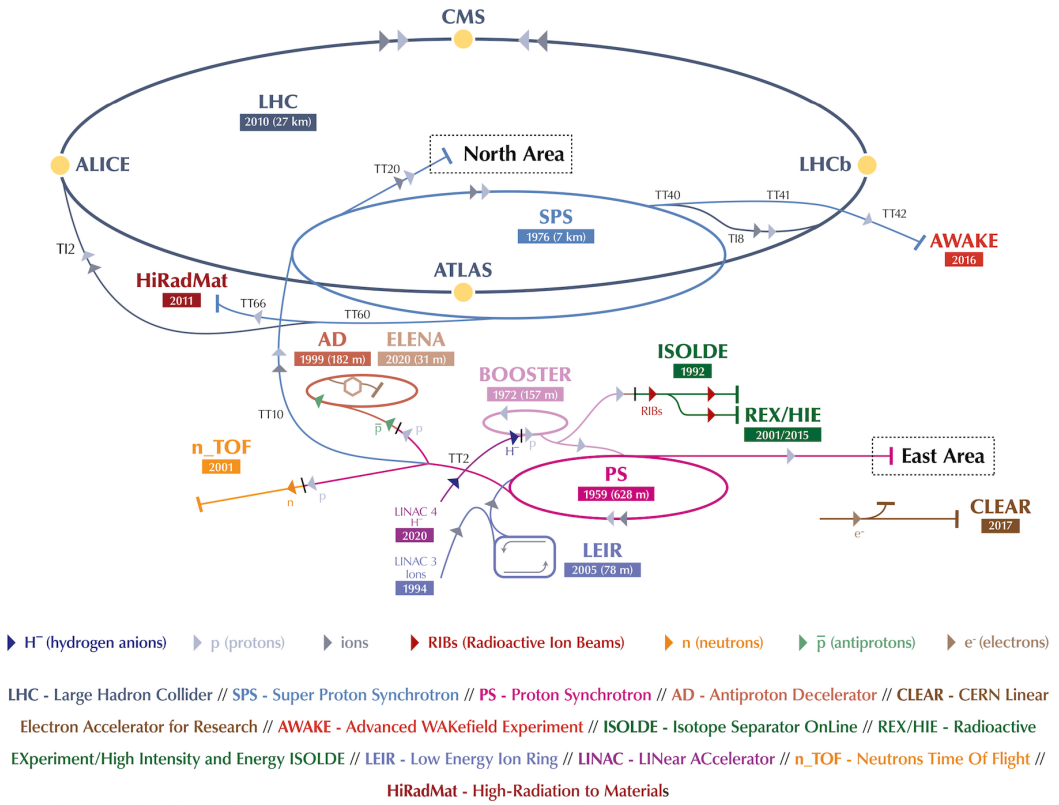

Figure 1.2: CERN accelerator cascade [9].

It has been the world's biggest and most powerful particle accelerator for more than ten years now. It collided two bunches for the first time on September 10, 2008. CERN's accelerator cascade was described in previous section and it could be seen on Fig. 1.2. This thesis will focus on the LHC as a pp collider and do not mind other possibilities (such as proton-ion or ion-ion collider) [10]. Protons from SPS are injected into the LHC, where they gain energy of 6.5 TeV (travel about 3.1 m/s slower then light in vacuum, $\gamma \approx 6937$). The LHC got its name Large because tunnel (formerly used to house LEP collider) is 26.7 km long, at a depth ranging from 50−175 m, hadron because it is suitable to accelerate hadrons and world collider meant that bunches of particles orbit in closed loop while RF system and magnetic field to have to be synchronized to match particle revolution frequency f_{rev}. Protons travel in LHC beampipe in both clockwise and counterclockwise direction. They collide in almost head-on collision on 4 spots of LHC ring called IPs (Interaction Points) where four main experiments are based. This non-zero angle is called crossing angle Θ_C. When the LHC is in full operation, it is filled with more than $2,800$ bunches (with approximately 10^{11} protons in one bunch). They travel in beampipe at discrete intervals of 25 ns, so the bunch collision rate is $f = 40$ MHz (40 million bunch crossing per second at each IP).

The power of the LHC is quantified by physical quantity called instantaneous luminosity that is giving the number of the particles produced with cross-section σ per unit time interval $dN/dt = \sigma\mathcal{L}$. It is defined as

$$\mathcal{L} = f_{rev}\frac{N^2 n_b \gamma}{4\pi\epsilon_n\beta^*}R, \tag{1.1}$$

where N is the number of protons in one bunch (it is assumed that both the colliding bunches have same population of protons), n_b is number of bunches in one beam, γ is gamma factor of proton, geometrical emittance ϵ is proportional to area in momentum-position phase-space and it is constant on whole path around the LHC except when it is accelerated. Normalised emittance ϵ_N is then defined to be preserved with acceleration. The β gives information about machine optics near IP, mainly about quadrupole magnet configuration defined as $\beta = \pi\sigma^2/\epsilon$, where σ is cross-sectional size of bunch. Sometimes it is also referred as the distance from the focus point that the beam width is twice as wide as the focus point. Value of β in IP is usually denoted as β^*. Luminosity geometrical reducing factor gives information about the impact of beam-beam effects, is $R = (1 + \sigma_z\theta_c/\sigma_T)^{-1/2}$, where σ_T, σ_z is the transverse and longitudinal beam sizes respectively. When the power of the accelerator is viewed in a longer time period, the integrated luminostity L_{int} is introduced as the time integral of $\mathcal{L}$. When the machine is working it draws around 200 MW of electrical power. In order to accelerate the bunches of protons a longitudinal electric field is used. Oscillating voltage is applied, so that the particle is only affected by an accelerating voltage at the gap and the voltage then cancels out as the particle goes around the rest of the ring. Magnets are the key components when a new collider is build. From the assumption of equivalence of magnetic and centripetal force one can get a relation $|\vec{p}| = qR|\vec{B}|$ between momentum $\vec{p}$, charge q, radius R and magnetic field $\vec{B}$. This equation says that if one wants to increase the momentum of colliding particle one has to make a bigger collider (in means of a bigger R) or magnets need to be able to deliver stronger magnetic field. Focusing and bending could be done using electric or magnetic force. In accelerators it is usually the magnetic one. One introduces Lorentz force as $F_L = q(\vec{E} + \vec{v} \times \vec{B})$, where $\vec{v}$ is velocity and $\vec{E}$ is electric field acting on the particle. For particles traveling nearly by light speed $|\vec{v}| \approx c$ is magnetic field much more effective. Benefits also come from the fact that magnetic force exerted on particle is always perpendicular to its velocity. All magnets are cooled down by super-fluid helium to temperature 1.8 K to become superconducting [11]. If material is cooled down to temperature close to absolute zero it is in superconducting state, where resistance falls to zero, a current can circulate inside the material without any dissipation of energy. The magnet is wound of a superconductive cables with strands made of niobium-titanium filaments surrounded by cooper matrix [12]. Magnets could be classified according to the number of poles they contain. If they have two poles then they are called dipole magnets, quadrupoles has four poles obviously. Quadrupole magnet focuses a beam of relativistic particles in the same way as lenses behave on light. The beam size is squeezed in one transverzal coordinate and at the same time it becomes wider in second one. Because of this in the LHC system of such magnets is used.

There is 1232 dipole magnets that keep protons on right circular path and 392 quadrupole magnets focusing the beam. There are also higher order magnets used in the LHC such as sextupoles, which correct jobs after quadrupoles or octupoles and or so on. Protons are charged particles, so they repulse each other. Because of this fact one has to focus them and keep transverse beam size as small as possible (to increase the $\mathcal{L}$). Quadrupole and higher order magnets do the job for us. Quadrupoles act on beam of charged particles in the very same way as lens acts on beam of light [13]. It focuses the beam in one direction and spreads it in the other one. That is the reason, why two quadrupoles are coupled in the row, where the second one is 90° rotated around the axis of beampipe. Because of the enormous number of protons in each bunch, the energy is slightly different for each proton so they are following slightly different paths. The sextupole and higher order magnets are able to focus the particles according to their energy.

HL-LHC

The LHC is has been constantly upgraded since 2010, when it started to collect data. At that time was the centre-of-mass energy $\sqrt{s}$ was equal to 7 TeV. Then it was increased to $\sqrt{s} = 8$ TeV in 2012. This period is called Run 1. After every three or four years of operation, the LHC is turned off for few years, officially it is denoted as LS (Long Shutdown). The accelerator and experiments that operate on it need this time to upgrade experimental equipment down in the tunnel. Specifically the LS1 (20122015) took the place after Run 1. During this shutdown, an energy was successfully increased to $\sqrt{s} = 13$ TeV. Run 2 corresponds to years between $2015 - 2018$, which were crucial for operation of the LHC. In the first half of the Run, the nominal (designed) instantaneous luminosity of 1.0×10^{34} cm^{-2}s^{-1} was achieved. Even after EYETS (Extended Year-End Technical Stop, scheduled after first two years of each run) the designed luminosity was increased two times. The experiments operating on the LHC are also upgraded and their status together in Run 1, Run 2 and Run 3 is called Phase 1. Currently the LHC is in LS2. On October 2021 the Run 3 should start and following $LS3$ is time dedicated to upgrade detectors to Phase 2 towards the HL-LHC [14]. As the name hints HL-LHC should deliver up to ten times more collision than the LHC was designed for. It will allow to probe the Standard Model with even greater precision and will extend the sensitivity to possible anomalies in the Standard Model [15]. For this purpose new quadruple magnets with strength of 12 T have to be placed on both sides of each IP.

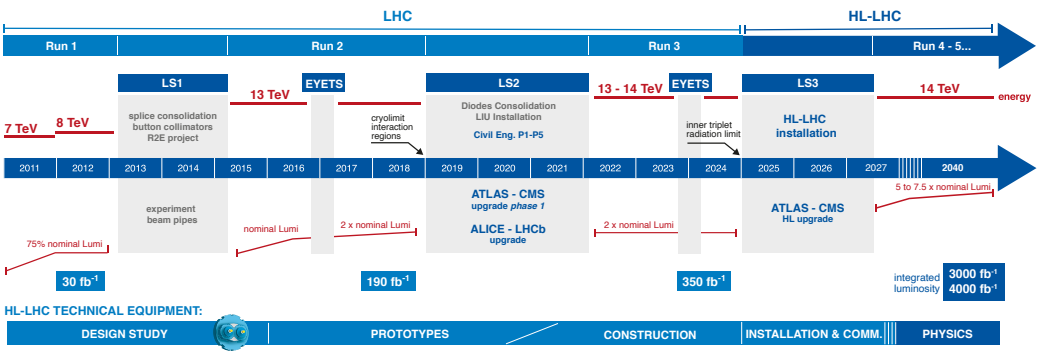

Figure 1.3: LHC/ HL-LHC Plan (last update January 2021) [16]

1.3 CMS

There are four major experiments operating at the LHC. The ALICE (A Large Ion Collider Experiment) focuses on the interactions of heavy ions. The goal of this project is to explore the physics of the strong interaction and the new phase of matter, the quark-gluon plasma. The LHC-b (Large Hadron Collider beauty experiment) studies CP violation in the decays of hadrons containing heavy quarks. The ATLAS (A Toroidal LHC ApparatuS) and the CMS (Compact Muon Solenoid) are called the "general-purpose detectors". Their main mission was to find a Higgs boson (it was successfully achieved in 2012 [17] [18]) and there are some universal aims such as to explore the physics on TeV scale, to search for undiscovered particles or extra dimensions of the space. The main difference between the CMS and the ATLAS is the arrangement of magnet used for bending of the created charged particles. ATLAS uses toroidal magnet while the CMS is equipped with a solenoid. Other big difference is the electromagnetic calorimeter. While the ATLAS is equipped with the sampling calorimeter (lead and stainless steel are absorbing materials and liquid argon is the active material), while electromagnetic calorimeter on the CMS in made of homogeneous crystal. Because this thesis deals with CMS experiment, it will be described closer in the following chapter.

The CMS is a cylinder-shaped detector 21 metres long, 15 metres wide and 15 metres high (see Fig. 1.5). It is placed 100 m below the ground near small french town Cessy. Despite word compact in its name, weight is over 14 kt (the CMS is twice smaller but twice heavier then ATLAS detector). It consists of many layers of the forward-backward symmetric sub-detectors. Right-handed coordinate system is used. The z axis is parallel to beam line, $x - y$ plane is perpendicular in the way that x points in to center of the LHC (see Fig. 1.4).

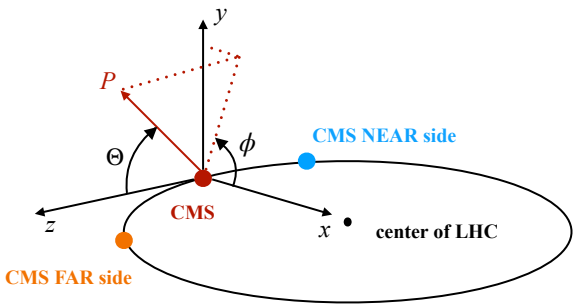

Figure 1.4: CMS coordinate system.

To easily describe each detector position or track position of the particle traveling though the detector, it is conventional to introduce following variables. The polar angle measured form the positive beam axis is denoted as Θ and azimuth angle measured from the positive x-axis in the xy plane is indicated with ϕ. Then pseudorapidity η is defined as

$$\eta = -\ln\tan\frac{\Theta}{2} = \frac{1}{2}\ln\frac{1+\cos\Theta}{1-\cos\Theta}, \quad y = \frac{1}{2}\ln\frac{E+p_z}{E-p_z} = \frac{1}{2}\ln\frac{1+\beta\cos\Theta}{1-\beta\cos\Theta}, \tag{1.2}$$

when the velocity of particle is relativistic, one benefits from defining the rapidity y. They become asymptotically equivalent as $\beta = |\vec{v}|/c \to 1$.

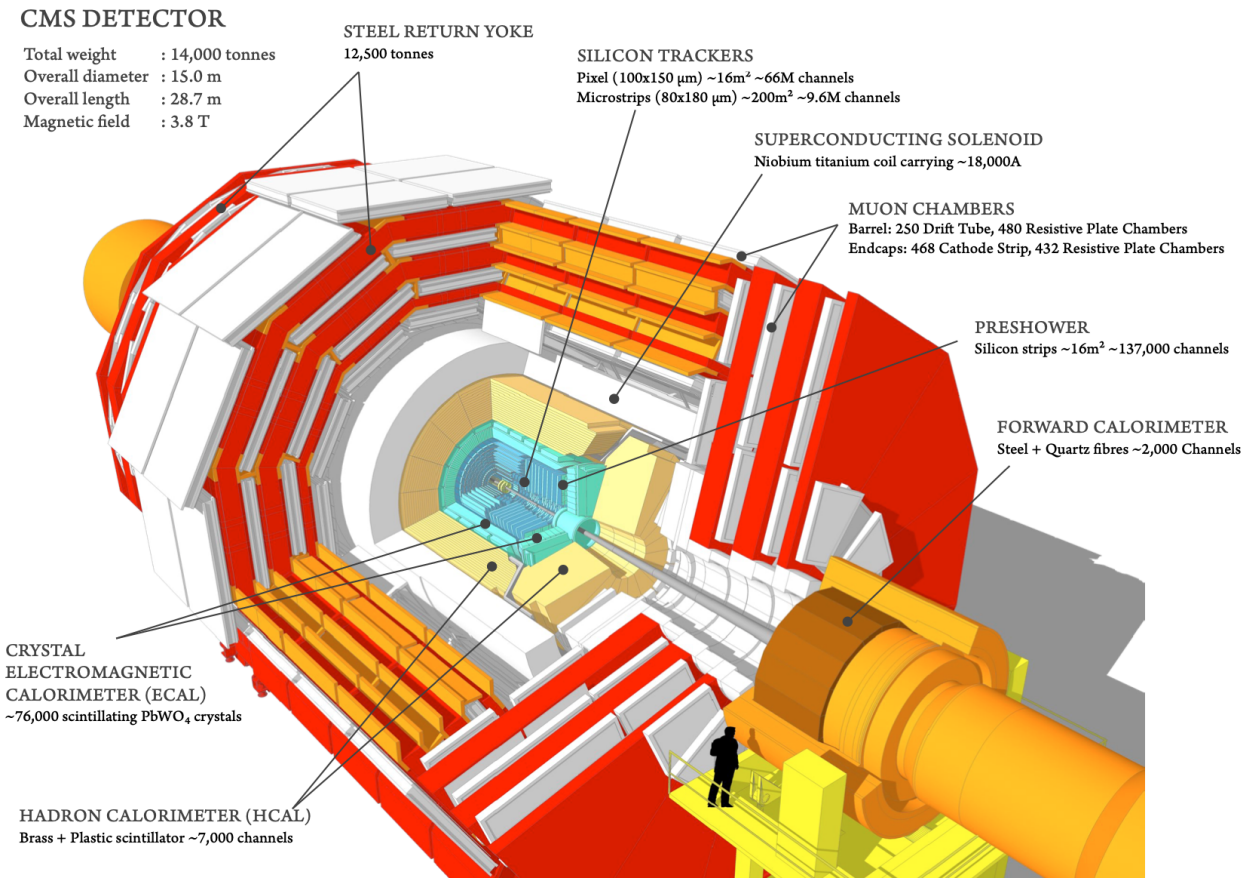

Figure 1.5: Visualization of the CMS detector [19].

The inner tracker

Closest component to the IP is CMS inner tracker measuring 5.8 m with a 2.5 m radius over a pseudorapidity range of $|\eta| < 2.5$ m [20]. It consist of two parts: Pixel detector and Silicon strip detector, being both semiconductor detectors. When charged particle transverses sensor sensitive volume, electron-hole pairs are created along its path. Signal from the electrons is amplified and transmitted to back-end electronics to further signal processing. Pixel detector is used to obtain a position of the vertices, and of a silicon strip tracker, which allows for the measurement of the momentum of charged particles due to the bending of their tracks in the homogeneous magnetic field. Pixel detector is equipped by the silicon sensors with a size of 100×150 /mum^2 in the barrel region, arranged in 53 cm long layers, with the space resolution of just 10 μm in $r - \phi$ plane and 15 μm along z. Second part of pixel detector are end-cap disks having space resolution of just 15 μm in $r - \phi$ plane and 20 μm along z. The silicon strip tracker is the outermost part of the inner tracker, equipped with ten layers of a microstrips, while every end-cap region ($1.5 < |\eta| < 2.5$) has three inner mini-disks and nine outer disks. The detector is sectioned into four parts: the TIB (Tracker Inner Barrel), the TEC (Tracker End-Caps), the TOB (Tracker Outer Barrel) and the TID (Tracker Inner Disks). Four innermost layers are part of the TIB, covering $|r| < 55$ cm and $|z| < 65$ cm [21]. Pixels there are parallel to the beam pipe and their resolution is $13 - 38$ μm in $r - \phi$ plane. Outermost part of barrel is called TOB, consisting of last six layers in $|r| > 55$ cm and $65 < |z| < 110$ cm.

Sensors there are slightly bigger compared to ones in TIB, but high resolution $18 - 47$ μm in $r - \phi$ persist. Rest of inner tracker sensors are placed on disks by side of the barrel. TID contains first three disks in $20 < |r| < 50$ cm and $65 < |z| < 120$ cm. It provides measurement of the ϕ coordinate, with precision ranging from $15 - 50$ μm when radius is low respectively high. Last part of the inner tracker is TEC covering the region $120 < |z| < 282$ cm, divided to seven rings per each side. Resolution there is comparable with TID. When a tracker is build, one has to mind that whole mechanical structure has to be as light as possible to do not disturb created particles on their path. Also it is very important to get rid of materials that could easily activated.

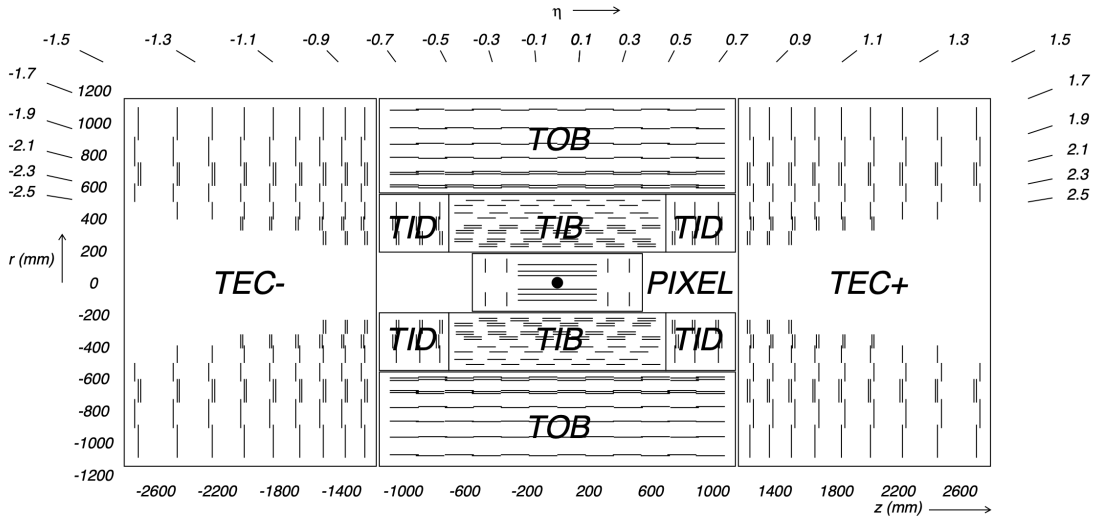

Figure 1.6: Scheme of CMS inner tracker [22].

Calorimetery

A calorimeter is a device that absorb energy of the particle transversing it and in return it provides the information about energy or particle type. Interesting property of calorimeter is the uncertainty of energy resolution decreases as energy of particle increases. As particle going through matter it looses energy due to showering effect (it will be closely described in next chapter). There are two types of the particle showers. Electromagnetic one is measured by the electromagnetic calorimeter and hadronic by the hadronic one. Also there are two types of calorimeters. In the homogeneous calorimeter is the entire volume sensitive, so the signal is generated in one type of the material. In the sampling calorimeter material that produces the particle shower (active detector layers) is different from the material that measures the deposited energy (pasive absorber). Calorimeters are capable to detect charged particles but also neutral ones. They can also provide information about particles barely interacting with the matter in terms of the so-called missing energy.

The electromagnetic calorimeter

The CMS ECAL (Electromagnetic CALorimeter) is homogenous lead tungstate ($PbWO_4$) crystal calorimeter. This technology was motivated by the need for the ECAL to be sufficiently compact to fit inside the inner tracker and solenoid magnet (described in next subsection). Even through tungstate is very heavy element, a touch of oxygen in its crystalline form makes it highly transparent which is necessary condition for being good scintillating material. These high-density crystals produce light in the fast, short, well-defined photon bursts in proportion to the particle's energy. APD (Avalanche photodiode) is silicon photodetector glued onto the back of each crystal to detect the scintillation light and convert it to an electrical signal [23]. A strong electric field is applied to the each APD, so when a photon strikes a electron out of the silicon and ionizes atom, the electron is accelerated within the electric field and further ionizes other silicon atoms, creating an electron avalanche. To describe any electromagnetic shower it is useful to introduce the radiation length X_0 as average distance that particle needs to lose $1/e(\approx 37\%)$ of its energy by the radiation. The ECAL can be characterised by the Molière radius R_M, a characteristic constant of the material giving average lateral deflection of incident high energy electron or photon after traversing one radiation length. Molière radius could be approximated as $R_M = 0.0265(Z + 1.2)X_0$, where Z is proton number of material, where the shower takes place. Crystals of tungsten has $X_0 = 0.89$ cm and $R_M = 2.2$ cm. Cryslats are unique because of their short scintillation delay time, with 80% of the scintillated light being emitted within one bunch crossing. ECAL consist of the two regions. In the barrel region there is 62200 crystals with cross section 22×22 mm^2 and length 230 mm (25.8 X_0) [24]. The end-cap region consist of 7324 crystals with cross-section 28.6×28.6 mm^2 and length 220 mm (24.7 X_0). End-cap crystals have slightly different photo-detectors, namely VPT (Vacuum PhotoTriode). Because of stronger radiation field in end-cap region they have to be more radiation tolerant. The ECAL covers pseudorapidity range of $1.479 < |\eta| < 3.0$.

The hadronic calorimeter

Whereas the ECAL measures the energy of electromagnetic particles (mainly photons and electrons), the HCAL (Hadronic CALorimeter) measures the energy of hadrons, as the name hints. Hadronic shower is created in different way then electromagnetic one. Particles carrying color charge (quarks and gluons) cannot exist in free form, because the QCD confinement allows only a colorless states. Therefore, only a narrow cone of hadrons and other particles produced by the hadronization of a quark or gluon, called jet, can be seen in the hadronic calorimeter. Hadronic shower also consist of particles with decay channels to leptons, which can create the EM shower. The HCAL is sampling calorimeter having brass as absorber material and the tiles of plastic scintillators as active material. When primary particle hits absorber material, secondary particles are produced and those again interact with absorber and more particles are produced. Energy of all created particles is then summed up using scintilator tiles in the active area. Charged particles passing through the scintillator tiles excites surrounding atoms and in response emit a blue-violet light. Each tile have the wavelength-shifting optical fiber, which absorbs the scintillation light and shifts its wavelength into green region of the visible spectrum [25]. Green light is then transmitted through clear optical cables to the readout boxes which are strategically situated at different points within calorimeter. HCAL consist of four

distinct subsystems: the HB (Hadron Barrel), the HE (Hadron End-cap), the HO (Hadron Outer) and finally the HF (Hadron Forward) calorimeters. The HB and the HE are inside cryostat of the solenoid magnet. The HF is placed at 11.5 m from the IP and it is made of out steel absorbers and the quartz fibers as active material, that causes the production of the Cherenkov radiation when particles pass through the fibers. Such a design is essential to improve the detection of the forward jets and of the particles scattered in the very forward region. The HB covers the rapidity range $|\eta| < 1.4$, with the HE providing coverage over the range $1.3 < |\eta| < 3.0$. Both HB and HE are segmented in $\eta - \phi$ by 0.087×0.087 for $|\eta| < 1.6$ and up to 0.17×0.17 for $|\eta| >= 1.6$ [26]. The HF extends coverage up to $\eta < 5.2$ region.

Solenoid magnet

The solenoid magnet (see Fig. 1.7) gives the CMS its last name. It generates 4T magnetic field parallel to the beam line. This enormous magnetic field is created by current nearly 20 kA and its operating temperature is 4.6 K [27]. Magnetic field must be confined to the volume of the detector by the steel yoke. The solenoid has diameter 6 m and it is 13 meters long and weights more than 10 kt (the biggest solenoid ever build). It is capable to store around 2.5 GJ of energy. Desired magnetic field is used for bending of charged particles. Charged particle's path curvature gives a information about sign of charge and momentum of the particle. As particle momentum raises, radius of particle track grows as well. Tracks are reconstructed by the hits in the inner pixel detector placed inside the magnet volume.

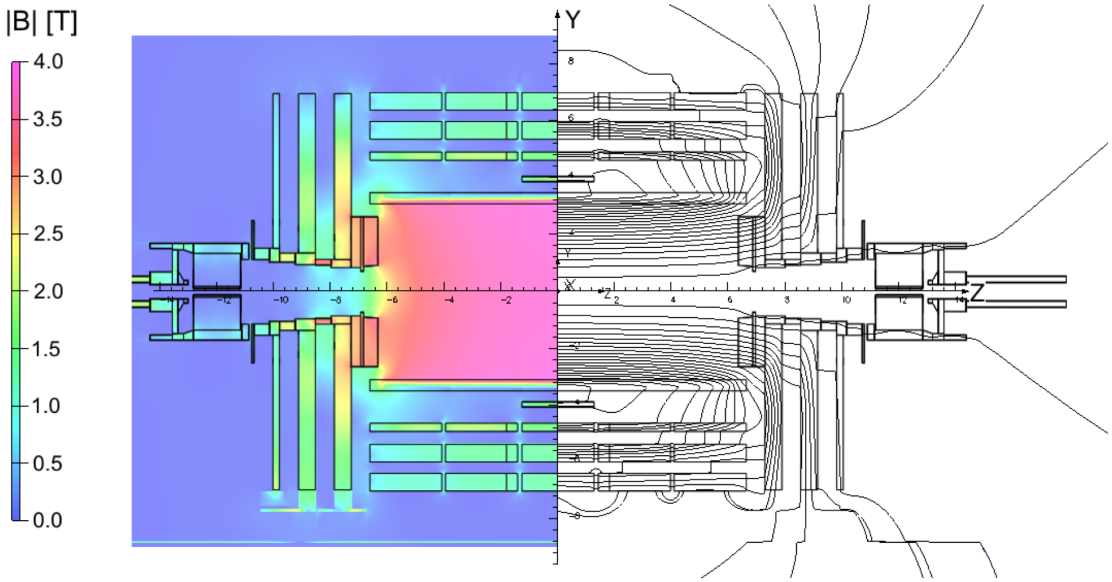

Figure 1.7: Simulation of magnetic field in CMS solenoid magnet [28].

The muon detector

As abreviation for CMS suggests, measuring muons is main task of this detectors (the Higgs boson's clearest decay channel called golden decay is its decay to 4 leptons, mainly to muons). Muons are probably the hardest charged particle to detect, since they can penetrate several metres of iron without a single interacting. Because of this fact are muon detectors placed further away form the IP, then other detectors. Muon stations sit outside the magnet coil and are interleaved with the iron return yoke plates. To determinate muon momentum one has to know radius of its path in the magnetic field. Muon chambers also provide fast triggering information and hence decrease amount of stored data. In total there are 1400 muon stations of four different types: DTs (Drift Tubes), CSCs (Cathode Strip Chambers), RPCs (Resistive Plate Chambers) and GEMs (Gas Electron Multipliers) [29]. The term station refers to an assembly of chambers around a fixed radius (in the barrel) or z-axis coordinate (in the end-cap) view of chambers deployment is in Fig. 1.8. Barrel consist of four stations labelled MB1-MB4 (Muon Barrel 1 and so on) and another four stations ME1-ME4 in end-cap region. In barrel region (DTs and RPCs occurs there) are stations segmented into five wheels[30]. W0 (Wheel 0) is centered in $z = 0$ and wheels W+1 and W+2 (W-1 and W-2) in the $+z$ (-z) direction. Similarly in the r direction in the end-caps, there are rings of RPC and CSC labeled ME1/n-ME4/n, where integer n increases (up to three) with the radial distance from the beam line. At $|\eta| < 1.2$, the muon system is then still inside a return magnetic field of 2 T, oriented backwards with respect to the inner field.

Drift tubes

DTs are responsible for finding precise muon track position in barrel part of the detector. They are ionizing detectors consisting of tubes with diameter of 4 cm, filled with gas. When charged particle passes through gas volume, it ionize the gas atoms. Electrons have bigger mobility then positively charged ions, so they are used for generating the signal, electrons follow the electric field, which guide them to positively-charged wire. System of such detectors is able to deliver two coordinates of the muon's track position. By registering where along the wire electrons hit it, together with information about the particle original distance away from the wire, 2D information about track could be inferred. Each chamber has size of 2.5×2 m^2 and have 12 layers of aluminium arranged in the three groups of four. One layer hosts 60 tubes. The DT chambers are installed on the five wheels YB2, YB-1, YB0, YB+1 and YB+2. Each wheel is further divided into 12 sectors, where each one covers approximately 30° around the interaction point.

Cathode Strip Chambers

The CSCs are placed on eight end-cap disks in total of 450 chambers. Magnetic field there is not confined by iron yoke and hence is rather problematic. CSCs are build up of the positively-charged anode wires crossed with the negatively-charged cooper strip surrounded by the gas volume. Tubes are filled with 50% Ar, 40% CO_2, and 10% CF_4. Wires are closely spaced to increase precision of the particle track. The charged particle going through it ionize gas atoms and produced electrons travels to anode creating avalanche of electrons. Conversely positive ions are pulled to cathode plates, giving second coordinate of particle track, because plates are perpendicular

to the wire direction. The wires are supplied with the high voltage and are read out in the groups, its width varies between different chambers from 1.5 cm to 5 cm. There are six layers in the each CSC module. It is very fast detector, this ability is used for triggering.

Resistive Plate Chambers

RPCs have two parallel plates, a anode and a cathode, both made of a very high resistivity plastic material and are separated by a gas. Gas is freon based gas mixture, which contains $C_2H_2F_4$ and SF_6 (both greenhouse gases) [31]. Charged particle going through gas knocks out one of its electrons. This electron causes the avalanche, electric signal is then read out by the external metallic strips after a small but precise time delay. Particle momentum is obtained from the pattern of hit strips enormously fast, so the information from detector is also used for triggering purposes. The time resolution is close to one nanosecond. The barrel region contains 480 chambers, which vary in size and are located in the range of $|\eta| < 0.8$ and $|z| < 7$ m.

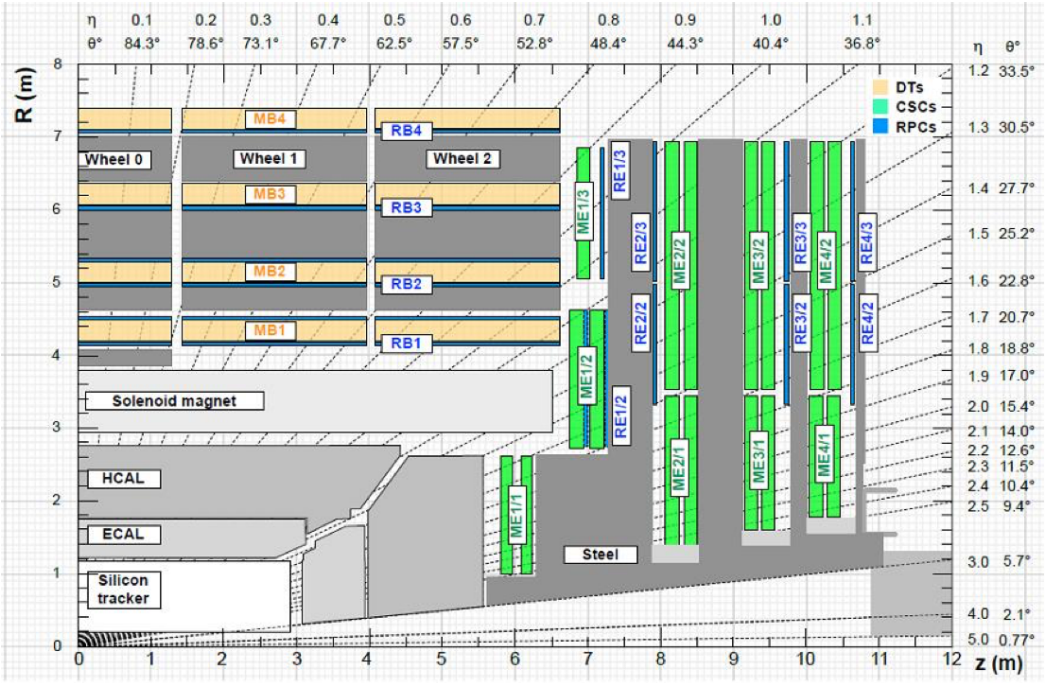

Figure 1.8: Layout of one quadrant of the CMS muon detectors [32].

Gas Electron multipliers

This type of detector is part of the CMS since 2019. It is arranged in end-caps, so it has to withstand enormous radiation doses. It is made out of three layers, each one is 50 μm thick copper-cladded polyimide foil [33]. Foil is embedded in the gas, mixture of the Ar and CO_2. Plates has cross-sectional area of almost 2 m^2. GEM detector creates the large electric field in small holes in a thin plates and the avalanche occurs inside small holes. The resulting electrons are ejected from the sheet, and a separate system must be used to collect the electrons and guide them towards the readout. The GEM chambers allow a better muon track identification and also wider coverage in the very forward region.

Trigger system

When the CMS is performing at its peak, bunches of protons collide 40 million times per second so in each IP, so interaction rate is 40 MHz. It is impossible to store data from all of the collisions (tens of terabytes per second only at the CMS) and even if one can, most of events are not physically interesting. Trigger system has a goal to decide which information should be kept for later offline analysis or lost forever. There are 2 stages of such a system in the CMS. L1 (Level 1) is hardware based and fully automatic trigger system, that quickly looks for signs of interesting physics. L1 decides 3.8 μ after collision, if event was interesting or not by presence of energy deposits in CMS subdetectors [34]. There are two parallel processes taking place in L1 trigger: the Muon Trigger and the Calorimeter Trigger. The muon trigger uses information from DTs, CSCs and RPCs and the calorimeter triggger processes data from ECAL and HCAL (including HF). The L1 trigger system restricts the output rate to 100 kHz. The second level of the CMS trigger system is the HLT (High-Level Trigger), implemented in software, selecting an average rate of 400 Hz for event storage [35].

CMS forward components

All previously mentioned detectors are part of central detector. There are other components in the CMS cavern relevant for this work. These are shield around the HF, the CASTOR calorimeter, the TAS collimator, rotating shield behind it and block house surrounding the end of the Q1 quadrupole follows. They are made out of perspective shielding materials such as steel, concrete or borated polyethylene. The forward shielding of the CMS consist of shielding elements along the beam line between the endcap and the end of the cavern. TAS collimator protects the first quadrupole magnet from unwanted particles coming from IP. The TAS gives the biggest contribution to background radiation in from all CMS components. The collimator sits inside the rotating shield (RS). The RS is made in the way that it can be opened to allow the movement and access to other CMS components and detectors in the shutdown period. Inside RS and after the HF is the CASTOR calorimeter, which is situated to intercept very forward directed particles.

1.4 BRIL

The BRIL (Beam Radiation, Instrumentation, and Luminosity) project is key part of the CMS experiment taking care of radiation simulation, luminosity measurements and radiation background measurement and detection. The duty of the BRIL is to monitor beam conditions, whenever it is present in the LHC. Towards the HL-LHC, BRIL is responsible for: passive and online monitoring of radiation fields in CMS cavern, ensures protection of detector sensitive parts, measures online bunch-by-bunch luminosity in the CMS, investigates time between two bunches and keeps an eye on the accelerator performance or provides signals for the L1 trigger for each beam for the CMS global trigger.

RadSim Group

At CMS the dominant source of radiation background in standard operation is generated by proton-proton collision. When two bunches collide, many new particles are produced, usually with enough energy to further produce new particles in the collisions with material in the experimental cavern. When a charged particle follows curved path it loses its energy by radiation. Particles in the LHC follow nearly circle path and radiation they produce is called synchrotron radiation. There is very strong vacuum inside the beampipe 10^{-7} Pa, despite this there are some redundant molecules of air. When a highly relativistic beam of protons hits the molecule, a shower of secondary particles is observed. Experimental cavern is because above mentioned fact inhabitable for living organism, not only when the beam is present in the LHC but also many days after it is off, due to activation of the material. Showering particles can be produced in interactions of beam with LHC components such as collimators or beam monitors [36].

The RadSim (Radiation Simulation) group is part of the BRIL responsible for maintaining and improving the radiation simulation infrastructure, which is used by the CMS projects to estimate the radiation fields in the CMS experimental cavern and inside detector sensitive elements. The RadSim group also provides so-called benchmark studies. This means verifying simulated radiation properties against measured data and explaining a possible differences between those. For radiation monitoring BRIL uses detectors described in Chapter 3.

The RadSim group also cooperates with HSE/RP (The Occupational Health Safety and Environmental Protection / Radiation Protection) group for simulations related to activation of material and possible dose to personnel. Safety to personnel has to be ensured so when new accelerator is build, the group advises how to minimize radiological hazard [37]. Extensive studies are performed to design shielding of radiation from equipment in cavern. Precise estimation of radiation field in cavern relies on operating radiation monitors.

Chapter 2

Passage of radiation through matter

When particle goes through matter it may be deflected from original direction, its energy may be transferred to a production of new particles or it can harm material structure. Example of such an interaction is elastic scattering from nuclei or inelastic collisions with electron shell of material. When dealing with the particle interactions it is convenient to sort particles if they have charge or not and according to their rest mass. This section will describe interactions of light charged particles such as electrons, heavy charged particles as muons, charged mesons, protons and their antiparticles. Particle without charge include, for example a photon or a neutral hadron. Collisions might be soft (with small energy transferred) resulting in excitation or harder enough to ionize atom. Number of inelastic interactions is large at macroscopic scale and the fluctuations in the total energy loss are small so it is absolutely relevant to work with average energy loss per unit path length $\left\langle \frac{dE}{dx} \right\rangle$ also called stopping power [38].

Heavy charged particles

The formula for energy loses of heavy charged particle was first derived by M. Born, later on a quantum-mechanical calculation was done mainly by H. Bethe and F. Bloch. Born's equation is a function of an impact parameter, while Bethe-Bloch formula is characterized by momentum transferred. This plays a crucial role because impact parameter is not a measurable quantity, while momentum transferred is. The mean rate of energy loss by relativistic heavy charged particles is

$$-\left\langle \frac{dE}{dx} \right\rangle = Kz^2 \frac{Z}{A} \frac{1}{\beta^2} \left[\frac{1}{2} \ln \frac{2m_e c^2 \beta^2 \gamma^2 T_{\max}}{I^2} - \beta^2 - \delta - 2\frac{C}{Z} \right], \tag{2.1}$$

where constant K has value of 0.1535 MeV cm^2 s^{-1}, z is charge of incident particle in units of elementary charge e. Z (A) is proton (nucleon) number of material, β is velocity of incident particle as a fraction of speed of light in vacuum and $\gamma = (1-\beta^2)^{-1/2}$. When this equation is derived, integral over possible energy transferred to atomic electrons is performed, T_{max} is a cut-off parameter giving maximum energy per one collision. Mass of electron m_e is and I stands for excitation potential. The quantities δ and C are corrections important at high and low energies respectively.

Formula is valid with an accuracy of few percents for intermediate-Z materials in region between $0.1 < \beta\gamma < 1000$. The Bethe-Bloch formula only deals with particle interactions with matter and hence radiation looses are not taken into account. When projectile velocity is small and hence comparable to speed of atomic electrons or very big and radiation effects begin to be important the formula is no longer applicable. At non-relavistic energies Bethe-Bloch formula is dominated by $1/\beta^2$ until $\beta \approx 0.96$ (or $\beta\gamma = 3.43$). At this point the function has local minimum. Particles with corresponding energy are called the MIP (Minimum Ionizing Particle). When energy of particle is further increased its energy loss grows logarithmicaly. When material consists of various elements, a good approximation is to average over all elements in the compound weighted by the fraction of electrons belonging to each element. As an example, the stopping power of positively charged muon in copper could be seen in Fig. 2.1.

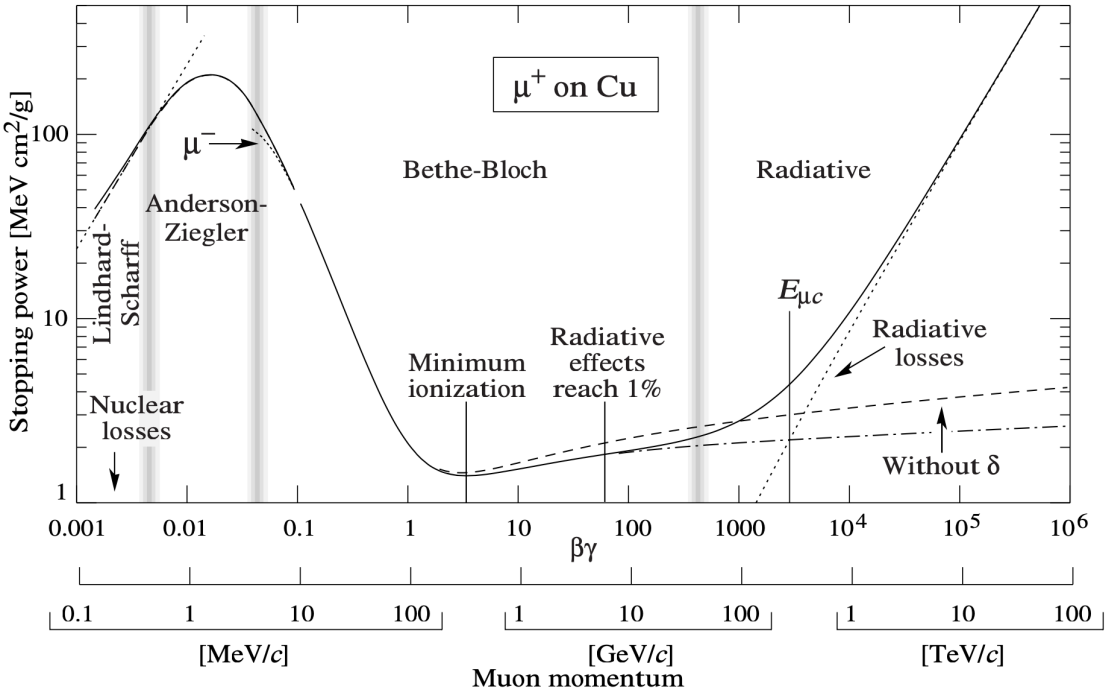

Figure 2.1: Stopping power for μ^+ in Cu as a function of muon momentum. Minimum is in $\beta\gamma \approx 3$ [39].

Both heavy and light charged particles can also lose energy if they cross boundary of two materials with different indices of refraction n. This index is defined as a speed of light in a vacuum divided by speed of light in given material. Transition radiation is produced by particle on boundary of two materials with different n. Cherenkov radiation is effect occurring when charged particle transfers through a material faster then light. The shock-wave induced by Cherenkov effect is emitted in a cone, with angle $\cos(\Theta_C) = 1/n\beta$.

Electrons and positrons

Electrons (or positrons) with energy less than few MeVs lose most of their energy by ionizing of material. They also undergo elastic collisions such as electron-electron scattering or elastic interaction of electron and positron (also known as Bhabha scattering). Because of small electron mass, radiation effect also comes into play. They lose energy, because whenever charged particle is disturbed on its straight line path, for example by an electrical attraction of a nucleus, it emits photons inversely proportional to square root of particle mass (i.e. it is more relevant for light particles). The total energy loss of electrons and positrons is therefore sum of energy deposits by collisions with material and radiation losses. The radiation (also called bremsstrahlung) depends on a strength of an electric field felt by electrons. For each material E_C is energy of electrons, which feel the same stopping power by collisions and radiation.

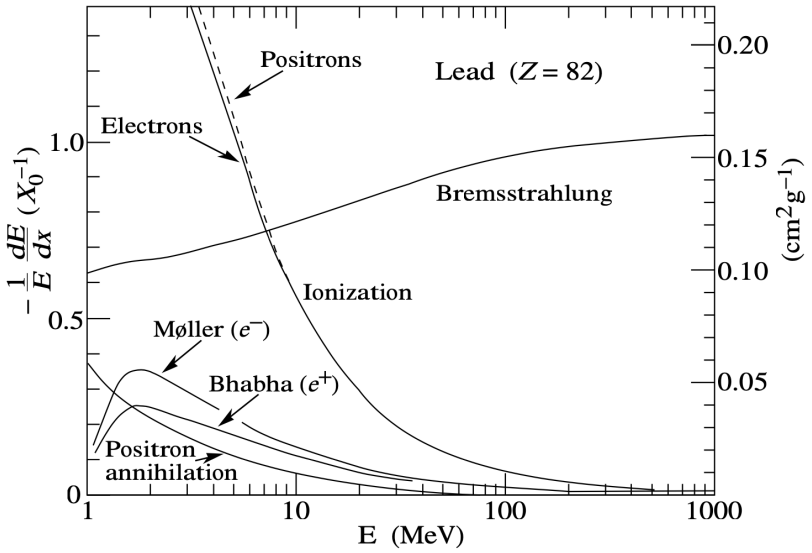

Figure 2.2: Fractional energy loss per radiation length in lead as a function of electron or positron energy [40].

Photons

Photon induced interactions in matter are different from processes induced by charged particles. Particles of light are massless and they do not carry electric charge, so occurrence of many inelastic collisions with electron shell of material is not observed for them. A type of photon interaction is highly dependent on its energy E_γ. Historically the first photon interaction ever explained is a photoelectric effect, showing particle properties of light. Analogously to elastic collisions of massive particles, photons participate in Compton, Thomson and Rayleigh scattering. When external field is present to carry out part of momentum and photons have enough energy, electron-positron could be created from the photon. External field is electric field of nucleus or atomic electrons. Photons also have small but non zero probability to be absorbed by nucleus and neutron can be released. This process is known as nuclear dissociation reaction.

When burst of photons traverse through a layer of material, there is no degradation of energy but intensity is decreased. It is guided by differential equation $dI = \mu I dx$, where I is intensity of the photon beam and μdx is probability that photon interact within depth x. Coefficient μ is called photon attenuation coefficient. Number of photons going through matter decrease exponentially $I = I_0 \exp(-\mu x)$. Total photon-lead cross section in lead is in Fig. 2.3.

Photoelectric effect

This effect was described by A. Einstein and is so fundamental, that he received Nobel prize for explaining it. The photoelectric effect takes place, when atomic shell electron is kicked out of electron shell by incident photon. Energy of electron leaving the atom is a difference given by the between incident photon energy and binding energy of the electron, so there is energy threshold and it is completely independent on I. Free electron cannot absorb photon, simply because of momentum conservation. Cross section of photoeffect $\sigma_{p.e.}$ is energy dependent (as for other photon processes), it falls as energy of photon rises. There are small edges for this distribution corresponding to different shells, where can electron exist and therefore energy thresholds for k-shell, l-shell etc. could be seen. Cross section of photoelectric effect after some assumptions on E_γ could derived from Born approximation. Materials with higher Z are more suitable to induce photo effect because of high dependence of $\sigma_{p.e.}$ on charge $\sigma_{p.e.} = Z^5 E^{-3.5}$ (closer to k-shell $\sigma_{p.e.} = Z^{4.5} E^{-3}$).

Compton scattering

Conversely to photoelectric effect, Compton scattering is reaction of photons with free electrons. Electrons in material are always bound, but when photons energy is larger than bounding strength of electron, it could be treated as free. With the use of the QED, formula for cross-section could be obtained. It is usually denoted as Klein-Nishina formula. Distribution of electrons recoiled by Compton scattering has a sharp peek in maximum at energy electrons can have, then the drop falls down to zero, known as Compton edge. Cross section for Compton scattering is proportional to $\sigma_C = Z/E_\gamma$, if E_γ is higher than electron rest mass energy. When incident photon doesn't have enough energy to participate in Compton scattering, classical reaction comes into a place, namely Thomson and Rayleigh scattering. In both cases photon interacts with atomic electron or whole nucleus. Thomson scattering is classical limit of free electron and photon interaction with cross section of $\sigma_T = 8\pi r_0/3 = 0.665$ b, where $r_0 = \alpha/m_e$ is classical radius of electron. When photons collide with whole atom coherently, not only with atomic electron, we call the process Rayleigh scattering. Both of above mentioned classical processes do not transfer any energy from photon to electron or whole atom, only thing that changes there is direction of photon after scattering.

Pair production

When a photon with energy slightly greater than rest mass of two electrons meets a electric field it has probability to create electron-positron pair. This process is affected by screening of nucleus by electrons. Energy threshold for electron pair production twice less then in the field of electron. Pair production could be formally described in the similar way as bremsstrahlung. In MeV energies region, cross section for pair production is proportion to $\sigma_P \approx Z^2 \ln(2E_\gamma)$. Photons together with electrons and positrons can produce EM shower. Showers are result of bremsstrahlung of photons by electrons or positrons in matter combined with production of electron-positron pairs by photons. When incident energetic photon, electron or positron travels in medium, it produces cascade of new EM particles, until energy of photons created by radiation is under threshold of pair production. Below this energy electron-positron pairs and photons will lose their energy in other reactions. Development of cascade shower is statistical process. Simple model describing the mean number of particles produced and their mean energies as a function of X_0 will be introduced now. If one begins with energetic photon, after one radiation length it transforms into electron-positron pair and then after another radiation length both electron and positron radiate energetic photon and so on. Number of particles after k radiation lengths is 2^k each with average energy $E(k) = E_0/2^k$. This model is simple and only gives basic idea of electron-photon shower propagation properties.

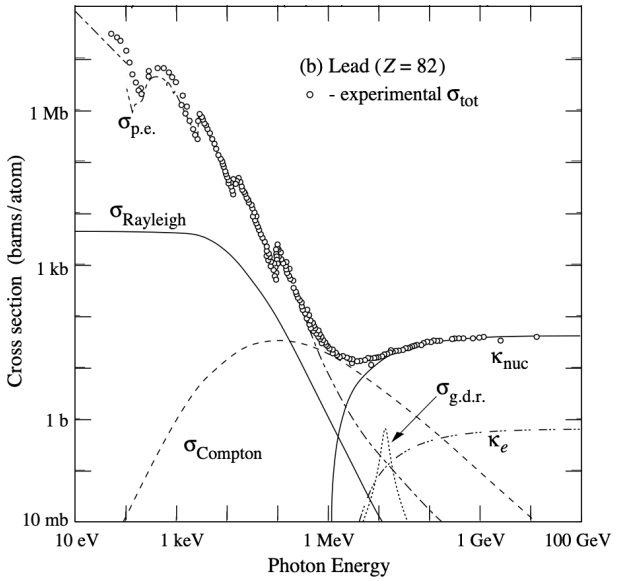

Figure 2.3: Total photon cross section for photon interaction with lead [40].

Neutrons

Neutron is neutral particle, so it doesn't participate in the Coulomb interaction. However it has nonzero magnetic moment, because its constituents are charged. As other particles, reactions are dependent on energy of neutrons. Most significant reaction in MeV range is elastic scattering with material's nuclei. This process is used for moderating (slowing down) neutrons. They can also excite whole atom or knock out another neutron and hence transform atom to different isotope. When its energy is very high (hundreds of MeVs) hadron shower can be produced. Neutron could be absorbed by target nucleus, when energy of neutron is lower than 1 MeV also other nuclear reaction such as (n, p), (n, d) or (n, t) could take place. When neutrons have thermal energy they can also induce fission. Term thermal neutron comes from mean energy of neutrons with temperature of 20° this equal for energy of 0.0253 eV. Thermal neutron cross section for absorption is known as 1/v law. To easily discriminate between neutrons with different energy it is conventional to call neutrons with energy 1 eV $< E <$ 10 keV epithermal. If they have energy 10 keV $< E <$ 20 MeV they are denoted as fast and faster ones are called relativistic.

2.1 Shielding at hadron accelerators

At the CMS cavern strong radiation field is observed, when the LHC collides bunches of charged hadrons. Electronic components of the detectors have to withstand enormous doses, some sensitive parts have to be even shielded. When one want to shield from mixed radiation field composed from different particle species, it is most conventional to sort them into three groups: photons, charged particles and neutrons. Photons together with light charged particles (electrons or positrons) are constituents of EM cascade, whose cross section grows with Z, so material with large proton number is suitable for shielding from this type of shower. Situation is more complicated in mixed radiation fields. Lead would be effective to shield EM cascade, but it contains many neutrons that could be released by inelastic interaction followed by evaporation. Pions are hadrons and may be charged, so they participate in both EM and strong interaction. They can ionize the material and also undergo inelastic nuclear scattering. When they produce hadronic cascade number of secondary particles with reduced energy is formed. This type of shower could be stopped by iron or tungsten after 10 hadronic interaction lengths even at LHC energies. Muons are not stable particles, but their mean free path is usually in orders of kilometres. The only way how to stop muons is prevent them from being produced. They are usually created in meson decays, so one has to make sure they better interact before they decay (mean free path of energetic charged pions is around 10 m). Generally muons are same as electrons so they participate in same processes. Radiation of photons by charged particle is inversely proportional to mass of particle so it is relevant for muons after their energy exceed 100 GeV. On the contrary if their energy is less than 1 GeV ionization is the only important moderation process.

Free neutron decay time is nearly 15 min, so it has a lot of time to make some damage. They are not slowed down by ionization processes and therefore they can penetrate over relatively long distances. Low-energy neutron scattering is dominated by elastic nuclear collisions with material. From kinematics of such a process it could be seen that most of the energy is transferred if target is as light as neutron, for example proton. Because of this fact hydrogen-rich materials are often good choice

for slowing down neutron. Inelastic collisions have to be also taken into account, so when neutron energy is higher, heavier element can provide a better shielding. When neutron energy is around 1 MeV, the best option to stop it is to use a material with medium weight (such as stainless steel). It has short mean free path for neutrons with this energy, but the problem of neutron multiplication in inelastic events is not important yet. For energies less than 1 MeV, it is convenient to shield by water H_2O, paraffin or polyethylene (both C_nH_{2n+2}). Such materials have a lot of hydrogen atoms, which ensure a lot of elastic collisions and hence a good moderation of neutrons. CMS cavern is shielded by concrete, which is also good shielding material. It can be even doped by some heavier elements to obtain even better attenuation for high energy particles. Neutron could by absorbed by an atom, which is hence transformed to new, possibly excited state. In such a process, neutron with energy 1 eV can possibly induce nuclear excitation resulting in gamma decay with MeV energies.

2.2 Dosimetry quantities

There are different types of quantities characterising radiation field and its effect on material. Radiation field could be characterised by particles it consists of and their energies. It is often described by terms of fluence or flux, being both non-stochastical quantities. Second set of variables describe the medium interacting with such a field. Dosimetric quantities then try to combine these two types of variables. Flux ϕ often called also as flux density or fluence rate at given point is number of particles hitting a sphere, with unit cross-sectional area per unit time with centre in that point (see Fig. 2.4). It can be also equally defined as track-length per unit volume per unit time so unit is $\mathrm{cm}^{-2}\mathrm{s}^{-1}$. Time integral of flux is fluence Φ, so if radiation field is independent on time $\phi \neq \phi(t)$, then $\Phi = \phi(t_1 - t_0)$ [41]. Both ϕ and Φ express the sum of rays or particles incident from all directions. In principle one could measure the flux at any time t and in some infinitesimal volume as a function of energy and of the polar angles of incidence α and β, to obtain two differential fluence rate $\phi''(\alpha, \beta, E)d\Omega dE$.

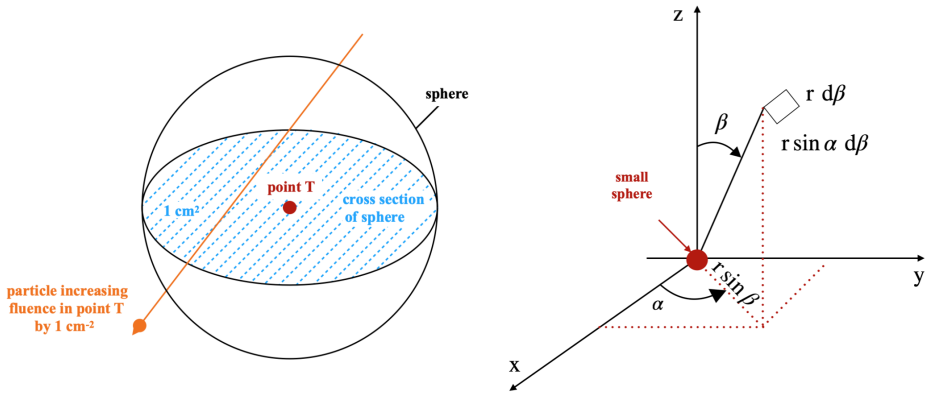

Figure 2.4: Visualisation of particle fluence (left), angular distribution (right).

Properties of matter, when radiation is incident, could be also described by absorbed dose D and KERMA K. Absorbed dose measures the energy deposited by all types of particles in matter per unit mass. It could be also defined as $D = \epsilon/m$, where ϵ is the mean energy transferred by the radiation to a mass m. The unit used to measure absorbed dose is the Gray [Gy]=[J/kg], sometimes absorbed dose measured in rads, where 1 rad = 0.01 Gy. The energy transferred is a stochastic quantity and hence K operates with mean of energy transferred. KERMA (Kinetic Energy Released per unit MAss) K is defined for particles without charge, neutrons and photons. It has the same units as absorbed dose. Photon energy spectrum $\Phi_\gamma(E)$ multiplied by coefficient μ/ρ (μ is photon attenuation coefficient, for given energy and given material with density ρ) integrated over energy gives contribution to KERMA from photons. It could be similarly defined for neutrons.

When radiation is imposed on human body the physical quantity describing it is dose equivalent H_T, which has units of Sv. Equivalent dose (biological dose) represents the stochastic health effects of ionizing radiation on the human body. Its value is calculated as mean absorbed dose $D_{T,R}$ deposited in body organ T, multiplied by the radiation weighting factor W_R, which is dependent on type of radiation. Weighting factor for photons, electrons and muons is 1, for protons and charged pions 2, alpha particles or other fission fragments have weighting factor equal to 20 and finally for neutrons it is continuous function of energy. These coefficients are given by the ICRP (International Commission on Radiological Protection) group, which constantly update and improve their estimates. Effective dose E for human is then

$$E = \sum_T W_T \sum_R W_R D_{T,R}. \tag{2.2}$$

These body-related protection quantities are not directly measurable. For the purpose of radiation protection it is conventional to define quantity $H^*(d)$ called ambient dose at depth d. Ambient dose is measured inside so-called ICRU sphere, made from 30 cm of material similar to tissue. Material contains elements in percentage terms: 76.2% O, 11.1% C, 10.1% H and 2.6% N. Usually is strength of radiation field measured in 10 mm of such a square, quantity could then be calculated as

$$H^*(10) = \int_{E_{min}}^{E_{max}} dE\Phi(E)h^*_\Phi, \tag{2.3}$$

where h^*_Φ is function of energy (for neutrons it is depicted in Fiq. 2.5).

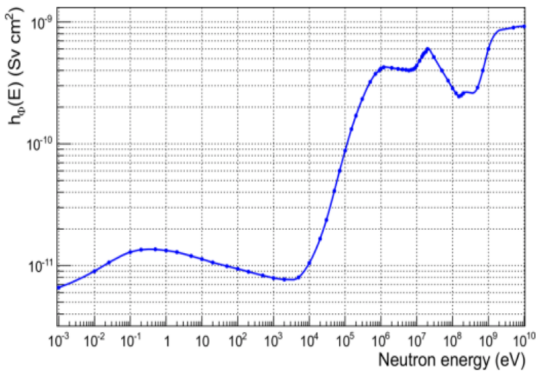

Figure 2.5: Neutron damage to human tissue as function of neutron energy [42].

2.3 Radiation damage

Radiation causes serious damage to particle detectors, the most sensitive ones are tiny silicon parts of electronics. Incoming radiation can induce two types of defects in the semiconductor structures: a ionization and a displacement damage. In the former case absorbed ionization energy frees charge carriers that drift or defuse to other location and there they could be trapped. In the latter case whole atom of silicon is knocked out of the silicon lattice. For example, it could negatively affect V-A characterics.

Ionization damage

Ionization damage is proportional to energy absorbed by the incoming radiation. There are many things that play a role such as voltage applied to the sensor, its temperature or duration of irradiation. Charged particles create electron-hole pairs in silicon volume when they traverse it. Holes have smaller mobility, this means they travel slower in the silicon volume. Because of this fact they can be captured in traps and hence create a bulk of unwanted charge. Ionization causes damage on the surface of the detector. On the top of each semiconductor sensor is SiO_2 layer, because voltage cannot be applied to bare silicon. Holes created by ionization can be trapped in silicon volume and increase its charge or induce creation of the surface generation centers.

Displacement damage

Non-ionization energy losses produce displacement damage in the semiconductor structures. Damage is proportional to the non-ionization energy loss dependent on mass and energy of the irradiating particles. The energy levels in semiconductor detector can be changed by displacement damage. Created mid-gap states in the forbidden gap result in a formation of electron emission or electron capture process. These processes induce dark current in sensors. This means it reduces the current flowing in the conduction band and thus it suppresses detector charge collection efficiency. When radiation has enough energy it can knock out the whole silicon atom. In this process the Frenkel pair constituents interstitial and vacancy is produced. Interstitial is silicon atom allocated from lattice structure and vacancy is resulting hole in lattice. Displacement damage does not have to be permanent because Frenkel pairs have high probability of recombination and this probability is affected by temperature. Annealing is process when temperature ranging from 20° to 70° degrees is applied to sensors. This range of temperatures gives vacancies energy to move and hence increases their chance to find vacancy and recombine. NIEL (Non-Ionizing Energy Loss) hypothesis states that the secondary reaction of the displaced atoms is independent on primary reaction. As was stated above primary reaction differs according to a type and energy of irradiating particles. Using NIEL hypotesis one can scale displacement damage to compare defects caused by several particles within some specified range of energies. Effects are normalised to damage created by neutrons with kinetic energy of 1 MeV.

Displacement damage function $D(E)$ could be seen on Fig. 2.6. Damage efficiency D_{eff} of source with fluence distribution $\Phi(E)$ is computed as

$$D_{eff} = \int dE\Phi(E)D(E) = D_n(1MeV)\kappa \int dE\Phi(E), \tag{2.4}$$

where $D_n(1MeV)$ is dispacement damage cross section of neutrons with energy of 1 MeV (equal to 95 mb), κ is the hardness factor characteristic for the particle type.

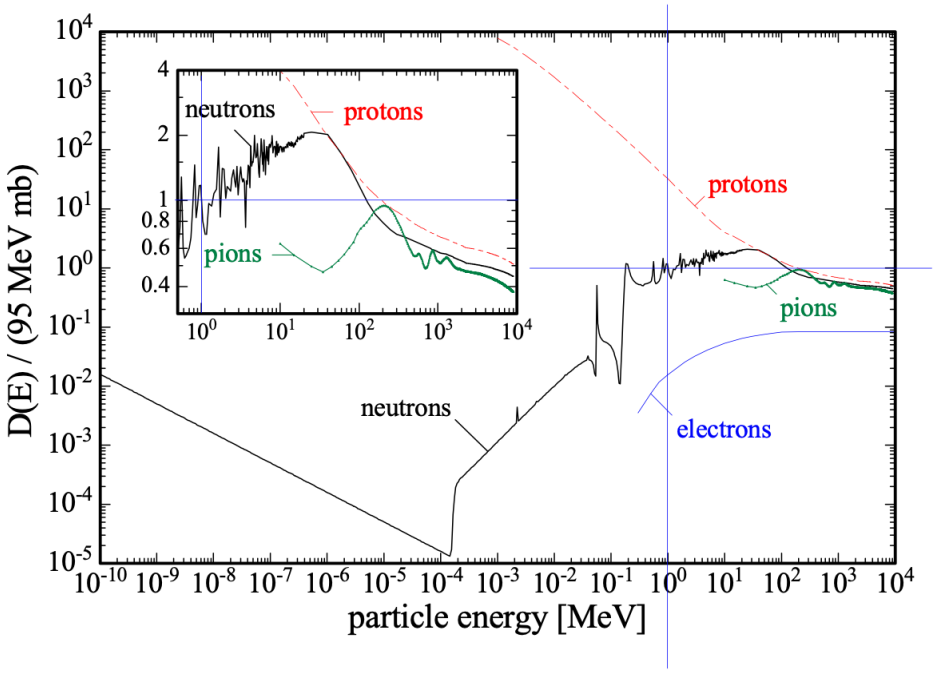

Figure 2.6: Displacement damage function $D(E)$ for different particles [43].

2.4 The radiation transport problem

It is straightforward from previous sections that propagation of particles through matter is rather complicated. Elementary quantity to characterize such a process is number of transported and newly generated particles dN in a position within dr of r with momentum within dp of p at time within dt of t given by $dN = f(r, p, t, \alpha)drdpdtd\alpha^n$, where α is n of other variables such as spin, particle type or charge and $f(r, p, t, \alpha)$ is density of particles in this phase space element. Particle transport problem is to find how introduced particle-number density changes after propagating through a bulk of material. Solving radiation transport problem comprises of solving so-called Boltzmann transport equation a multi-dimensional (> 6) integro-differential equation. Monte Carlo method is very powerful for this purposes. Procedure for solving of Boltzmann transport equation is outlined below. Energy and direction of one particle is initialized. If particle is in vacuum then it is transported to boundary of next material. In the case, when the material is different from vacuum then with respect to particle type and its energy the total cross section is inferred for particle interaction with medium. Then position of first interaction and its type randomly sampled.

Energy loss, change of direction or possibly number of secondary created particles by this interaction is also taken into account. Afterwards, the whole procedure described repeats for all primaries also as for secondary produced particles until particle exits the place of interest or after its energy is less than threshold given by user. All above mentioned is performed using particle transport codes equipped with source of pseudo random number generator and libraries of measured cross sections for wide range of processes of particle interactions with matter.

2.5 FLUKA

The FLUKA is general purpose tool for calculations of particle transport in matter [44]. It is used in many related field such as accelerator science, radiotherapy or rocket science. FLUKA can simulate with high accuracy the interaction and propagation in matter of about 60 different particles, including photons and electrons from few eV to thousands of TeV, neutrinos, muons of any energy, hadrons of energies up to 20 TeV and all the corresponding antiparticles, neutrons down to thermal energies and heavy ions. The program can also transport polarised photons (e.g., synchrotron radiation) and optical photons. Many complex geometries could be defined in FLUKA. External fields such as electric or magnetic field could by applied to simulated particles. In FLUKA single events are simulated, initiated by a primary particle or collision-event. The output is usually averaged over all simulated primary events and normalized per primary event. Many variance reduction techniques are available in FLUKA such as weight windows, region importance biasing as well as leading particle interaction length and decay length biasing. Advantage of FLUKA is also induced radioactivity regard to their decay and the transport of residual radiation. Particle transport and interaction of prompt and residual radiation are simulated in parallel based on microscopic models for nuclide production. The decay radiation and its associated electromagnetic cascade are internally flagged as such in order to distinguish them from the prompt cascade. This allows to put different threshold for residual and prompt radiation and to score both independently. FLUKA uses DPMJET-III as a built-in event generator to create primary pp or ion collisions. The DPMJET simulates interaction of hadrons with electric fields, it is based on PHOJET 1.12, PYTHIA 6.115 and LEPTO 6.5.1. Other big advantage of FLUKA is grapical interface Flair [45], which makes the work with geometry much easier.

Combinatorial geometry

Building blocks of FLUKA geometry are bodies, regions and Boolean operators + (union) , - (difference) and — (intersection). FLUKA gives user wide range of 3D bodies such as sphere, box and cylinder with finite volume. It is also possible to define infinitely long cylinder or plane dividing the 3D space on two distinct regions. Bodies are folded together by Boolean operators to create regions. Regions do not have to be connected, since they can be made of two or more non-contiguous parts, but always have to be of same material composition. All the regions are surrounded by an infinitely absorbing material called "blackhole", which absorbs all particles that hit it. The + operator act like AND, so intersection of two bodies can be produced using it. When one needs to subtract the inside of the body from the rest, - operator is used, which is like the + operator, but the outside of the volume is used. The — operator is like an OR and its used to create one region out of several separate building blocks. Better understanding of bodies and operators could be gained from Fig. 2.7. From these components even very complicated regions could be build. Usually some simplifications are used on some very complex objects. As numbers of region grows, the simulation time increase as well. There are some requirements for geometry, for example two regions cannot overlap, which also means that particle cannot be in two materials at the same time. User has to define material for each region from FLUKA library, materials could be easily created by element composition. User has to define density of the material. Big advantage of FLUKA combinational geometry is lattice function. It allows to use already created object in more places in geometry by a transformation which can be both rotation and translation. When particle arrives to lattice, it is shifted from lattice region via the defined transformation into the fully defined region.

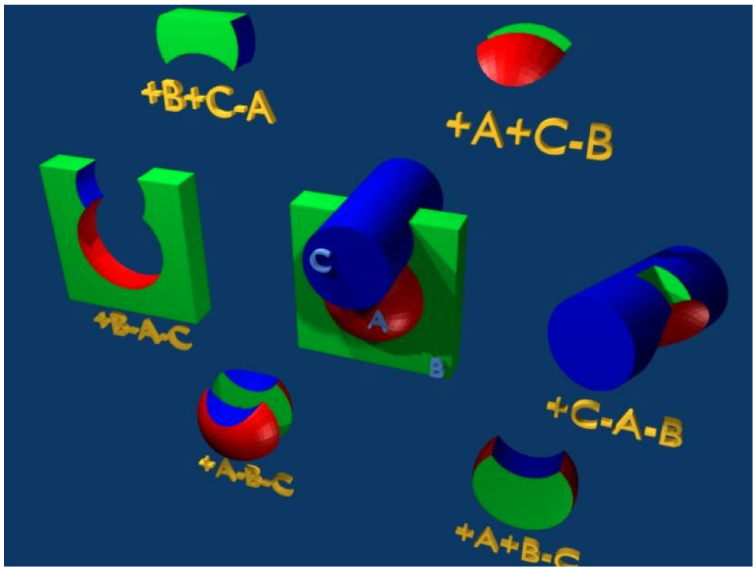

Figure 2.7: Explanation of Boolean operators in FLUKA [46].

Biasing

For a complex geometry with a particular region of interest, biasing techniques can be used to improve statistics without extending the necessary computing time. Biasing has to be mathematically correct and it should not involve any approximations. One defines importance of a region and by number proportional to the contribution that particles in that region are expected to give the desired result: the number of particles moving from a region to the neighbouring one will increase or decrease accordingly to the ratio of importance values assigned to both regions and the particle statistical weight. Nonetheless, a convergence in specific regions of phase space will generally give the disadvantage of a slower convergence in other regions. Due to the fact that an actual calculation does not use an infinite number of particles, but it is necessarily truncated after a finite number of histories, results must be judged accordingly.

Scoring

Before start of a simulation, the user has to define scoring regions, where he is interested in results of simulation. A scoring routine is called when a particle matches the conditions for this scoring. Estimator or also called as detector is designed to estimate one or more radiometric quantities, and the final score is a statistical estimation of the average value of the corresponding population of primary particles. It is possible to calculate standard deviation and induced statistical uncertainty in each estimator. There are many different types of scorings in FLUKA. In this work only two of them were used and will be further described. The most frequently used estimator in FLUKA is USRBIN. The volume of interest is overlaid with a binning mesh. There are several types of binning such as Cartesian, cylindrical or other more complex ones. Scoring is used to obtain particle fluence by calculating the track length density, or dose like values by scoring the energy deposition. Obtained 3D data is projected to two dimensions and shown as a 2D flux map or one dimension, showing change of scored quantity in one coordinate. So-called track length estimation is incorporated in the USRTRACK estimator. This stands for recording length of particle track in selected volume. Track is then normalised to this volume. This technique is better for counting particles in some specific region, because it properly weights particles that enter the region in some small angle or get destroyed or created in the middle of the scoring volume. Both USRBIN and USRTRACK allow to only choose one specific particle type or group of particle types such as neutral hadrons or electromagnetic particles (electrons, positrons and photons). FLUKA gives possibility to weight each particle type and gain ambient dose equivalent or 1 MeV neutron equivalent.

Chapter 3

CMS detectors for neutron/radiation monitoring

3.1 LHC RadMon

Most of the electronic systems of the LHC are located in underground areas, where radiation field is expected. The LHC Radiation Monitor (RadMon) was developed at CERN in the EN Department. LHC RadMon device offers online measurement of radiation and warn operators in control room about leakage of radiation. There is more than 400 RadMon detectors around LHC [47]. It is fully commercial system, which is radiation tolerant enough to withstand doses of particles even in experimental cavern. Two versions of RadMon are installed in the accelerator complex: V5 and V6 [48]. The V5 version monitor consists of nine sensors, 2 radiation sensitive p-channel MOS-FETs (RadFETs) with different oxide thickness (100 nm, 400 nm and 1000 nm), two RadFETs and two p-i-n diodes and SRAM memory, allowing to measure SEU (Single Event Upsets), 3 photodiodes and a Toshiba SRAM memory.

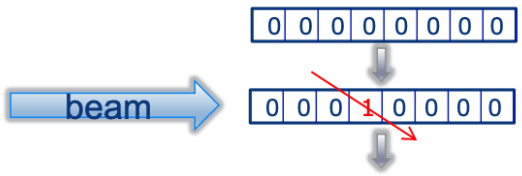

Figure 3.1: Single Event Upset measurement with LHC RadMon SRAM memory [49].

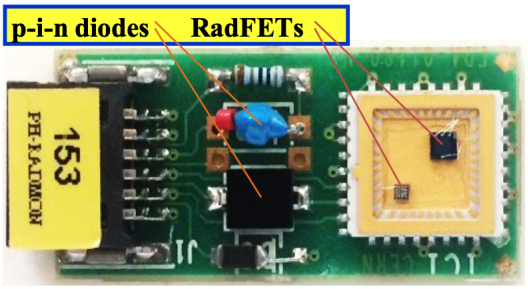

Figure 3.2: Photo of LHC RadMon detector [49].

RadFETs provide information about absorbed dose D. RadFET's gate threshold voltage V_{th} changes because of incoming radiation. Then shift of threshold voltage is $\Delta V_{th} = aD^b$, where a and b are coefficients dependent on the RadFET type as well as on the measured dose range. The p-i-n diodes forward voltage V_F changes, when radiation field is present. 1MeV equivalent particle fluence $\Phi_{neq}^{1\ MeV} = C\Delta V_F$ is proportional to forward voltage shift and c is proportional constant measured for each p-i-n diode. Single event upsets induced by hadrons with energy bigger than 20 MeV can be measured with SRAM memories. Hadron can induce a bit flip in the data stored in a memory, if number of flips is counted and cross-section for this process is known, then fluence of high energy hadrons Φ_{HEH} (hadrons with energy greater than 20 MeV) could be inferred [50]. These memories become more sensitive to thermal neutrons when they are operated at lower bias voltage compared to higher one. The most recent version of the RadMon is called V6. Improvements include: higher radiation tolerance (more than 200 Gy), modular architecture for easy replacement of part and updates and remote configuration.

3.2 REMUS

The REMUS (Radiation and Environment Monitoring Unified Supervision) also called RAMSES detector is dedicated to measure $H^*(10)$ in underground areas of LHC. It provides online measurement of the residual radiation from activation during shutdown as well as the so called prompt radiation during collisions. This they operate with a large dynamic range. It is primarily used in shutdown periods by the CERN radiation protection groups and the CMS technical coordination with the aim of ensuring it is safe to enter the CMS cavern. There are various types of REMUS detectors, BRIL group uses the ones in the CMS cavern called PMI. BRIL uses the online results during collisions for cross check against other luminosity monitors and to measure the cavern background. These are gas filled ionization chambers. Charged particle produce electron-ion pair when it traverse gas active volume. There are three litres of air with atmospheric pressure. The air is surrounded by 4 mm thick PE graphite coated wall see Fig. 3.3. A photo from cavern is in Fig. 3.4.

3.3 Bonner sphere with SiPM

Bonner sphere is device able to determine the energy spectrum of a neutrons in wide range of energies. Principle of operation was used first by Tom Bonner in 1960s [53]. Bonner spectrometer consists of spheres with different sizes made out of moderating material (polyethylene in this case) with scintillating detector inside each sphere. Thermal neutron detector (ZnS(Ag)/$_6$LiF scintillator) is capable of measuring neutrons from thermal to GeV. By measuring the count rate with each sphere individually, an unfolding procedure provides information about the energy distribution of the incident neutrons. Detection with $_6$Li-enriched scintillator coupled to silicon photomultiplier (SiPM) rely on $_6$Li(n,α) reaction. It has high cross-section for neutrons with energy smaller than 10 MeV [54]. The emitted alpha particle is counted by scintillator. A SiPM is a semiconductor photodetector, where pixels are joined together on a one silicon substrate. Advantages of this monitor is an insensitivity to the magnetic field, a low bias voltage, a compactness in size, a robustness and a low cost. Radiation hardness of SiMP was studied by CMS

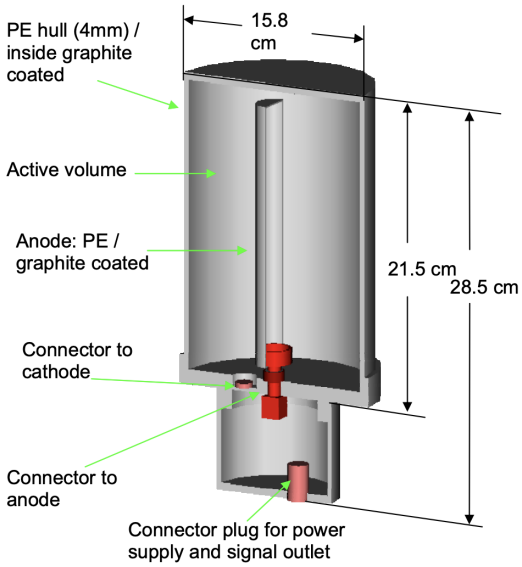

Figure 3.3: Scheme of REMUS detector [51].

Figure 3.4: Photo of REMUS detector in CMS cavern [52].

Collaboration [55]. It was found that fluence of 1 MeV neutrons $\Phi_{neq}^{1\ Mev} = 10^{12}$ cm^{-2} is limit for SiMP technology at room temperature. Above this limit dark current starts growing up rapidly and dark counts are observed. The most radiation-tolerant SiPMs were found to be those with the smallest pixel ($10-15\ \mu m$). It is intended that they will be replaced during appropriate technical stops before they reach critical levels of radiation damage. The Bonner sphere spectrometer in the CMS cavern will consist of six moderating spheres with diameters of 76 mm, 81 mm, 108 mm, 133 mm and 178 mm. Four of them will be placed at the vertices of the square while the fifth and sixth will be located in its center.

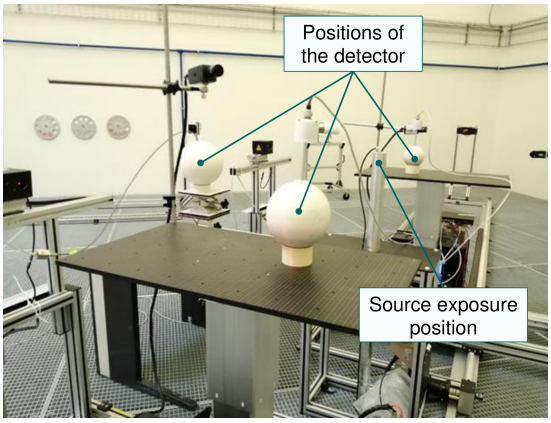

Figure 3.5: Calibration in the CERN calibration facility [52].

Figure 3.6: Photo of the Bonner sphere spectrometer during Run 2 in the CMS cavern [56].

3.4 GFPC

GFPCs (Gas Filled Proportional Chambers) are very well known devices capable to detect charged particles and to estimate particle energy. Proportion in its name means that it produces signal proportionally to energy deposited by particle. They can also detect neutrons when one covers them by a layer of material, which contains element having high cross section for neutron interaction. GFPC's used in the CMS cavern consist of six inch thick cylindrical polyethylene layer for moderation of neutrons, which occupy a corona counter SNM-14 a thin-wall (0.3 mm) cylinder with a diameter of 188 mm and length of 154 mm. The internal surface of the counter is covered with the $_{10}B$ isotope. The counter is filled with argon at atmospheric pressure. A signal is formed mainly after ionization of argon by ions created by neutron and boron collision products. Operation of the chamber in proportional mode requires the high voltage supply be precise and stable, and this is satisfied by the built-in electronics of the monitors. The use of the proportional operating mode reduces both the deadtime and the power consumption of the monitor.

HF RadMon

The HF radiation monitors have been installed around HF since Run 1. Scheme of the detector could be seen in Fig. 3.7. They measure neutron fluence, which could be compared with the degradation of HF fibers, electronics, and PMTs in HF. HF RadMons are calibrated with reference neutron field of AmBe source. Signal from detectors could be understood as neutron fluence density expressed as a number of Am-Be source neutrons [56].

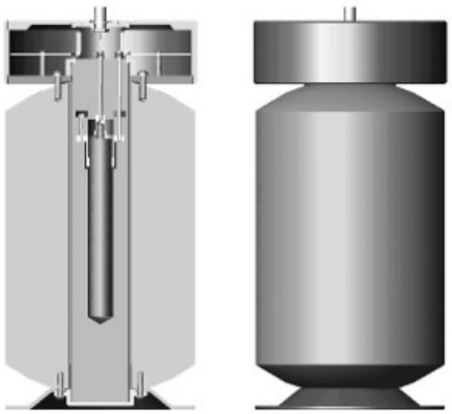

Figure 3.7: Scheme of HF RadMon monitor [56].

GFPC full and light versions

For Phase 2 will be GFPC monitors made in pairs. Single monitor cannot investigate wide range of neutron energies. There will be the Main detector and Complementary detector. The complementary detector does not contain any radiator, and the moderator material is polystyrene . Whole pair is denoted as GFPC full option and only main detector is labeled with GFPC light.

Chapter 4

Radiation environment in CMS cavern

Investigation of radiation field in the CMS cavern is important task that allows to predict a damage to detector sensitive elements or schedule workload in the CMS hall. Firstly some general features of the field will be described. The CMS central detector is mostly symmetric in r and ϕ and radiation field follows such a trend. When bunches of particles collide most of the new particles are produced in forward directions. For this reason higher flux of particles could be seen in end-caps than in barrel region. The vast majority of charged particles is stopped by calorimeters. In the forward region is beam filtered of collision product and beam particles which lost part of their energy in elastic collision. Those particles persist to have relativistic energies, so when they interact with collimating material shower of particles are produced. These regions are shielded but gaps and the practical constraints that limit the ability to fully attenuate the high amount of radiation produced, means these components are still main source of background radiation in cavern. The fluence of all particles shown in Fig. 4.1 demonstrates the pattern of radiation in the CMS cavern.

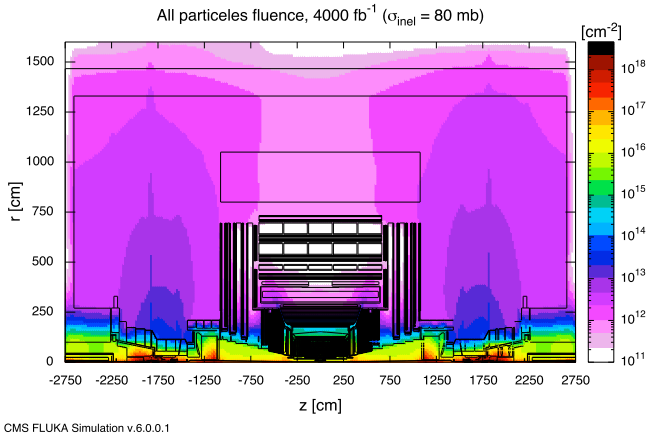

Figure 4.1: All particles fluence recorded in 2D r-z mesh averaged over 360° in ϕ. Leakage of radiation from rotating shield in $z = \pm 1750$ is clearly visible. The slight asymmetry in z is due to the large shaft adjoining the cavern walls on the negative z end, which results in fewer neutrons reflected back into the cavern.

Particles with charge cannot penetrate material as easily as neutral particles so the main contribution in cavern comes from neutrons and photons. The ratio of neutrons and photons to all particles is on Fig. 4.2 and Fig. 4.3. It could be seen that neutrons (photons) account for around 65% (34%) of all particles. All charged particles contribute only by 1% to fluence from all particles in cavern.

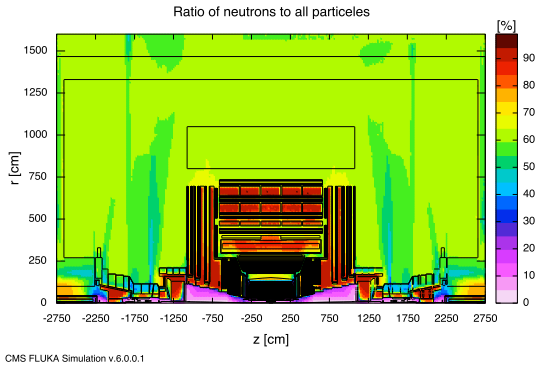

Figure 4.2: Neutrons to all particles.

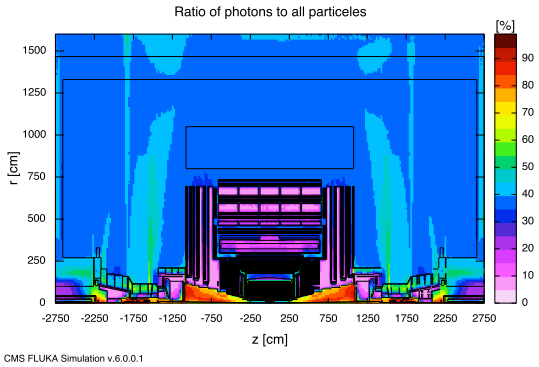

Figure 4.3: Photons to all particles.

Normalization

In a standard FLUKA output, results are normalized to one primary event (in this case a proton-proton collision), so a normalisation has to be applied to provide meaningful values. When one is interested in flux of particles (i.e. a rate), results are normalised with instantaneous luminosity. When LHC nominal luminosity $\mathcal{L} = 10^{34}$ cm^{-2}s^{-1} is multiplied with the expected inelastic cross section $\sigma_{inel} = 80$ mb one can calculate that this corresponds to approximately 800 million collisions every second. When radiation field is studied in longer time perspective number of particles is calculated with respect to integrated luminosity. It is predicted that by the end of its lifetime, the CMS experiment could receive a maximum integrated luminosity of 4000 fb^{-1}. Since RadSim is typically concerned with detector longevity, it is a conservative approach to normalize to all Phase 2 predictions to this value. When this value is multiplied with the inelastic cross section, $\sigma_{inel} = 80$ mb, one finds this responses to a total of 3.2×10^{17} collisions.

CMS FLUKA geometry

The systematic uncertainty of performed simulations rely on accuracy of geometry model. It is nearly impossible and not desirable in terms of manpower and CPU time to include each piece of material in cavern to the CMS FLUKA model. The detail required depends on the region and output quantity of interest. The most important is the central detector of CMS. The model of CMS cavern is continuously improved where necessary, and updated with detectors and components in the experimental hall are upgraded. Subdetector projects and the CMS integration office are responsible for providing mechanical drawings, and material budgets which are simplified and implemented into the CMS FLUKA model by the BRIL RadSim group. Three models are currently maintained to reflect the different CMS and beamline configurations in different time periods; a Run 2 model is maintained for benchmarking purposes, and a Run3 and a Run 4 model for future estimates. Any simulation with geometry model update had an associated version tag. Simulation v4.0.1.0, uses a geometry model with the CMS detectors based on a Run 2 detector and beampipe configuration as described in the first Chapter. The geometry models for Run 3 and Run 4 will be described in following subsections but only changes relevant for this work will be mentioned.

Geometry Model for Run 3 Simulations; v5.0.0.3

The CMS FLUKA Run 3 model [57] contains a set of recent improvement style updates also made to the Run 2 model including the adjustments to the concrete cavern walls to include asymmetrical shape and recent update to first quadruple magnet and rotating shield region. These are particularly important for estimates of the cavern background. The main CMS detectors are identical to those in Run 2, although several BRIL detectors were added e.g. beam monitor BCML2. The most long shutdown 2 upgrades implemented for the Run 3 model were the following: the modification of the beampipe from the IP to z $\approx$ 15.7 m to represent the replacement of this part in LS2; the addition of part of the support structure for the VAX equipment inside the RS which involved partial removal of steel to accommodate this , and various insertions (borotron + steel) for thin part of RS. Physical modifications to the vacuum chamber and rotating shield structures are important to include in the geometry model as they influence the shower development and leaking into the CMS cavern.

It is anticipated that an external shield will be added outside the thin and conical parts of the RS to further suppress the cavern background. However the design is not yet finalized, thus it is not included in the Run 3 (or Run 4) simulations in this thesis.

Geometry Model for Phase 2, Run 4 Simulations v6.0.0.1

The CMS FLUKA geometry representing a Run 4 configuration was recently updated. This involves a substantial update to the CMS central detectors which will be upgraded in LS 3. The entire CMS endcap region is replaced with newly designed detectors and the inner envelope will reach a higher pseudorapidity range. Relative to the Run 3 model there are modifications to the beampipe, the inner TAS radius is increased from 1.7 to 3.0 cm, and LHC VAX equipment and support structures are added inside the rotating shield region. The components with biggest impact on the radiation environment in the cavern are the forward components. Fig. 4.4 and Fig. 4.5 offer geometry view from Flair of shielding between HF and Block house with v5.0.0.3 and v6.0.0.1 geometries. It could be seen that vacuum equipment is upgraded in latter version.

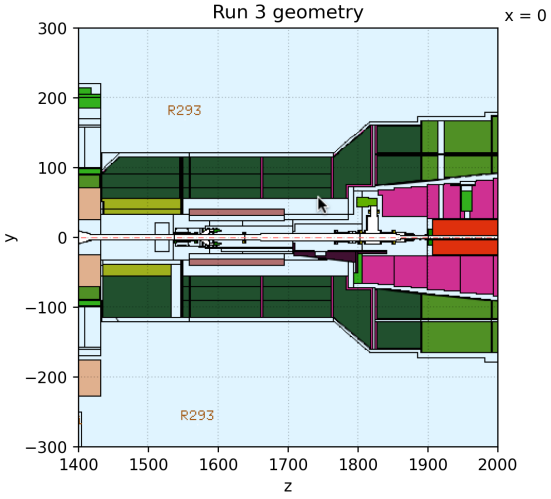

Figure 4.4: Forward region of the CMS FLUKA Run 3 model used in simulation v5.0.0.3

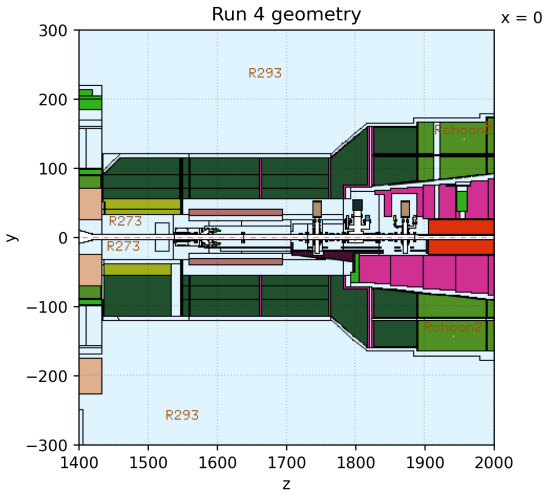

Figure 4.5: Forward region of CMS FLUKA Phase 2, Run 4 model used in simulation v6.0.0.1

4.1 Run 3 vs. Run 4 simulation study

The CMS FLUKA geometry versions for Run 3 (v5.0.0.3) and Phase 2/Run 4 (v6.0.0.1) were described in the previous section. For both models many simulation have been preformed to fulfil the requests related to radiation predictions in the CMS cavern. Before describing of work towards the BRIL TDR (Technical Design Report) in the next section, an example of the changes in the expected radiation field in the CMS cavern from Run 3 to Run 4 is presented. As both models are newly developed, general comparisons are under study, however in the context of the BRIL Phase 2 TDR work energy spectra of various particle types were recorded in particular locations ultimately using the Run 4 model but had also been included in a Run 3 simulation.

As a key difference between models is in RS region, the neutron spectra at the balcony at the same z location were selected for comparison. In Fig. 4.6 and Fig. 4.7 the neutron spectra in BALC3 and BALC4 respectively for Run 3 and Run 4 is plotted (position of these scoring regions is in Tab. 13). For Run 4 the expected instantaneous luminosity will be substantially higher, as is the expected integrated luminosity. Thus to make a direct comparison of the geometry models both are normalized to 1 fb^{-1}. Despite the extra components and corresponding cut out of the shield, the expected neutron fluence per collision is reduced in Run 4. This is likely due to the increased aperture of the TAS, shown in red in Fig. 4.4 and Fig. 4.5, which is the main source of secondary showers within the RS region.

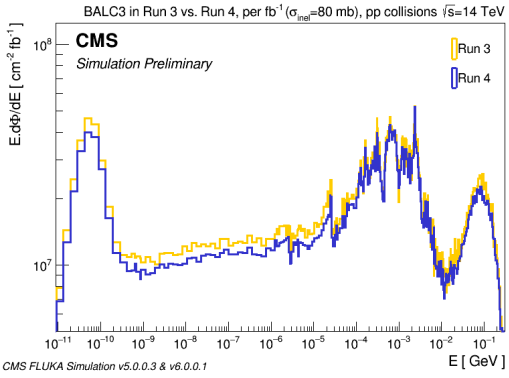

Figure 4.6: Neutron spectra in BALC3 region simulated with Run 3 and Run 4 geometry normalised per fb^{-1}.

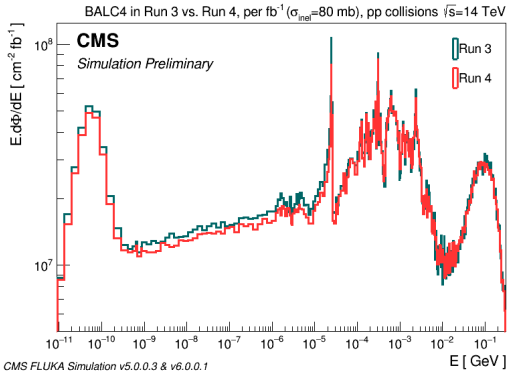

Figure 4.7: Neutron spectra in BALC4 region simulated with Run 3 and Run 4 geometry normalised per fb^{-1}.

4.2 Work towards the BRIL TDR

The main purpose of this work is to simulate quantities characterising radiation field in the CMS cavern in locations proposed for monitors in Phase 2. Two main simulation tasks were required, firstly predict integrated radiation quantities for whole list of locations provided (from Tab. 7 to Tab. 12) and secondly to estimate energy spectra of various particle types to better understand the radiation field at monitor locations. A few key locations were selected as predicted energy spectra at precise monitor locations is not necessary at this stage and it is sufficient to understand the field at the approximate region. This enable the recording of spectra in large volumes this enabling better statistical uncertainty. The main purpose of the simulations was to define the sensitivity and dynamic range requirements for the radiation monitors in Phase 2, thus a Run 4 geometry versions was used for the final TDR simulations. Simulations were also performed for Run 3 for comparison. Radiation environment predictions for the stability of materials and electronic equipment in terms of damage are based primarily on Monte Carlo simulations. Quantities considered as important for accomplish all requirements will be stated now. Safety to the personnel must be insured in all cases. Ambient dose equivalent $H^*(d)$ is crucial to manage work activities in the cavern shutdown. Whilst the REMUS monitors measure $H^*(d)$, during operation they are mostly expose to neutrons and thus signal can be approximated with absorbed dose in Gy. Relevant quantifiers for the proposed monitors are absorbed dose D and 1 MeV neutron equivalent in Si $\Phi_{neq}^{1\ MeV}$ and fluence of hadrons with energy greater than 20 MeVs (high energy hadrons) Φ_{HEH}. The CMS cavern is full of electronic devices. Radiation hardness of each devise should be considered before placing it in experimental hall. Radiation effect on electronic devices could be predicted from SEU (Single Event Upset) rate measurements. In following two subsections neutron and radiation monitoring will be further described.

Neutron monitoring

As was shown in Fig. 4.2 neutrons are the main constituents of radiation background in CMS cavern. They cause serious damage to external parts of muon chamber, by photons produced in nuclear capture of slow neutrons. Source of neutrons are partly cavern walls made out of concrete. Energy of neutrons range from thermal to few GeVs in cavern. Single type of detector is not able to measure neutrons in whole range, but rather combination of detectors tuned to narrower energy ranges is used. Contributors to neutron monitoring are: CMS Electronics Coordination interested in $\Phi_{neq}^{1\ MeV}$, CMS Radiation Protection and Safety for the complex geometry model validations, Muon community needs to control flux of neutrons in muon endcap electronics racks and inside GEM volume. Plan is to use monitors described in previous chapter. Only neutron monitor able to deliver energy of neutrons in CMS cavern is Bonner sphere detector with SiMP. Proposed locations are in Tab. 12 and simulated quantities are marked in Tab. 18. As was described in previous chapter set spheres occupy volume of approximately 0.5 m^3 so where is not enough space other monitor has to be used. The p-i-n diodes of LHC RadMon detector are suitable for the areas with limited space. Proposed locations are in Tab. 9 and simulated quantities are in Tab. 16, Tab. 15 and Tab. 17.

Last but not least are GFPC monitors in two versions. GFPC full at locations and results of simulation with CMS geometry $v5.0.0.3$ in Tab. 19 and $v6.0.0.1$ in Tab. 20. GFPC light at locations in Tab. 10 and results of simulation with in Tab. 21. There are other monitors able to detect neutrons that will be used in Phase 2, but they can also measure other particles so they are labeled simply as radiation monitors.

Radiation monitoring

There are other particles in the CMS cavern radiation field, which have to be monitored as could be seen in any of Figures 25 - 48. Stakeholders of radiation monitoring are Technical Coordination and Electronics Coordination. Technical Coordination has to ensure safe access to cavern. Two types of detectors persist over the last two runs and will continue in Phase 2, namely REMUS detector and LHC RadMon. Ambient dose equivalent will be measured using REMUS detector discussed in the previous chapter. List of proposed locations of REMUS detectors is in Tab. 7 and results of simulation are in Tab. 14. LHC RadMons provide set of quantities. They are able to measure high energy hadron fluence, SEU rate and absorbed dose. Tables with LHC RadMon locations and simulation output are in Tables 20, 19, and 21. From proposed locations maximal and minimal values are extracted for each scored quantity in Tab. 4.1.

	Min	Max
D [Gy]	0.90±0.15	96±4
Φ_{HEH} $[cm^{-2}]$	(5.6±0.9)×10^{6}	(1.05±0.01)×10^{12}
$\Phi_{neq}^{1\ MeV}$ $[cm^{-2}]$	(3.75±0.07)×10^{10}	(3.49±0.01)×10^{12}
$\phi_{neq}^{1\ MeV}$ $[cm^{-2}s^{-1}]$	(1.36±0.03)×10^{2}	(4.37±0.01)×10^{4}
Φ_{neut}^{th} $[cm^{-2}]$	(3.56±0.08)×10^{10}	(4.50±0.01)×10^{12}

Table 4.1: Summary table to define the dynamic range requirements of monitors in terms of various simulated quantities. For each quantity, the maximum and minimum values are obtained from all monitor locations. Integrated values are scaled for 4000 fb^{-1} and neutron flux for instantaneous luminosity 5×10^{34} $\text{cm}^{-2}\text{s}^{-1}$.

Last but not least goal was to simulate energy spectra for all relevant particles in radiation monitor locations. To accumulate statistically good results in a finite time, one has build scoring regions sufficiently big. The bigger a volume of the region is the more particles should reach it, so statistical uncertainty becomes less relevant. On the other side when scoring region is too big it cannot show trends of radiation field precisely. It was decided to build only 25 spectra scoring regions (there is 100 proposed monitor locations) at key locations see Tab. 13 together with visualisation of regions in Figs. 20-24. Firstly proposed locations are not final yet, secondly it would take too much of CPU time. When it was possible (because of free space) the scoring region volume was set to 1 m^3. Because CMS geometry model is symmetric in z (it is made by lattice function in FLUKA), scoring regions occurs symmetrically in both $\pm z$ sides. Because of this fact additional 1/2 have to be applied to normalisation, because when one makes scoring region with volume of 1 m^3, in fact particle are counted in regions on both sides of IP. Energy spectra could be sorted to central regions, where doses of particles are usually higher and balcony regions where opposite is true. In Fig. 4.8 (Fig. 4.9) neutron energy spectra for central (balcony) regions.

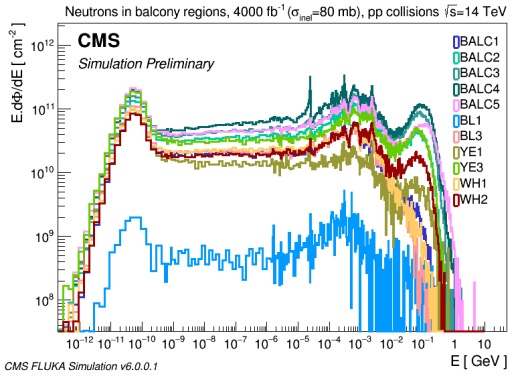

Figure 4.8: Energy distribution in balcony regions.

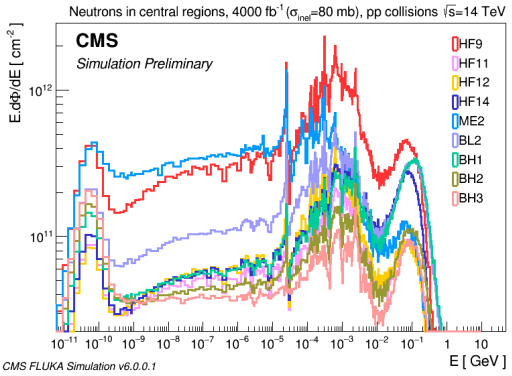

Figure 4.9: Energy distribution in selected central regions.

4.3 Benchmark with HF RadMons

In this section Run 2 data from GFPC monitors placed inside and outside of HF calorimeter (they are also called HF RadMons) are compared to FLUKA predictions. Detector names for external (X) and internal (I) monitors or top (T) and bottom (B) are chosen to be easily recognized. The scheme of the detector locations is shown in Fig. 4.10 together with photo from cavern in Fig. 4.11 and positions with names and measured values are in Tab. 4.2.

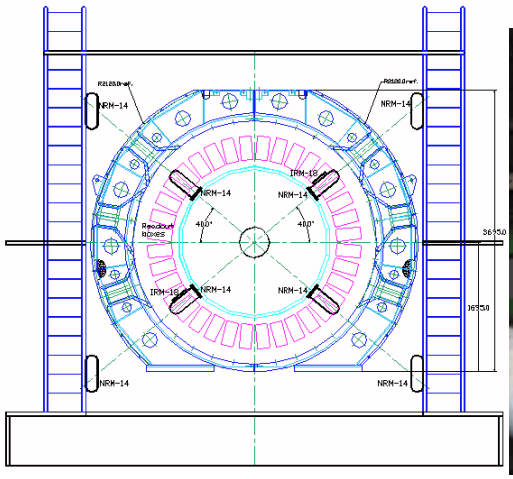

Figure 4.10: Scheme of HF RadMon monitors [52].

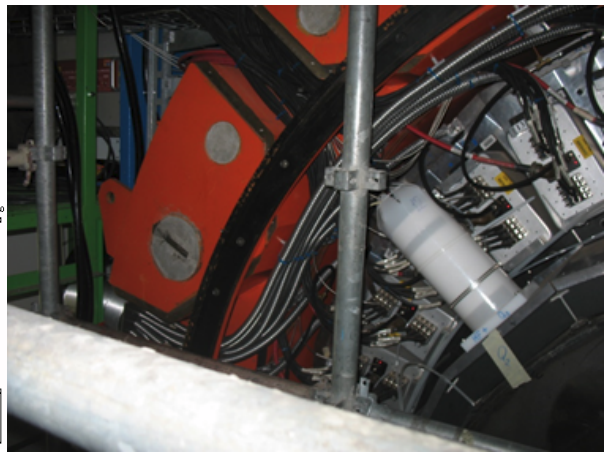

Figure 4.11: Photo of MFIT monitor [52].

Detector	$x[cm]$	$y[cm]$	$z[cm]$	Φ $[cm^{-2}\mu b^{-1}]$ (13 TeV, 2017)	Φ $[cm^{-2}\mu b^{-1}]$ (13 TeV, 2018)	Φ $[cm^{-2}\mu b^{-1}]$ (5 TeV, 2017)
PFIT	-92	92	1390	3.65	3.25	1.95
PFIB	-92	-92	1390	x	x	x
PNIB	92	-92	1390	4.5	4.15	2.42
PNIT	92	92	1390	3.62	3.22	1.82
MFIB	-92	-92	-1390	4.33	4.2	2.31
MFIT	-92	92	-1390	x	3.17	x
MNIB	92	-92	-1390	4.25	4.12	2.27
MNIT	92	92	-1390	3.41	3.12	1.85
PFXT	-179	179	1220	0.27	0.27	x
MFXT	-179	179	-1220	0.25	x	x

Table 4.2: Positions of HF RadMons, x,y and z denotes distance from IP. Number of neutrons per cm and per μb in 2017 and 2018 with centre-of-mass energy equal to 13 TeV and 5 TeV [58].

In order to compare already mentioned data two sets of simulations were performed with Run 2 CMS geometry model. Simulation with centre-of-mass energy equal to 13 TeV has tag $v4.0.1.6$ and 5 TeV simulation is labeled with $v4.0.2.0$. Both simulation runs differ only in colliding energy. Scoring regions for spectra scoring were created in existing air regions. CMS FLUKA model is almost symmetric in z, so scoring regions were created symmetrically in z using lattice card. Because of this we cannot distinguish between negative and positive side of CMS detector. In first round of simulations was hollow cylinder region of inside monitor chosen. Then was region divided into regions as could be seen on Fig. 4.12. Sensitive volume of real monitors is cylindrical and very small. It would take long to gain good statistic in such a small volumes. Hence scoring region was made in the way that it is sufficiently big and it catches features of radiation field in HF region. Each of the internal detectors is $z = 1395.5 \pm 16.5$cm and $r = 128.5 \pm 22.5$cm, then was cylinder divided into 12 same parts and four of them were chosen to be scoring regions for internal detectors. Air scoring region for external monitor is show in Fig. 4.13 as rectangle shape region in $x = -200 \pm 50$ cm, $y = 260 \pm 50$ cm and $z = 1220 \pm 50$ cm above external shielding layer. The pictures are made as screenshot from Flair graphical interface and labels are done using short Python macro, names of regions are written in pink.

After two weeks of simulations were gained 0.5 million primaries for 13 TeV run and 0.4 million primaries for 5 TeV run. Neutrons with kinetic energy between 0.01 eV and 10 GeV were scored. To crosscheck $d\Phi/dE$ output from USRTRACK scoring, also integrated Φ $3D$ map was simulated with USRBIN card with 2 cm bins in r, 1 cm bins in z and 12 bins in ϕ. Those could be seen in Fig. 4.14 for 5 TeV simulation and Fig. 4.15 for 13 TeV simulation.

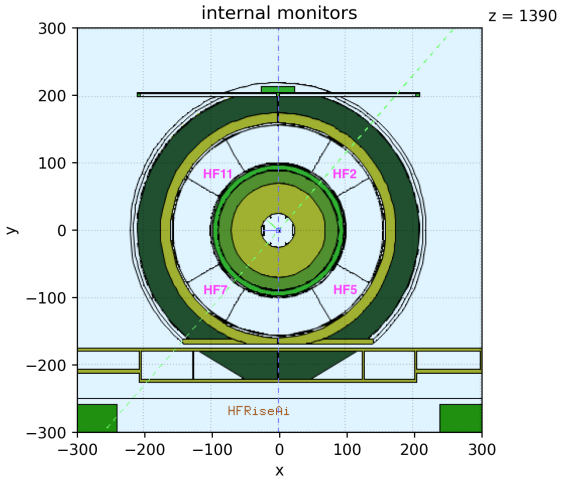

Figure 4.12: Scoring regions for internal detectors.

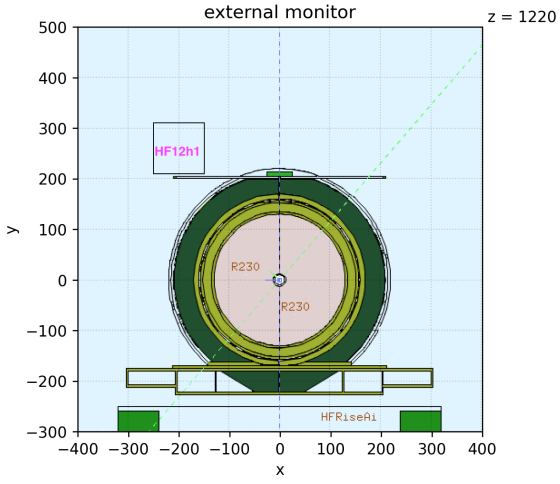

Figure 4.13: Scoring regions for external detector.

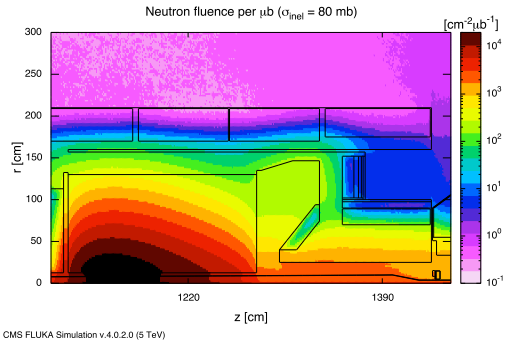

Figure 4.14: Neutron fluence per μb with 5 TeV simulation. Results are averaged over full ϕ.

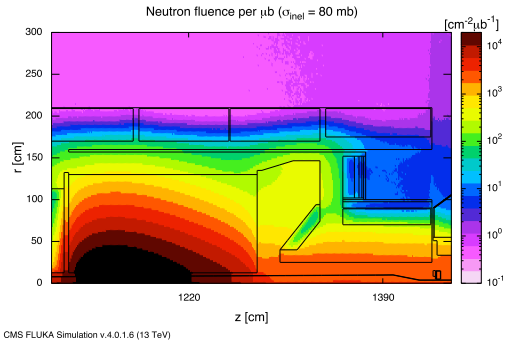

Figure 4.15: Neutron fluence per μb with 13 TeV simulation. Results are averaged over full ϕ.

It could be seen that trend is similar for both centre-of-mass energy, but the absolute values for neutron fluence are higher for the 13 TeV center-of-mass simulation. A ϕ asymmetries in HF region are likely caused by reflections from the symmetric cavern, floor and cavern elements and vertical gaps in the center of the HF detectors. As mentioned in previous chapter, precision of monitors rely on calibration them in a radiation facility. HF RadMons were calibrated with AmBe source at Radiation Protection calibration facility at CERN. This calibration has to be taken into account in order to properly analyse measured data. It is only know how monitors respond to AmBe source, while their operation can differ in radiation field of CMS cavern. Because of this fact calibration coefficient k_{cal} have to be computed. Difference between expected fluence Φ_{exp} and simulated fluence in FLUKA denoted as Φ_{FLUKA} is

$$\Phi_{exp} = k_{cal}\Phi_{FLUKA} = \frac{\int \frac{d\Phi_{FLUKA}(E)}{dE} R(E)dE}{\int \frac{d\Phi_{AmBe}(E)}{dE} R(E)dE}\Phi_{FLUKA}, \tag{4.1}$$

where $R(E)$ is response function of HF RadMon detector (could be seen in Fig. 4.18), $d\Phi_{FLUKA}(E)/dE$ is differential energy spectrum of neutrons in given region from FLUKA and $d\Phi_{AmBe}(E)/dE$ is differential energy spectrum of neutrons from AmBe source. Before performing the integral both distributions have to be normalised to same number neutrons on range of integration. AmBe source emits neutrons from 0.414 eV to 15 MeV so

$$\int_{0.414\ eV}^{15\ MeV} \frac{d\Phi_{FLUKA}(E)}{dE}dE = \int_{0.414\ eV}^{15\ MeV} \frac{d\Phi_{AmBe}(E)}{dE}dE \tag{4.2}$$

must be accomplished before performing the integral of distribution folded with response function at the same range. Neutron spectra in all regions used with 13 TeV simulation could be seen on Fig. 4.16 and for 5 TeV simulation in Fig. 4.17.

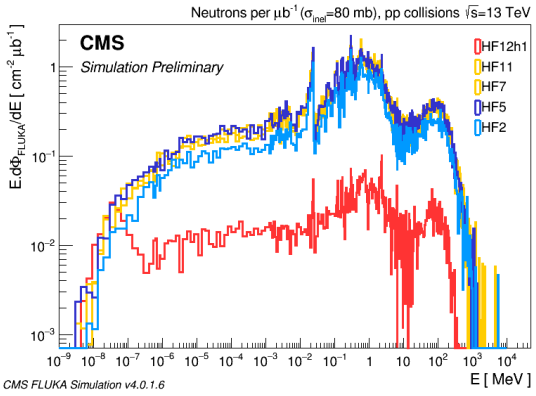

Figure 4.16: Neutron energy spectra in scoring regions for 13 TeV simulation.

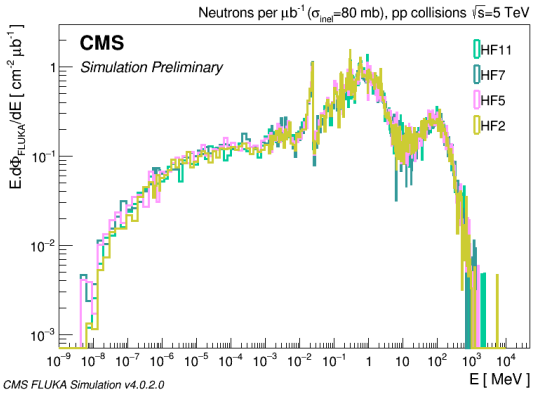

Figure 4.17: Neutron energy spectra in scoring regions for 5 TeV simulation.

After all previous steps could be k_{cal} computed for each centre-of-mass energy and location. Response function $R(E)$, normalised spectrum and folded function for one location could be seen in Fig. 4.18. When k_{cal} for all relevant locations is known it allows one to estimate expected fluence of neutrons in all HF RadMon locations. Measured data and expected values from simulations could be compared. Because neutrons were simulated symmetrically on both sides, it cannot be distinguished between $\pm z$ in simulation. Because of this fact simulation results were compared with date from both ends of the CMS detector.

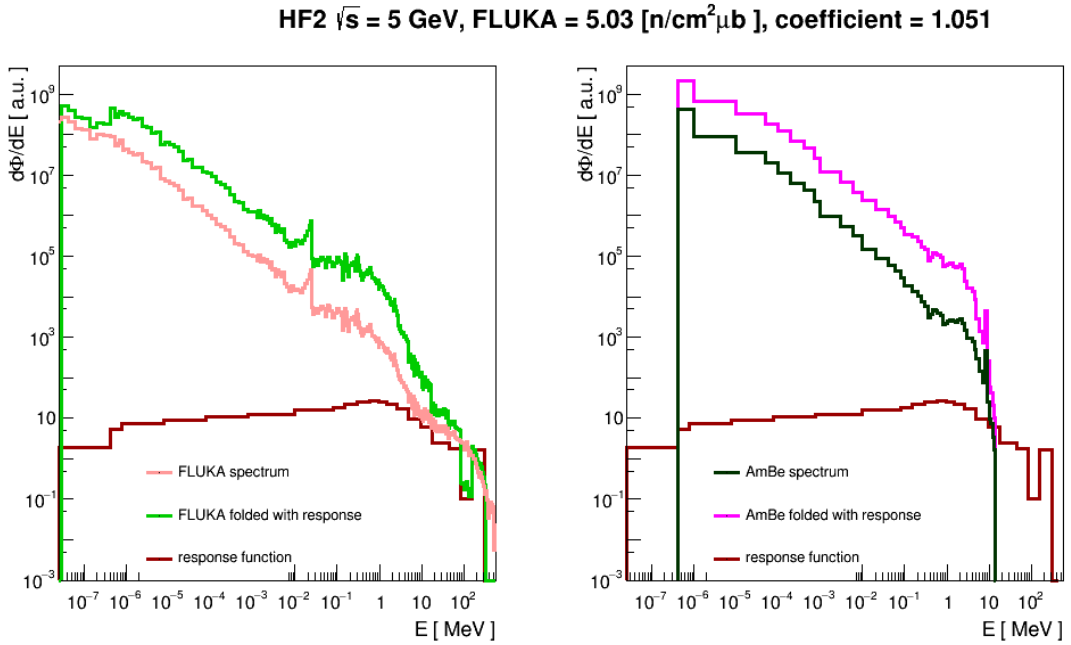

Figure 4.18: Estimation of k_{cal} for HF2 location (relating to PNIT and MNIT monitors from 4.2). The USRTRACK output from FLUKA folded with response function (left). Spectra of AmBe spectrum recalculated to differential spectra and normalised to FLUKA output (right) folded with response function.

Calibration coefficients for spectra scoring regions for both centre-of-mass energies compared to data measured in 2017 and 2018 are in Tab. 4.3, Tab. 4.4 and Tab. 4.5. It could be seen that values expected from simulations are underestimated. From Tab. 4.2 is visible that lower rates were always measured in positive z side, so ratio of data to simulations are closer to one for this side.

Region	Φ_{FLUKA} $[cm^{-2}\mu b^{-1}]$	k_{cal}	$\Phi_{exp}/\ data^{5TeV}_{2017}$(-Z)	$\Phi_{exp}/\ data^{5TeV}_{2017}$(+Z)
HF2	5.03	1.051	2.858	2.905
HF5	5.12	1.055	2.38	2.232
HF7	5.04	1.034	2.256	x
HF11	5.004	1.031	x	2.646

Table 4.3: Result of HF RadMon benchmark study. The number of neutrons in scoring region for energy range of response function Φ_{FLUKA} is multiplied to get calibration coefficient k_{cal} to get Φ_{exp}. Then a ration to measured data in 2017 with centre-of-mass energy equal to 5 TeV for both $\pm z$ sides.

Region	Φ_{FLUKA} $[cm^{-2}\mu b^{-1}]$	k_{cal}	$\Phi_{exp}/\ data^{13TeV}_{2017}$(-Z)	$\Phi_{exp}/\ data^{13TeV}_{2017}$(+Z)
HF2	7.211	1.054	2.229	2.100
HF5	7.587	1.053	1.880	1.775
HF7	7.494	1.061	1.836	x
HF11	7.184	1.056	x	2.078
HF12h1	0.423	1.022	1.729	1.601

Table 4.4: Result of HF RadMon benchmark study. The number of neutrons in scoring region for energy range of response function Φ_{FLUKA} is multiplied to get calibration coefficient k_{cal} to get Φ_{exp}. Then a ration to measured data in 2017 with centre-of-mass energy equal to 13 TeV for both $\pm z$ sides.

Region	Φ_{FLUKA} $[cm^{-2}\mu b^{-1}]$	k_{cal}	$\Phi_{exp}/\ data^{13TeV}_{2018}$(-Z)	$\Phi_{exp}/\ data^{13TeV}_{2018}$(+Z)
HF2	7.211	1.054	2.436	2.360
HF5	7.587	1.053	1.939	1.925
HF7	7.494	1.061	1.893	x
HF11	7.184	1.056	2.393	2.334
HF12h1	0.423	1.022	1.601	x

Table 4.5: Result of HF RadMon benchmark study. The number of neutrons in scoring region for energy range of response function Φ_{FLUKA} is multiplied to get calibration coefficient k_{cal} to get Φ_{exp}. Then a ratio to measured data in 2018 with centre-of-mass energy equal to 13 TeV for both $\pm z$ sides.

Averaging over all data to simulation ratios for 5 TeV simulation and considering standard deviation as error gives 2.546 ± 0.299 and 2.007 ± 0.278 for 13 TeV. There is one more way how to benchmark simulations of radiation field in CMS cavern. As could be seen from Fig. 4.12 and Fig. 4.13 material around HF might be taken as a shielding and efficiency of this shield could be inferred from data and simulations separately and then be compared. Only in 13 TeV data both internal and external measured values were provided. In 2018 data are both monitors on same side of CMS so, they might be compared with simulation. Ratios were computed in Tab. 4.6. Ratio of simulation to data is approximately 1.25, which shows good agreement between them. For simplicity a normalization based on an inelastic cross section of 80 mb based on 14 TeV center-of-mass energy collisions has been applied for all simulations. It is known to be slightly lower for 13 TeV and more so for 5 TeV center-of-mass energy collisions and estimates would scale linearly meaning the ratios would be slightly closer to one. These normalization adjustments will be implemented for a follow up analysis.

	internal / external
$data^{13TeV}_{2018}$(+Z) (PFIT/PFXT)	13.52
simulations (HF11/HF12h1)	16.98

Table 4.6: Efficiency of shielding by material around HF calorimeter seen in data and expected from simulations.

Summary

The monitoring and predictions of radiation environment in the CMS cavern are necessary for various reasons. Safety to personnel has to be ensured for all accesses to the cavern so level of residual radiation has to be known before anybody is allowed to enter the experimental hall. Activation from the prompt background radiation during collisions should be limited. Moreover, ionizing particles can harm detector sensitive elements, so investigation of radiation field in cavern helps with choosing of technologies for future operation. Background radiations can also generate false triggers in the CMS detectors. The CMS BRIL RadSim group participates in simulations of background radiation in cavern, contributes to design of shielding and detector upgrades, and assists with the development of radiation monitoring infrastructure. Simulations are benchmarked where possible to verify the use of the set up for future estimates.

This thesis describes CERN experimental facility and CMS experiment, the propagation of radiation through matter, and the use of FLUKA transport code. A summary of the radiation monitors operated and used by BRIL is provided. Several key tasks for the BRIL RadSim group were performed including simulations for predicting the features and composition of radiation field at various CMS cavern locations, a comparison of Run 3 and Run 4 estimates, and a benchmark of Run 2 data. For estimates of the radiation field in locations of radiation monitors absorbed dose, fluence of 1 MeV neurons in Si equivalent and fluence of high energy hadrons were considered. This enabled the estimation dynamic range requirements of monitors proposed for the Phase 2 era, values are listed in Tab. 4.1. Energy spectra all around the cavern was simulated for relevant particles species. To investigate precision of simulations a benchmark study was performed with Run 2 geometry model and data from HF RadMon monitors in 2017 and 2018. Calibration coefficient was found for all locations, where data was measured. The ratio of simulation to data measured with HF RadMons in 2017 and 2018 for 13 TeV was found to be 2.007 ± 0.278 and 2.546 ± 0.299 for 13 TeV centre-of-mass energy.

Bibliography

1. BENEDETTI, S. *The 2017 Xe run at CERN Linac3: Measurements and beam dynamics simulations*. Available from DOI: 10.1063/1.5066086.
2. HILL, C. *Performance of the CERN Linac 2 with a high intensity proton RFQ*.
3. COLLABORATION, CERN. *CLEAR*. Available also from: https://clear.cern/content/welcome-clear.
4. REGENSTREIF, E. *The CERN Proton Synchrotron*. Available from DOI: 10.5170/CERN-1962-003.
5. AMBATS, I. *The MINOS Detectors Technical Design Report*.
6. PLASS, G. *Design study of a facility for experiments with low energy antiprotons (LEAR)*. Available also from: https://cds.cern.ch/record/124681.
7. BAIRD, S. A. *Design study of the antiproton decelerator: AD*. Available also from: https://cds.cern.ch/record/317704.
8. CALDWELL, A. *AWAKE Design Report: A Proton-Driven Plasma Wakefield Acceleration Experiment at CERN*. Available also from: https://cds.cern.ch/record/1537318.
9. COLLABORATION, CERN. *The CERN accelerator complex*. Available also from: https://cds.cern.ch/record/2684277/files/.
10. BENEDIKT, M. *LHC Design Report*. Available from DOI: 10.5170/CERN-2004-003-V-3.
11. AUCHMANN, B. *Testing Beam-Induced Quench Levels of LHC Superconducting Magnets*. Available from DOI: 10.1103/PhysRevSTAB.18.061002.
12. BONAUDI, F. *Magnets in particle physics*. Available also from: https://cds.cern.ch/record/245397/files/p1.pdf.
13. COLLABORATION, CERN. *Magnetic multipoles*. Available also from: https://www.lhc-closer.es/taking_a_closer_look_at_lhc/0.magnetic_multipoles.
14. CONTARDO, D. *Technical Proposal for the Phase-II Upgrade of the CMS Detector*. Available also from: https://cds.cern.ch/record/2020886.
15. AZZI, P. *Report from Working Group 1: Standard Model Physics at the HL-LHC and HE-LHC*. Available from DOI: 10.23731/CYRM-2019-007.1.
16. COLLABORATION, CERN. *LHC/ HL-LHC Plan*. Available also from: https://hilumilhc.web.cern.ch/content/hl-lhc-project.
17. COLLABORATION, CMS. *Observation of a new boson at a mass of 125 GeV with the CMS experiment at the LHC*. Available from DOI: 10.1016/j.physletb.2012.08.021.

18. COLLABORATION, ATLAS. *Observation of a new particle in the search for the Standard Model Higgs boson with the ATLAS detector at the LHC*. Available from DOI: 10.1016/j.physletb.2012.08.020.

19. SAKUMA, T. *Detector and Event Visualization with SketchUp at the CMS Experiment*. Available from DOI: 10.1088/1742-6596/513/2/022032.

20. KARIMÄKI, V. *The CMS tracker system project: Technical Design Report*. CERN. Available also from: https://cds.cern.ch/record/368412.

21. *The CMS tracker: addendum to the Technical Design Report*. CERN. Available also from: https://cds.cern.ch/record/490194.

22. COLLABORATION, The CMS. *The CMS experiment at the CERN LHC*. Available from DOI: 10.1088/1748-0221/3/08/s08004.

23. *The CMS electromagnetic calorimeter project: Technical Design Report*. Available also from: https://cds.cern.ch/record/349375.

24. BLOCH, P. *Changes to CMS ECAL electronics: addendum to the Technical Design Report*. Available also from: https://cds.cern.ch/record/581342.

25. *The CMS hadron calorimeter project: Technical Design Report*. Available also from: https://cds.cern.ch/record/357153.

26. MANS, J. *CMS Technical Design Report for the Phase 1 Upgrade of the Hadron Calorimeter*. Available also from: https://cds.cern.ch/record/1481837.

27. *The CMS magnet project: Technical Design Report*. Available also from: https://cds.cern.ch/record/331056.

28. COLLABORATION, CMS. *Precise mapping of the magnetic field in the CMS barrel yoke using cosmic rays*. Available also from: http://dx.doi.org/10.1088/1748-0221/5/03/T03021.

29. LAYTER, J. G. *The CMS muon project: Technical Design Report*. Available also from: https://cds.cern.ch/record/343814.

30. *The Phase-2 Upgrade of the CMS Muon Detectors*. Available also from: https://cds.cern.ch/record/2283189.

31. PUGLIESE, G. *CMS RPC muon detector performance with 2010-2012 LHC data*. Available from DOI: 10.1088/1748-0221/9/12/C12016.

32. SHOPOVA, M. *Performance of Resistive Plate Chambers installed during the first long shutdown of the CMS experiment*. Available also from: https://arxiv.org/abs/1605.06798.

33. COLALEO, A. *CMS Technical Design Report for the Muon Endcap GEM Upgrade*. Available also from: https://cds.cern.ch/record/2021453.

34. *CMS L1 Calorimeter Trigger performance in 2016 data*. Available also from: https://cds.cern.ch/record/2202966.

35. *The Phase-2 Upgrade of the CMS L1 Trigger Interim Technical Design Report*. Available also from: https://cds.cern.ch/record/2283192.

36. GUTHOFF, M. *Radiation Damage to the diamond-based Beam Condition Monitor of the CMS Detector at the LHC*. Available also from: https://cds.cern.ch/record/1977429.

37. WANCZYK, J. *Measurements and estimates of the radiation levels in the CMS Experimental Cavern using Medipix and RAMSES monitors, and the FLUKA Monte Carlo code*. Available also from: https://cds.cern.ch/record/2701798.

38. LEO, W. R. *Techniques for Nuclear and Particle Physics Experiments: A How to Approach*. ISBN 978-3-540-57280-0.

39. BARKAS, W. H. *Mass-ratio method applied to the measurement of L-Meson masses and the energy balance in pion decay*. Available also from: https://cds.cern.ch/record/401564.

40. ZYLA, P.A. *Review of Particle Physics*. Available from DOI: 10.1093/ptep/ptaa104.

41. HUHTINEN, M. *The radiation environment at the CMS experiment at the LHC*. Available also from: https://cds.cern.ch/record/308251.

42. ICRP. *Conversion Coefficients for Radiological Protection Quantities for External Radiation Exposures*. Available from DOI: 10.1016/j.icrp.2011.10.001.

43. FRETWURST, E. *Radiation Damage in Silicon Detectors Caused by Hadronic and Electromagnetic Irradiation*.

44. B., Giuseppe. *Overview of the FLUKA code*. Available from DOI: https://doi.org/10.1016/j.anucene.2014.11.007.

45. VLACHOUDIS, V. *FLAIR: A POWERFUL BUT USER FRIENDLY GRAPHICAL INTERFACE FOR FLUKA*.

46. MATERIAL, FLUKA course. *FLUKA Combinatorial Geometry in 15th FLUKA Course 2014 in Greeece*. Available also from: http://www.fluka.org/fluka.php.

47. WIJNANDS, T. *An on line radiation monitoring system for the LHC machine and experimental caverns*. Available from DOI: 10.5170/CERN-2007-001.113.

48. MARTINELLA, C. *High Energy Hadrons Fluence Measurements in the LHC during 2015, 2016 and 2017 Proton Physics Operations*. Available also from: http://cds.cern.ch/record/2652458.

49. DIMITROV, L. *Radiation monitoring of the GEM muon detectors at CMS*. Available from DOI: 10.1134/S1547477116050174.

50. KRAMER, D. *LHC RadMon SRAM Detectors Used at Different Voltages to Determine the Thermal Neutron to High Energy Hadron Fluence Ratio*. Available from DOI: 10.1109/TNS.2011.2105891.

51. VINCKE, H. *Simulation and measurements of the response of an air ionisation chamber exposed to a mixed high-energy radiation field*. Available from DOI: 10.1093/rpd/nci088.

52. *Private discussion with Arkady Lokhovitskiy*.

53. BONNER, T.W. *A new type of neutron spectrometer*. Available from DOI: https://doi.org/10.1016/0029-554X(60)90043-4.

54. K., Sei-ichi. *Neutron Cross Sections of Li-6*. Available from DOI: 10.1080/18811248.1978.9733203.

55. GARUTTI, E.; MUSIENKO, Yu. *Radiation damage of SiPMs*. Available from DOI: 10.1016/j.nima.2018.10.191.

56. COLLABORATION, The CMS. *The Phase-2 Upgrade of the CMS Beam Radiation, Instrumentation, and Luminosity Detectors: Conceptual Design*. Available also from: https://cds.cern.ch/record/2706512.

57. *Private discussion with Igor Kurochkin.*

58. *Private discussion with Andrei Gribushin.*

Appendix

A Proposed locations of radiation monitors

Monitor ID	x [cm]	y [cm]	z [cm]
PMIL5501	1060 ± 50	-570 ± 50	2200 ± 50
PMIL5502	100 ± 50	-1020 ± 50	-300 ± 70
PMIL5511	990 ± 50	100 ± 50	2450 ± 50
PMIL5512	-930 ± 50	70 ± 50	-2450 ± 50
PMIL5513	980 ± 50	60 ± 50	-2450 ± 50
PMIL5514	-160 ± 50	250 ± 50	1450 ±50
PMIL5515	-170 ± 50	259 ± 50	-1450 ± 50
PMIL5521	80 ± 30	460 ± 50	2650 ± 50
PMIL5522	-50 ± 30	510 ± 50	-2650 ± 50
PMIL5531	1080 ± 50	440 ± 50	400 ± 100
PMIL5541	-160 ± 50	250 ± 50	950 ±50
PMIL5542	-170 ± 50	259 ± 50	-950 ± 50

Table 7: Proposed locations of REMUS detectors.

Monitor ID	x [cm]	y [cm]	z [cm]
PFXT1	-180 ± 100	180 ± 100	1220 ± 50
PFXT2	-180 ± 100	180 ± 100	920 ± 100
PFIT	-92 ± 50	92 ± 50	1390 ± 50
PNIB	92 ± 50	-92 ± 50	1390 ± 50
PNXB1	180 ± 100	-180 ± 100	1220 ± 50
PNXB2	180 ± 100	-180 ± 100	920 ± 100
MFXT1	-180 ± 100	180 ± 100	-1220 ± 50
MFXT2	-180 ± 100	180 ± 100	-920 ± 100
MFIT	-92 ± 50	92 ± 50	-1390 ± 50
MNIB	92 ± 50	-92 ± 50	-1390 ± 50
MNXB1	180 ± 100	-180 ± 100	-1220 ± 50
MNXB2	180 ± 100	-180 ± 100	-920 ± 100

Table 8: Proposed locations of GFPC light.

Monitor ID	x [cm]	y [cm]	z [cm]
5RE02	1321	-692	1126
5LE02	979	80	54
5RE03	1316	302	1039
5LE03	1319	-728	-930
5RE04	65	500	2649
5LE04	1312	339	-912
5RE05	-1309	354	861
5LE05	0	400	-2480
5RE06	-1000	0	0
5LE06	800	400	-700
5RE07	-1196	-705	567
5LE07	-1313	353	-1021
5LE08	-1178	-734	-1043
5RE09	0	-400	2200
5LE09	0	-400	-2200
5RE10	0	-1050	500
5LE10	0	-450	-2350
5LE11	1290	-700	-2000± 100
5RE11	1290	-700	2000± 100
5LE12	1290	400	-2000± 100
5RE12	1290	400	2000± 100
5LE13	-1290	400	-2000± 100
5RE13	-1290	400	2000± 100
5LE14	-1290	-700	-2000± 100
5RE14	-1290	-700	2000± 100
5RE15	-200	250	1450
5LE15	-200	250	-1450
5RE21	550± 50	650± 100	800 ± 50
5LE21	550± 50	650± 100	-800 ± 50
5LE22	-550± 50	650± 100	800 ± 50
5RE22	-550± 50	650± 100	-800 ± 50
5LE23	550± 50	650± 100	1050 ± 50
5RE23	-550± 50	650± 100	-1050 ± 50
5LE24	550± 50	650± 100	1050 ± 50
5RE24	-550± 50	650± 100	-1050 ± 50
5LE25	-1290± 100	750± 100	600 ± 50
5RE25	-1290± 100	-750± 100	-600 ± 50
5RE26	-200± 100	750± 100	600 ± 50
5LE26	-200± 100	-750 ± 100	-600± 50

Table 9: Proposed locations of LHC RadMons.

Monitor ID	x [cm]	y [cm]	z [cm]
NMX3IPNEAR	1250 ± 100	0 ± 70	0 ± 150
NMX3IPFAR	-1250 ± 100	0 ± 70	0 ± 150
NMIPYB0TOP	0 ± 70	700 ± 150	0 ± 70
NMIPFLOOR	0 ± 150	-950 ± 100	0 ± 200
NMYE3PFAR	-400 ± 100	500 ± 100	700 ± 100
NMYE3PNEAR	400 ± 100	500 ± 100	700 ± 100
NMYE3NFAR	-400 ± 100	500 ± 100	-700 ± 100
NMYE3NNEAR	400 ± 100	500 ± 100	-700 ± 100
NMBHP	50 ± 120	460 ± 100	2650 ± 50
NMBHN	-50 ± 120	460 ± 100	-2650 ± 50
NMBHRSP	50 ± 120	400 ± 100	2250 ± 150
NMBHRSN	-50 ± 120	400 ± 100	-2250 ± 150
NMX1PFAR	-1250 ± 100	-700 ± 100	2000 ± 200
NMX2PFAR	-1250 ± 100	-400 ± 100	1000 ± 200
NMX4PFAR	-1250 ± 100	400 ± 100	1400 ± 200
NMX1NFAR	-1250 ± 100	-700 ± 100	-2000 ± 200
NMX2NFAR	-1250 ± 100	-400 ± 100	-1000 ± 200
NMX4NFAR	-1250 ± 100	400 ± 100	-1400 ± 200
NMX1PNEAR	1250 ± 100	-700 ± 100	2000 ± 200
NMX2PNEAR	1250 ± 100	-400 ± 100	1000 ± 200
NMX4PNEAR	1250 ± 100	400 ± 100	1400 ± 200
NMX1NNEAR	1250 ± 100	-700 ± 100	-2000 ± 200
NMX2NNEAR	1250 ± 100	-400 ± 100	-1000 ± 200
NMX4NNEAR	1250 ± 100	400 ± 100	-1400 ± 200

Table 10: Proposed locations of GFPC full monitors.

Monitor ID	x [cm]	y [cm]	z [cm]
NMME21P1	-110 ± 30	110 ± 30	825 ± 30
NMME21P2	-400 ± 30	250 ± 30	825 ± 30
NMME21P3	110 ± 30	-110 ± 30	825 ± 30
NMME21P4	400 ± 30	-250 ± 30	825 ± 30
NMME21N1	-110 ± 30	110 ± 30	-825 ± 30
NMME21N2	-400 ± 30	250 ± 30	-825 ± 30
NMME21N3	110 ± 30	-110 ± 30	-825 ± 30
NMME21N4	400 ± 30	-250 ± 30	-825 ± 30
NMME21N4	50 ± 120	400 ± 100	-2250 ± 150
NMME21N4	50 ± 120	400 ± 100	2250 ± 150

Table 11: Proposed locations of SiMP FN detectors.

Monitor ID	x [cm]	y [cm]	z [cm]
NMSP1	0 ± 250	400 ± 100	-1170 ± 150
NMSP2	0 ± 150	180 ± 100	1170 ± 150
NMSP3	850 ± 100	400 ± 150	1000 ± 200
NMSP4	850 ± 100	-600 ± 150	1000 ± 200

Table 12: Proposed locations of Bonnner sphere spectrometers with SiMP.

B Spectra scoring region locations

Scoring region	x [cm]	y [cm]	z [cm]
HF11	0±50	300±50	1150±50
BALC1	1200±50	0±50	150±50
BALC2	1200±50	0±50	950±50
BALC3	1200±50	0±50	1500±50
BALC4	1200±50	0±50	1800±50
BALC5	1200±50	0±50	2550±50
BL1	0±50	-1150±50	500±50
BL2	0±50	-450±50	2150±50
BH1	0±50	400±50	2150±50
BH2	0±50	400±50	2300±50
BH3	0±50	400±50	2550±50
BL3	0±50	800±50	100±50
HF14	-150±50	260±50	1400±50
ME2h4	150±50	-150±50	812±10
ME2h11	-150±50	150±50	812±10
HF9h4	200±50	-200±50	952±10
HF9h11	-200±50	200±50	952±10
HF12h4	280±50	-120±50	1220±50
HF12h1	-170±50	260±50	1220±50
YE1h2	-300±50	500±50	812±10
YE1h11	300±50	500±50	812±10
YE3h2	-300±50	500±50	1045±15
YE3h11	300±50	500±50	1045±15
WH1	-250±50	750±50	600±50
WH2	-1150±50	650±50	600±50

Table 13: Scoring regions for energy spectra in this regions, all regions are made out of the air. Where it was enough space regions have volume of 1 m^3

.

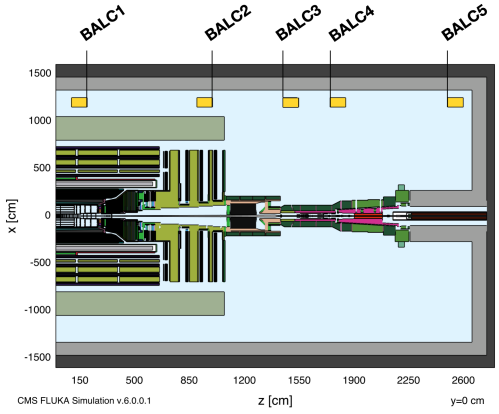

Figure 19: Location of scoring regions, top view.

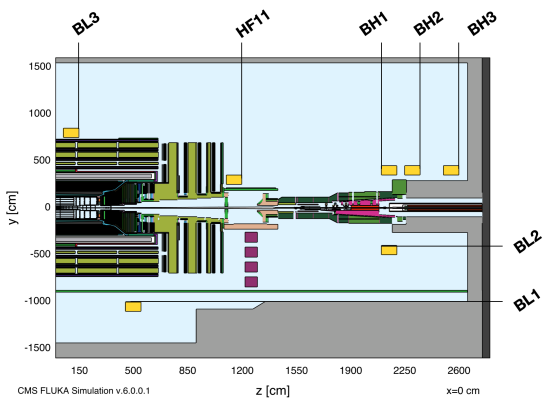

Figure 20: Location of scoring regions, side view.

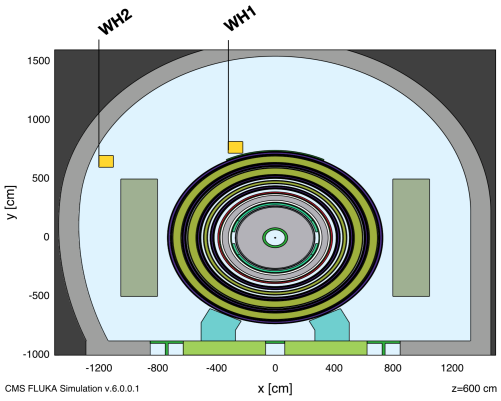

Figure 21: Visualization of scoring regions WH1 and WH2.

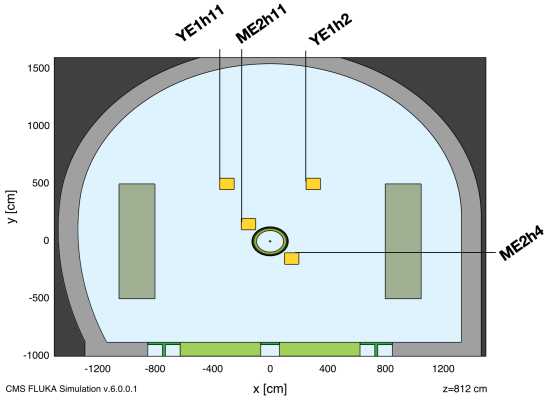

Figure 22: Visualization of scoring regions ME2h4, ME2h11, YE1h2 and YE1h11.

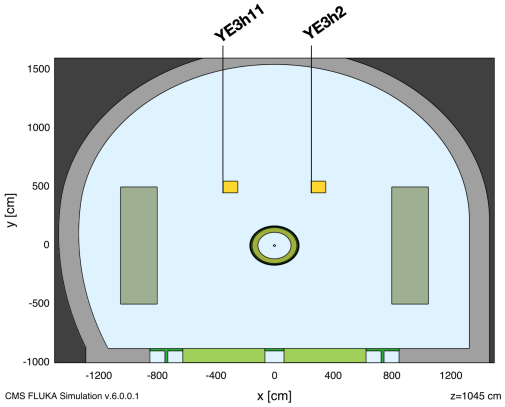

Figure 23: Visualization of scoring regions YE3h2 and YE3h11.

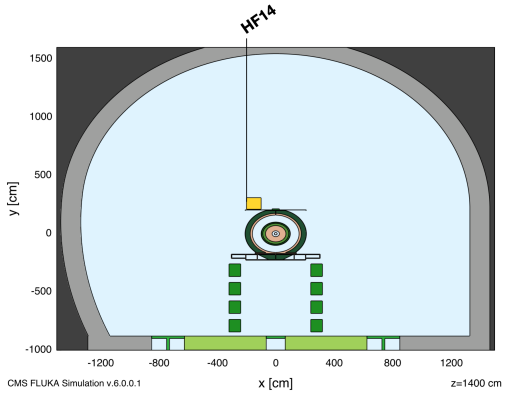

Figure 24: Visualization of scoring region HF14.

C Simulated quantities in proposed detector locations

CMS geometry version 5.0.0.3

ID	Level	Side	Since	D [Gy]	$\Phi_{neq}^{1\ MeV}$[cm^{-2}]	Φ_{HEH}[cm^{-2}]
PMIL5501	X1	NEAR	Run2	27.0±2.5	(4.985±0.020)e11	(8.28±0.08)e10
PMIL5502	X0	NEAR	Run2	0.03±0.02	(1.12±0.08)e9	(9.5±2.0)e7
PMIL5511	X3	NEAR	Run2	14.0±0.8	(4.765±0.025)e11	(1.120±0.008)e11
PMIL5512	X3	FAR	Run2	15.7±0.9	(4.915±0.025)e11	(1.167±0.010)e11
PMIL5513	X3	FAR	Run2	15.7±0.9	(4.915±0.025)e11	(1.167±0.010)e11
PMIL5514	HFTOP	FAR	Run2	80±3	(3.134±0.007)e12	(9.32±0.03)e11
PMIL5515	HFTOP	FAR	Run2	66±2	(2.839±0.006)e12	(8.49±0.03)e11
PMIL5521	BH	BL	Run2	19.0±0.7	(4.605±0.027)e11	(1.410±0.015)e11
PMIL5522	BH	BL	Run2	18.6±0.8	(4.705±0.025)e11	(1.40±0.02)e11
PMIL5531	X4	NEAR	Run2	5.5±0.9	(1.725±0.01)e11	(1.19±0.03)e10
PMIL5541	HFTOP	FAR	Run3	14.8±0.6	(7.76±0.04)e11	(1.032±0.010)e11
PMIL5542	HFTOP	FAR	Run3	14.8±0.6	(7.76±0.04)e11	(1.032±0.010)e11

CMS geometry version 6.0.0.1

PMIL5501	X1	NEAR	Run2	19.8±1.2	(9.11±0.03)e11	(2.43±0.02)e11
PMIL5502	X0	NEAR	Run2	0.045±0.020	(2.10±0.15)e9	(2.2±0.5)e8
PMIL5511	X3	NEAR	Run2	17.2±0.8	(5.96±0.03)e11	(1.32±0.01)e11
PMIL5512	X3	FAR	Run2	17.6±1.1	(6.12±0.02)e11	(1.342±0.110)e11
PMIL5513	X3	NEAR	Run2	17.6±1.1	(6.12±0.02)e11	(1.342±0.110)e11
PMIL5514	HFTOP	FAR	Run2	84±2.7	(3.324±0.009)e12	(9.89±0.03)e11
PMIL5515	HFTOP	FAR	Run2	81±2.6	(3.027±0.005)e12	(9.01±0.02)e11
PMIL5521	BH	BL	Run2	20±1.1	(15.7±0.02)e11	(1.412±0.003)e11
PMIL5522	BH	BL	Run2	21±1.1	(5.345±0.032)e11	(1.407±0.013)e11
PMIL5531	X4	NEAR	Run2	4±0.3	(1.695±0.009)e11	(1.06±0.03)e10
PMIL5541	HFTOP	FAR	Run3	15.4±0.7	(7.33±0.04)e11	(9.81±0.09)e10
PMIL5542	HFTOP	FAR	Run3	15.4±0.7	(7.33±0.04)e11	(9.81±0.09)e10

Table 14: Extracted values of absorbed dose D, 1 MeV neutron equivalent fluence in Si $\Phi_{neq}^{1\ MeV}$ and fluence of hadrons with energy grater than 20 MeV Φ_{HEH} in REMUS detector provided locations for Run 3 (5.0.0.3) and Run 4 (6.0.0.1) geometry versions. All values are normalised per 4000 fb^{-1}.

Monitor ID	Level	Side	Since	D [Gy]	$\Phi_{neq}^{1\ MeV}[\mathrm{cm}^{-2}]$	$\Phi_{HEH}[\mathrm{cm}^{-2}]$
5RE02	X1	NEAR	Run2	11.1±0.9	(4.47±0.02)e11	(8.54±0.08)e10
5LE02	X3	NEAR	Run2	2.26±0.07	(1.172±0.009)e11	(3.35±0.15)e9
5RE03	X4	NEAR	Run2	12.7±1.3	(4.58±0.03)e11	(8.66±0.06)e10
5LE03	X1	NEAR	Run2	9.0±0.6	(3.79±0.02)e11	(7.00±0.07)e10
5RE04	X4	BL	Run2	26.7±1.3	(6.75±0.03)e11	(2.085±0.017)e11
5LE04	X4	NEAR	Run2	8.7±0.8	(3.505±0.020)e11	(6.12±0.06)e10
5RE05	X4	FAR	Run2	7.7±0.5	(3.34±0.02)e11	(5.72±0.06)e10
5LE05	X4	BL	Run2	3.6±0.4	(1.175±0.015)e11	(1.69±0.04)e10
5RE06	X3	FAR	Run2	2.18±0.06	(1.168±0.008)e11	(3.45±0.15)e9
5LE06	X4	FAR	Run2	4.8±0.03	(1.73±0.02)e11	(6.25±0.21)e9
5RE07	X1	FAR	Run2	6.5±0.5	(2.42±0.02)e11	(3.38±0.04)e10
5LE07	X4	FAR	Run2	8.9±0.6	(4.04±0.02)e11	(7.31±0.07)e10
5LE08	X1	FAR	Run2	10.1±0.6	(4.58±0.02)e11	(8.56±0.08)e10
5RE09	X2	BL	Run2	151±4	(4.108±0.07)e12	(1.491±0.004)e12
5LE09	X2	BL	Run2	151±4	(4.108±0.07)e12	(1.491±0.004)e12
5RE10	X0	BL	Run2	0.055±0.010	(5.00±0.15)e9	(6.3±0.5)e8
5LE10	X2	BL	Run2	51±3	(1.428±0.004)e12	(4.33±0.02)e11
5LE11	X1	NEAR	Run3	6.20±0.15	(2.29±0.03)e11	(7.05±0.10)e10
5RE11	X1	NEAR	Run3	6.20±0.15	(2.29±0.03)e11	(7.05±0.10)e10
5LE12	X4	NEAR	Run3	5.9±0.1	(2.22±0.03)e11	(6.85±0.10)e10
5RE12	X4	NEAR	Run3	5.9±0.1	(2.22±0.03)e11	(6.85±0.10)e10
5LE13	X4	FAR	Run3	5.9±0.1	(2.22±0.03)e11	(6.85±0.10)e10
5RE13	X4	FAR	Run3	5.9±0.1	(2.22±0.03)e11	(6.85±0.10)e10
5LE14	X1	FAR	Run3	5.9±0.1	(2.22±0.03)e11	(6.85±0.10)e10
5RE14	X1	FAR	Run3	5.9±0.1	(2.22±0.03)e11	(6.85±0.10)e10
5RE15	HFTOP	FAR	Run3	58±2	(2.540±0.005)e12	(7.455±0.020)e11
5LE15	HFTOP	FAR	Run3	58±2	(2.540±0.005)e12	(7.455±0.020)e11

Table 15: Extracted values of absorbed dose D, 1 MeV neutron equivalent fluence in Si $\Phi_{neq}^{1\ MeV}$ and fluence of hadrons with energy grater than 20 MeV Φ_{HEH} in LHC Radmon detector provided locations for Run 4 (6.0.0.1) geometry version. All values are normalised per 4000 fb^{-1}.

Monitor ID	Level	Side	Since	D [Gy]	$\Phi_{neq}^{1\ MeV}$[cm^{-2}]	Φ_{HEH}[cm^{-2}]
5RE02	X1	NEAR	Run2	11.1±1.1	(4.867±0.022)e11	(9.36±0.08)e10
5LE02	X3	NEAR	Run2	2.85±0.19	(1.245±0.010)e11	(4.12±0.18)e9
5RE03	X4	NEAR	Run2	13.7±1.0	(5.065±0.023)e11	(9.51±0.08)e10
5LE03	X1	NEAR	Run2	10.2±0.7	(4.105±0.021)e11	(7.27±0.08)e10
5RE04	X4	BL	Run2	21±1.2	(5.35±0.02)e11	(1.407±0.013)e11
5LE04	X4	NEAR	Run2	10.2±0.9	(4.15±0.02)e11	(6.93±0.08)e10
5RE05	X4	FAR	Run2	8.8±0.6	(3.87±0.02)e11	(6.42±0.06)±e10
5LE05	X4	BL	Run2	23.9±1.4	(5.94±0.02)e11	(1.705±0.009)e11
5RE06	X3	FAR	Run2	3.04±0.18	(1.237±0.012)e11	(3.95±0.20)e9
5LE06	X4	FAR	Run2	4.6±0.3	(1.83±0.1)e11	(6.4±0.2)e9
5RE07	X1	FAR	Run2	4.7±0.02	(2.402±0.015)e11	(3.4±0.05)e10
5LE07	X4	FAR	Run2	12.6±1.2	(4.77±0.02)e11	(8.61±0.07)e10
5LE08	X1	FAR	Run2	10.6±0.06	(4.65±0.02)e11	(8.88±0.08)e10
5RE09	X2	BL	Run2	9.6±0.6	(3.281±0.024)e11	(5.69±0.07)e10
5LE09	X2	BL	Run2	9.6±0.6	(3.281±0.024)e11	(5.69±0.07)e10
5RE10	X0	BL	Run2	0.09±0.03	(5.05±0.21)e9	(6.20±0.75)e8
5LE10	X2	BL	Run2	39.7±0.9	(1.145±0.04)e12	(3.155±0.21)e11
5LE11	X1	NEAR	Run3	18.2±0.09	(6.49±0.03)e11	(1.497±0.008)e11
5RE11	X1	NEAR	Run3	18.2±0.09	(6.49±0.03)e11	(1.497±0.008)e11
5LE12	X4	NEAR	Run3	5.67±0.11	(2.11±0.03)e11	(6.55±0.11)e10
5RE12	X4	NEAR	Run3	5.67±0.11	(2.11±0.03)e11	(6.55±0.11)e10
5LE13	X4	FAR	Run3	5.67±0.11	(2.11±0.03)e11	(6.55±0.11)e10
5RE13	X4	FAR	Run3	5.67±0.11	(2.11±0.03)e11	(6.55±0.11)e10
5LE14	X1	FAR	Run3	5.67±0.11	(2.11±0.03)e11	(6.55±0.11)e10
5RE14	X1	FAR	Run3	5.67±0.11	(2.11±0.03)e11	(6.55±0.11)e10
5RE15	HFTOP	FAR	Run3	80.9±2.9	(3.027±0.006)e12	(9.01±0.03)e11
5LE15	HFTOP	FAR	Run3	80.9±2.9	(3.027±0.006)e12	(9.01±0.03)e11

Table 16: Extracted values of absorbed dose D, 1 MeV neutron equivalent fluence in Si $\Phi_{neq}^{1\ MeV}$ and fluence of hadrons with energy grater than 20 MeV Φ_{HEH} in LHC Radmon detector provided locations for Run 3 (5.0.0.3) geometry version. All values are normalised per 4000 fb^{-1}.

CMS geometry version 5.0.0.3

ID	Level	Side	Since	D [Gy]	$\Phi_{neq}^{1\ MeV}$[cm^{-2}]	Φ_{HEH}[cm^{-2}]
5RE21	CSC	FAR	Phase II	5.8±0.9	(2.29±0.3)e11	(6.1±0.8)e9
5LE21	CSC	FAR	Phase II	5.8±0.9	(2.29±0.3)e11	(6.1±0.8)e9
5LE22	CSC	NEAR	Phase II	5.8±0.9	(2.29±0.3)e11	(6.1±0.8)e9
5RE22	CSC	NEAR	Phase II	5.8±0.9	(2.29±0.3)e11	(6.1±0.8)e9
5LE23	CSC	FAR	Phase II	13.5±1.1	(5.69±0.03)e11	(1.14±0.05)e10
5RE23	CSC	NEAR	Phase II	13.5±1.1	(5.69±0.03)e11	(1.14±0.05)e10
5LE24	CSC	FAR	Phase II	13.5±1.1	(5.69±0.03)e11	(1.14±0.05)e10
5RE24	CSC	NEAR	Phase II	13.5±1.1	(5.69±0.03)e11	(1.14±0.05)e10
5LE25	X5	BL	Phase II	5.5±0.4	(2.7±0.02)e11	(6.55±0.03)e9
5RE25	X0	BL	Phase II	6.9±0.8	(2.545±0.02)e11	(7.1±0.02)e9
5RE26	X5	BL	Phase II	3.2±0.6	(1.51±0.02)e11	(3.65±0.22)e9
5LE26	X0	BL	Phase II	1.47±0.15	(4.66±0.6)e10	(1.6±0.1)e9

CMS geometry version 6.0.0.1

5RE21	CSC	FAR	Phase II	4.4±0.3	(2.22±0.02)e11	(1.78±0.03)e10
5LE21	CSC	FAR	Phase II	4.4±0.3	(2.22±0.02)e11	(1.78±0.03)e10
5LE22	CSC	NEAR	Phase II	4.4±0.3	(2.22±0.02)e11	(1.78±0.03)e10
5RE22	CSC	NEAR	Phase II	4.4±0.3	(2.22±0.02)e11	(1.78±0.03)e10
5LE23	CSC	FAR	Phase II	12.4±0.08	(6.09±0.03)e11	(1.27±0.01)e11
5RE23	CSC	NEAR	Phase II	12.4±0.08	(6.09±0.03)e11	(1.27±0.01)e11
5LE24	CSC	FAR	Phase II	12.4±0.08	(6.09±0.03)e11	(1.27±0.01)e11
5RE24	CSC	NEAR	Phase II	12.4±0.08	(6.09±0.03)e11	(1.27±0.01)e11
5LE25	X5	BL	Phase II	7.2±0.9	(2.88±0.2)e11	(4.18±0.6)e10
5RE25	X0	BL	Phase II	6.8±0.5	(2.54±0.02)e11	(3.64±0.05)e10
5RE26	X5	BL	Phase II	3.9±0.2	(1.59±0.01)e11	(4.65±0.19)e9
5LE26	X0	BL	Phase II	1.6±0.2	(5.18±0.07)e10	(1.2±0.1)e9

Table 17: Extracted values of absorbed dose D, 1 MeV neutron equivalent fluence in Si $\Phi_{neq}^{1\ MeV}$ and fluence of hadrons with energy grater than 20 MeV Φ_{HEH} in LHC Radmon detector provided locations for Run 3 (5.0.0.3) and Run 4 (6.0.0.1) geometry versions. All values are normalised per 4000 fb^{-1}.

CMS geometry version 6.0.0.1

ID	Level	Side	D [Gy]	$\Phi_{neq}^{1\ MeV}[\mathrm{cm}^{-2}]$	$\Phi_{HEH}[\mathrm{cm}^{-2}]$	$\Phi_{neut}[\mathrm{cm}^{-2}]$	$\Phi_{neut}^{th}[\mathrm{cm}^{-2}]$
NMSP1	HFTOP	-Z	23.5±1.5	(1.010±0.03)e12	(2.21±0.02)e11	(1.915±0.003)e12	(2.657±.014)e11
NMSP2	HFTOP	+Z	140.5±1	(7.75±0.01)e12	(5.24±0.02)e11	(1.814±0.003)e12	(2.365±0.014)e11
NMSP3	X4	+Z	7.85±0.25	(5.085±0.035)e11	(9.24±0.07)e11	(1.274±0.003)e12	(3.015±0.015)e11
NMSP4	X1	+Z	9.4±0.6	(4.835±0.020)e11	(8.10±0.08)e10	(1.288±0.003)e12	(2.817±0.014)e11

CMS geometry version 5.0.0.3

NMSP1	HFTOP	-Z	25.7±1.4	(1.095±0.004)e12	(2.425±0.010)e11	(1.975±0.004)e12	(2.620±0.015)e11
NMSP2	HFTOP	+Z	105.4±1.2	(5.204±0.010)e12	(3.685±0.015)e11	(4.489±0.004)e13	(3.320±0.012)e11
NMSP3	X4	+Z	11.6±0.7	(5.25±0.03)e11	(9.940±0.063)e11	(1.294±0.003)e12	(3.067±0.004)e11
NMSP4	X1	+Z	8.8±0.7	(5.025±0.025)e11	(8.48±0.08)e10	(1.264±0.003)e12	(2.670±0.015)e11

Table 18: Extracted values of absorbed dose D, 1 MeV neutron equivalent fluence in Si $\Phi_{neq}^{1\ MeV}$, fluence of hadrons with energy grater than 20 MeV Φ_{HEH}, neutron fluence Φ_{neut} and thermal neutron fluence Φ_{neut}^{th} in Bonner Sphere with SiMP detector provided locations for Run 3 (5.0.0.3) and Run 4 (6.0.0.1) geometry versions. All values are normalised per 4000 fb^{-1}.

ID	Level	End	D [Gy]	$\Phi_{neq}^{1\ MeV}$[cm^{-2}]	Φ_{HEH}[cm^{-2}]	Φ_{neut}[cm^{-2}]	Φ_{neut}^{th}[cm^{-2}]
NMX3IPNEAR	X3	NEAR	3.2±0.3	(1.325±0.010)e11	(6.3±0.2)e9	(6.055±0.002)e11	(1.915±0.010)e11
NMX3IPFAR	X3	FAR	3.2±0.3	(1.325±0.010)e11	(6.3±0.2)e9	(6.055±0.002)e11	(1.915±0.010)e11
NMIPYB0TOP	YB0TOP	BL	3.4±0.4	(1.206±0.010)e11	(2.3±0.1)e9	(6.535±0.002)e11	(2.285±0.015)e11
NMIPFLOOR	X0	BL	0.05±0.01	(1.70±1.5)e9	(1.1±0.3)e8	(7.65±0.28)e9	(1.97±0.15)e9
NMYE3PFAR	YE3TOP	FAR	1.7±0.3	(4.95±0.20)e10	(1.15±0.20)e9	(3.20±0.03)e11	(1.12±0.03)e11
NMYE3PNEAR	YE3TOP	NEAR	1.7±0.3	(4.95±0.20)e10	(1.15±0.20)e9	(3.20±0.03)e11	(1.12±0.03)e11
NMYE3NFAR	YE3TOP	FAR	1.7±0.3	(4.95±0.20)e10	(1.15±0.20)e9	(3.20±0.03)e11	(1.12±0.03)e11
NMYE3NNEAR	YE3TOP	NEAR	1.7±0.3	(4.95±0.20)e10	(1.15±0.20)e9	(3.20±0.03)e11	(1.12±0.03)e11
NMBHP	BH	BL	19.1±0.9	(1.97±0.03)e11	(1.575±0.015)e11	(1.283±0.005)e12	(4.38±0.03)e11
NMBHN	BH	BL	19.1±0.9	(1.97±0.03)e11	(1.575±0.015)e11	(1.283±0.005)e12	(4.38±0.03)e11
NMBHRSP	BH	BL	42.5±1.5	(1.111±0.003)e12	(3.675±0.01)e11	(2.049±0.004)e12	(4.045±0.020)e11
NMBHRSN	BH	BL	42.5±1.5	(1.111±0.003)e12	(3.675±0.01)e11	(2.049±0.004)e12	(4.045±0.020)e11
NMX1PFAR	X1	FAR	18±1	(6.61±0.4)e11	(1.53±0.01)e11	(1.803±0.005)e12	(5.235±0.025)e11
NMX2PFAR	X2	FAR	11.4±1.1	(4.32±0.03)e11	(7.89±0.08)e10	(1.237±0.004)e12	(3.465±0.020)e11
NMX4PFAR	X4	FAR	16.5±1.5	(5.62±0.03)e11	(1.24±0.01)e11	(1.462±0.004)e12	(1.242±0.011)e11
NMX1NFAR	X1	FAR	18±1	(6.61±0.4)e11	(1.53±0.01)e11	(1.803±0.005)e12	(5.235±0.025)e11
NMX2NFAR	X2	FAR	11.4±1.1	(4.32±0.03)e11	(7.89±0.08)e10	(1.237±0.004)e12	(3.465±0.020)e11
NMX4NFAR	X4	FAR	16.5±1.5	(5.62±0.03)e11	(1.24±0.01)e11	(1.462±0.004)e12	(1.242±0.011)e11
NMX1PNEAR	X1	NEAR	18±1	(6.61±0.4)e11	(1.53±0.01)e11	(1.803±0.005)e12	(5.235±0.025)e11
NMX2PNEAR	X2	NEAR	11.4±1.1	(4.32±0.03)e11	(7.89±0.08)e10	(1.237±0.004)e12	(3.465±0.020)e11
NMX4PNEAR	X4	NEAR	16.5±1.5	(5.62±0.03)e11	(1.24±0.01)e11	(1.462±0.004)e12	(1.242±0.011)e11
NMX1NNEAR	X1	NEAR	18±1	(6.61±0.4)e11	(1.53±0.01)e11	(1.803±0.005)e12	(5.235±0.025)e11
NMX2NNEAR	X2	NEAR	11.4±1.1	(4.32±0.03)e11	(7.89±0.08)e10	(1.237±0.004)e12	(3.465±0.020)e11
NMX4NNEAR	X4	NEAR	16.5±1.5	(5.62±0.03)e11	(1.24±0.01)e11	(1.462±0.004)e12	(1.242±0.011)e11

Table 19: Extracted values of absorbed dose D, 1 MeV neutron equivalent fluence in Si $\Phi_{neq}^{1\ MeV}$, fluence of hadrons with energy grater than 20 MeV Φ_{HEH}, neutron fluence Φ_{neut} and thermal neutron fluence Φ_{neut}^{th} in Bonner Sphere with GFPC full detector provided locations for Run 3 (5.0.0.3) geometry version. All values are normalised per 4000 fb^{-1}.

ID	Level	End	D [Gy]	$\Phi_{neq}^{1\ MeV}[\mathrm{cm}^{-2}]$	$\Phi_{HEH}[\mathrm{cm}^{-2}]$	$\Phi_{neut}[\mathrm{cm}^{-2}]$	$\Phi_{neut}^{th}[\mathrm{cm}^{-2}]$
NMX3IPNEAR	X3	NEAR	3.4±0.2	(1.269±0.010)e11	(5.75±0.25)e9	(5.895±0.020)e11	(1.880±0.015)e11
NMX3IPFAR	X3	FAR	3.4±0.2	(1.269±0.010)e11	(5.75±0.25)e9	(5.895±0.020)e11	(1.880±0.015)e11
NMIPYB0TOP	YB0TOP	BL	2.80±0.15	(1.245±0.010)e11	(2.45±0.15)e9	(6.525±0.025)e11	(2.34±0.01)e11
NMIPFLOOR	X0	BL	0.46±0.09	(2.79±0.05)e10	(8.4±0.9)e8	(1.265±0.010)e11	(2.46±0.05)e10
NMYE3PFAR	YE3TOP	FAR	1.68±0.31	(4.96±0.12)e10	(1.15±0.05)e9	(3.21±0.04)e11	(1.12±0.03)e11
NMYE3PNEAR	YE3TOP	NEAR	1.68±0.31	(4.96±0.12)e10	(1.15±0.05)e9	(3.21±0.04)e11	(1.12±0.03)e11
NMYE3NFAR	YE3TOP	FAR	1.68±0.31	(4.96±0.12)e10	(1.15±0.05)e9	(3.21±0.04)e11	(1.12±0.03)e11
NMYE3NNEAR	YE3TOP	NEAR	1.68±0.31	(4.96±0.12)e10	(1.15±0.05)e9	(3.21±0.04)e11	(1.12±0.03)e11
NMBHP	BH	BL	23.8±1.9	(5.71±0.025)e11	(1.622±0.012)e11	(1.527±0.035)e12	(4.59±0.02)e11
NMBHN	BH	BL	23.8±1.9	(5.71±0.025)e11	(1.622±0.012)e11	(1.527±0.035)e12	(4.59±0.02)e11
NMBHRSP	BH	BL	40.0±1.5	(1.038±0.004)e12	(3.42±0.02)e11	(1.948±0.004)e12	(3.795±0.006)e11
NMBHRSN	BH	BL	40.0±1.5	(1.038±0.004)e12	(3.42±0.02)e11	(1.948±0.004)e12	(3.795±0.006)e11
NMX1PFAR	X1	FAR	21.2±0.8	(6.96±0.03)e11	(1.605±0.010)e11	(1.796±0.004)e12	(4.655±0.020)e11
NMX2PFAR	X2	FAR	10.8±1.0	(4.81±0.02)e11	(8.64±0.08)e10	(1.284±0.030)e12	(3.140±0.015)e11
NMX4PFAR	X4	FAR	16.4±1.0	(6.57±0.03)e11	(1.425±0.013)e11	(1.601±0.040)e12	(3.815±0.020)e11
NMX1NFAR	X1	FAR	21.2±0.8	(6.96±0.03)e11	(1.605±0.010)e11	(1.796±0.004)e12	(4.655±0.020)e11
NMX2NFAR	X2	FAR	10.8±1.0	(4.81±0.02)e11	(8.64±0.08)e10	(1.284±0.030)e12	(3.140±0.015)e11
NMX4NFAR	X4	FAR	16.4±1.0	(6.57±0.03)e11	(1.425±0.013)e11	(1.601±0.040)e12	(3.815±0.020)e11
NMX1PNEAR	X1	NEAR	21.2±0.8	(6.96±0.03)e11	(1.605±0.010)e11	(1.796±0.004)e12	(4.655±0.020)e11
NMX2PNEAR	X2	NEAR	10.8±1.0	(4.81±0.02)e11	(8.64±0.08)e10	(1.284±0.030)e12	(3.140±0.015)e11
NMX4PNEAR	X4	NEAR	16.4±1.0	(6.57±0.03)e11	(1.425±0.013)e11	(1.601±0.040)e12	(3.815±0.020)e11
NMX1NNEAR	X1	NEAR	21.2±0.8	(6.96±0.03)e11	(1.605±0.010)e11	(1.796±0.004)e12	(4.655±0.020)e11
NMX2NNEAR	X2	NEAR	10.8±1.0	(4.81±0.02)e11	(8.64±0.08)e10	(1.284±0.030)e12	(3.140±0.015)e11
NMX4NNEAR	X4	NEAR	16.4±1.0	(6.57±0.03)e11	(1.425±0.013)e11	(1.601±0.040)e12	(3.815±0.020)e11

Table 20: Extracted values of absorbed dose D, 1 MeV neutron equivalent fluence in Si $\Phi_{neq}^{1\ MeV}$, fluence of hadrons with energy grater than 20 MeV Φ_{HEH}, neutron fluence Φ_{neut} and thermal neutron fluence Φ_{neut}^{th} in Bonner Sphere with GFPC full detector provided locations for Run 4 (6.0.0.1) geometry version. All values are normalised per 4000 fb^{-1}.

CMS geometry version 5.0.0.3

ID	Level	End	D [Gy]	$\Phi_{neq}^{1\ MeV}[\mathrm{cm}^{-2}]$	$\Phi_{HEH}[\mathrm{cm}^{-2}]$	$\Phi_{neut}[\mathrm{cm}^{-2}]$	$\Phi_{neut}^{th}[\mathrm{cm}^{-2}]$
PFXT1	HF RACKS	FAR	23.9±1.5	(9.23±0.05)e11	(1.88±0.01)e11	(1.836±0.006)e12	(2.22±0.03)e11
PFXT2	HF RACKS	FAR	15.4±0.5	(8.39±0.04)e11	(1.11±0.01)e11	(2.89±0.01)e12	(6.55±0.03)e11
PNXB1	HF RACKS	NEAR	23.7±1.3	(9.51±0.03)e11	(1.98±0.02)e11	(1.87±0.01)e12	(2.29±0.02)e11
PNXB2	HF RACKS	NEAR	15.4±0.5	(8.39±0.04)e11	(1.11±0.01)e11	(2.89±0.01)e12	(6.55±0.03)e11
MFXT1	HF RACKS	FAR	23.7±1.3	(9.51±0.03)e11	(1.98±0.02)e11	(1.87±0.01)e12	(2.29±0.02)e11
MFXT2	HF RACKS	FAR	15.4±0.5	(8.39±0.04)e11	(1.11±0.01)e11	(2.89±0.01)e12	(6.55±0.03)e11
MNXB1	HF RACKS	NEAR	24.5±1.2	(1.02±0.01)e12	(2.02±0.02)e11	(2.06±0.01)e12	(1.88±0.01)e11
MNXB2	HF RACKS	NEAR	15.4±0.5	(8.39±0.04)e11	(1.11±0.01)e11	(2.89±0.01)e12	(6.55±0.03)e11

CMS geometry version 6.0.0.1

PFXT1	HF RACKS	FAR	23.9±1.5	(9.23±0.05)e11	(1.88±0.01)e11	(1.836±0.006)e12	(2.22±0.03)e11
PFXT2	HF RACKS	FAR	15.4±0.5	(8.39±0.04)e11	(1.11±0.01)e11	(2.89±0.01)e12	(6.55±0.03)e11
PNXB1	HF RACKS	NEAR	23.7±1.3	(9.51±0.03)e11	(1.98±0.02)e11	(1.87±0.01)e12	(2.29±0.02)e11
PNXB2	HF RACKS	NEAR	15.4±0.5	(8.39±0.04)e11	(1.11±0.01)e11	(2.89±0.01)e12	(6.55±0.03)e11
MFXT1	HF RACKS	FAR	23.7±1.3	(9.51±0.03)e11	(1.98±0.02)e11	(1.87±0.01)e12	(2.29±0.02)e11
MFXT2	HF RACKS	FAR	15.4±0.5	(8.39±0.04)e11	(1.11±0.01)e11	(2.89±0.01)e12	(6.55±0.03)e11
MNXB1	HF RACKS	NEAR	24.5±1.2	(1.02±0.01)e12	(2.02±0.02)e11	(2.06±0.01)e12	(1.88±0.01)e11
MNXB2	HF RACKS	NEAR	15.4±0.5	(8.39±0.04)e11	(1.11±0.01)e11	(2.89±0.01)e12	(6.55±0.03)e11

Table 21: Extracted values of absorbed dose D, 1 MeV neutron equivalent fluence in Si $\Phi_{neq}^{1\ MeV}$, fluence of hadrons with energy grater than 20 MeV Φ_{HEH}, neutron fluence Φ_{neut} and thermal neutron fluence Φ_{neut}^{th} in Bonner Sphere with GFPC light detector provided locations for Run 3 (5.0.0.3) and Run 4 (6.0.0.1) geometry versions. All values are normalised per 4000 fb^{-1}.

D Energy spectra in scoring region locations

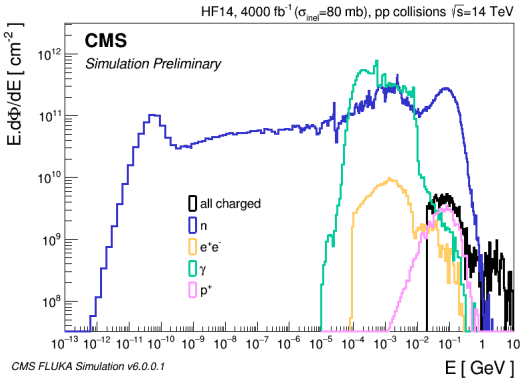

Figure 25: Energy spectra in scoring region HF14 normalised to 4000 fb^{-1} with Run 4 CMS FLUKA geometry.

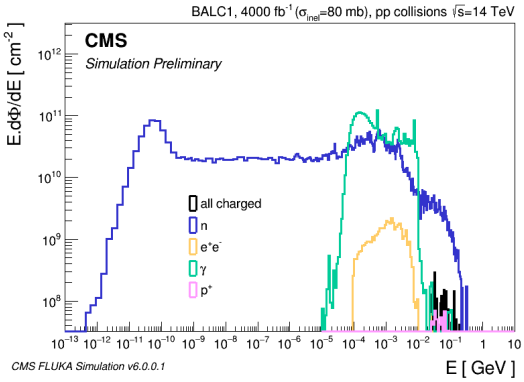

Figure 26: Energy spectra in scoring region BALC1 normalised to 4000 fb^{-1} with Run 4 CMS FLUKA geometry.

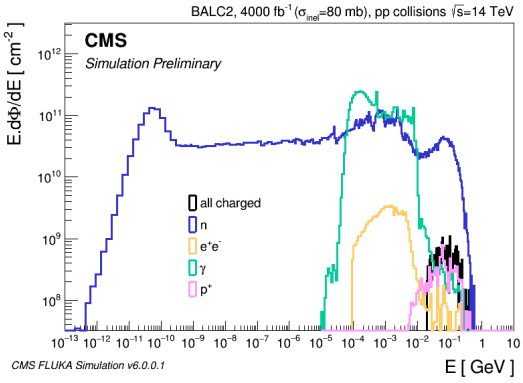

Figure 27: Energy spectra in scoring region BALC2 normalised to 4000 fb^{-1} with Run 4 CMS FLUKA geometry.

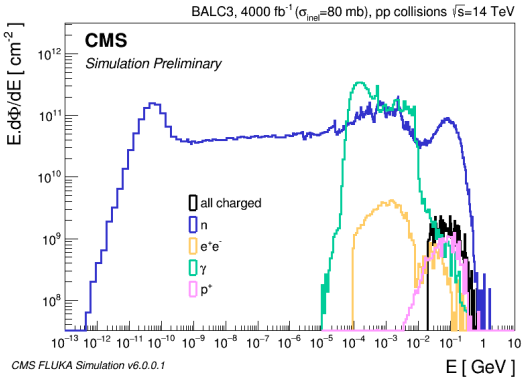

Figure 28: Energy spectra in scoring region BALC3 normalised to 4000 fb^{-1} with Run 4 CMS FLUKA geometry.

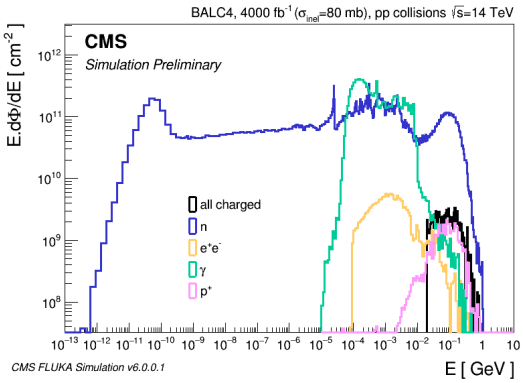

Figure 29: Energy spectra in scoring region BALC4 normalised to 4000 fb^{-1} with Run 4 CMS FLUKA geometry.

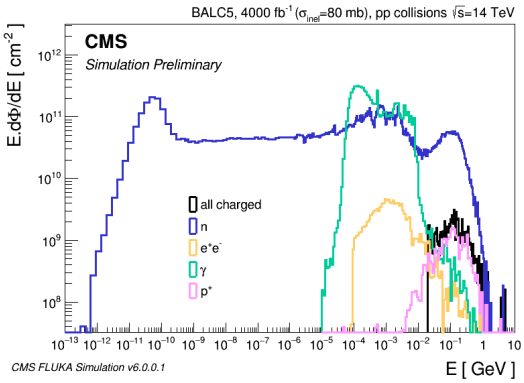

Figure 30: Energy spectra in scoring region BALC5 normalised to 4000 fb^{-1} with Run 4 CMS FLUKA geometry.

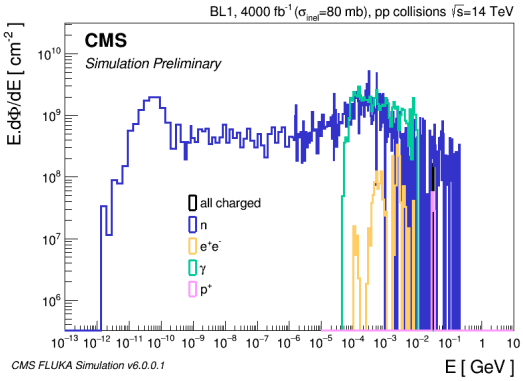

Figure 31: Energy spectra in scoring region BL1 normalised to 4000 fb^{-1} with Run 4 CMS FLUKA geometry.

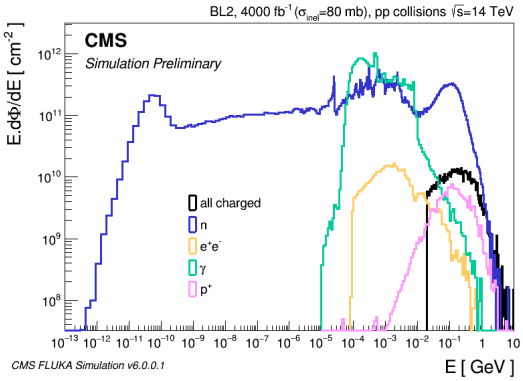

Figure 32: Energy spectra in scoring region BL2 normalised to 4000 fb^{-1} with Run 4 CMS FLUKA geometry.

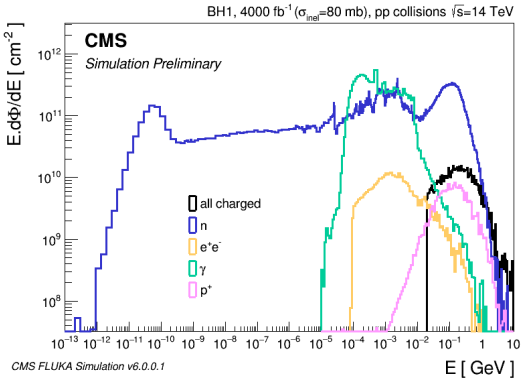

Figure 33: Energy spectra in scoring region BH1 normalised to 4000 fb^{-1} with Run 4 CMS FLUKA geometry.

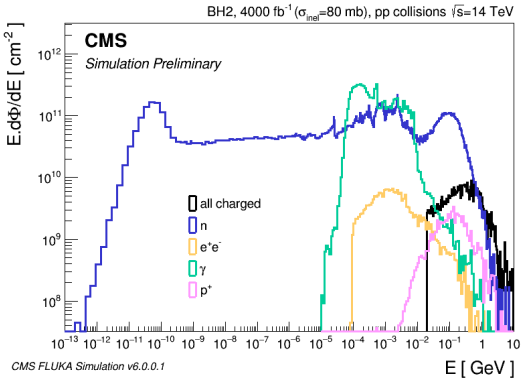

Figure 34: Energy spectra in scoring region BH2 normalised to 4000 fb^{-1} with Run 4 CMS FLUKA geometry.

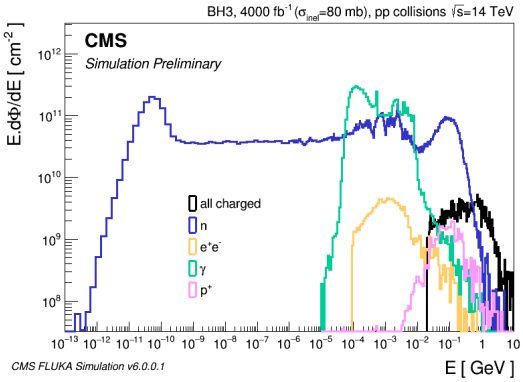

Figure 35: Energy spectra in scoring region BH3 normalised to 4000 fb^{-1} with Run 4 CMS FLUKA geometry.

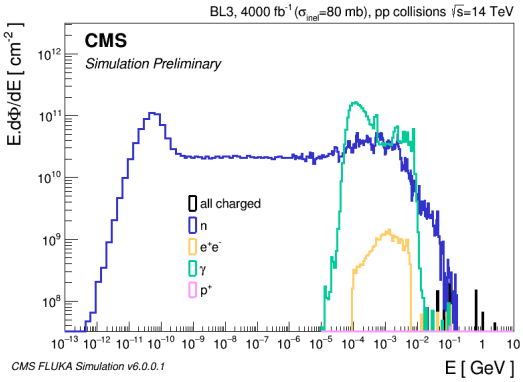

Figure 36: Energy spectra in scoring region BL3 normalised to 4000 fb^{-1} with Run 4 CMS FLUKA geometry.

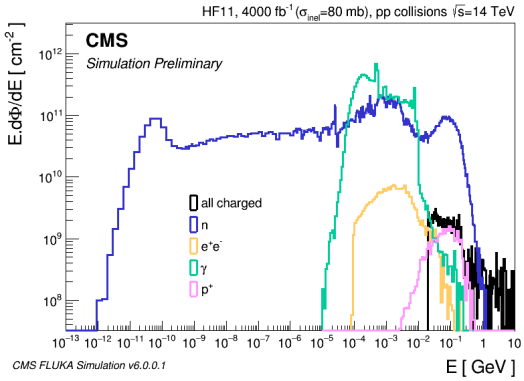

Figure 37: Energy spectra in scoring region HF11 normalised to 4000 fb^{-1} with Run 4 CMS FLUKA geometry.

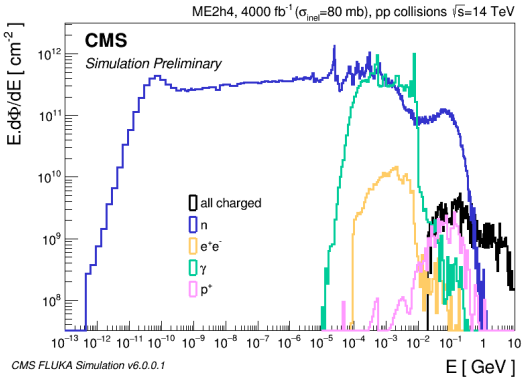

Figure 38: Energy spectra in scoring region ME2h4 normalised to 4000 fb^{-1} with Run 4 CMS FLUKA geometry.

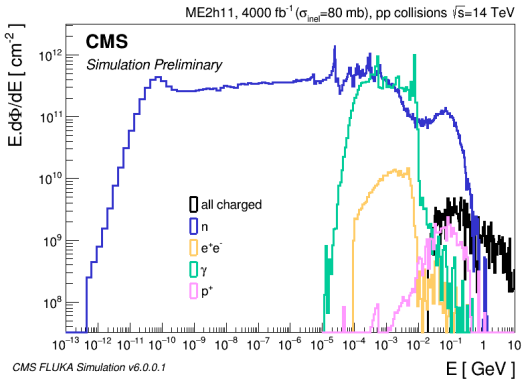

Figure 39: Energy spectra in scoring region ME2h11 normalised to 4000 fb^{-1} with Run 4 CMS FLUKA geometry.

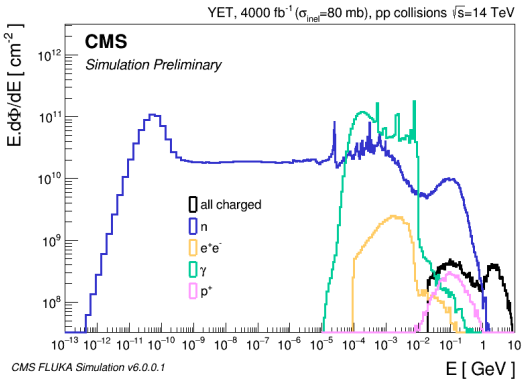

Figure 40: Energy spectra in scoring region YET normalised to 4000 fb^{-1} with Run 4 CMS FLUKA geometry.

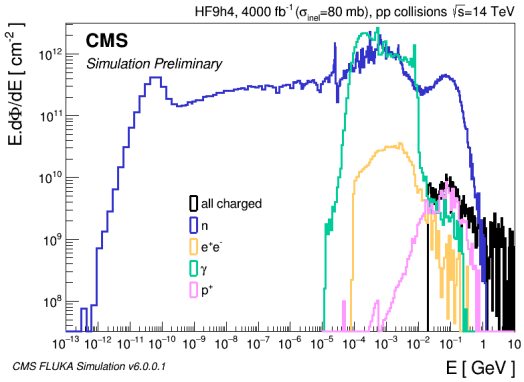

Figure 41: Energy spectra in scoring region HF9h4 normalised to 4000 fb^{-1} with Run 4 CMS FLUKA geometry.

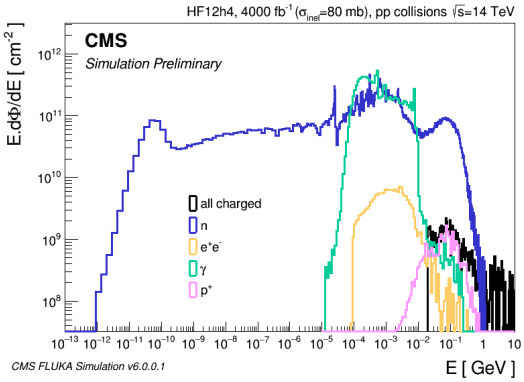

Figure 42: Energy spectra in scoring region HF12h4 normalised to 4000 fb^{-1} with Run 4 CMS FLUKA geometry.

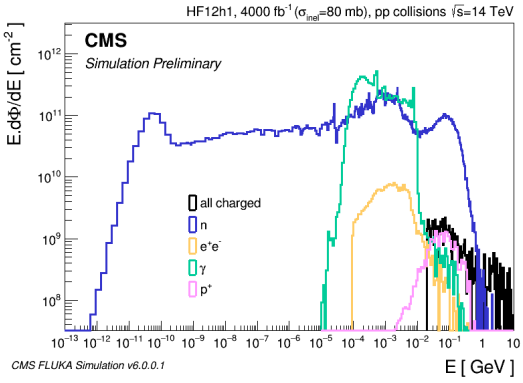

Figure 43: Energy spectra in scoring region HF12h1 normalised to 4000 fb^{-1} with Run 4 CMS FLUKA geometry.

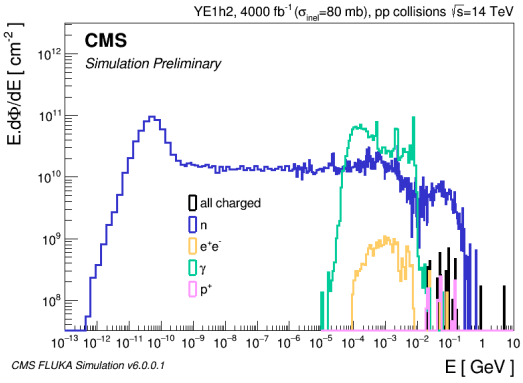

Figure 44: Energy spectra in scoring region YE1h2 normalised to 4000 fb^{-1} with Run 4 CMS FLUKA geometry.

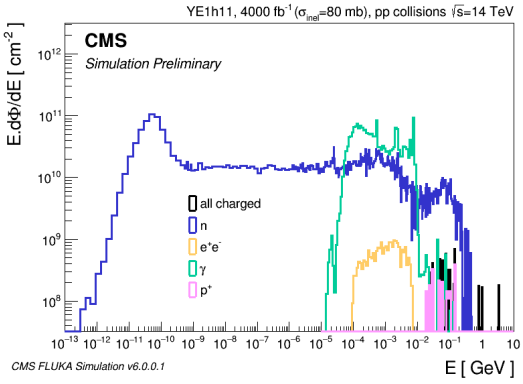

Figure 45: Energy spectra in scoring region YE1h11 normalised to 4000 fb^{-1} with Run 4 CMS FLUKA geometry.

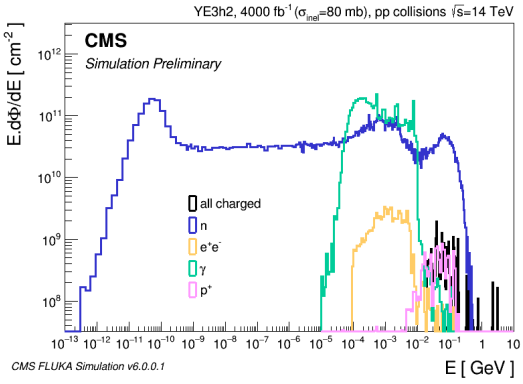

Figure 46: Energy spectra in scoring region YE3h2 normalised to 4000 fb^{-1} with Run 4 CMS FLUKA geometry.

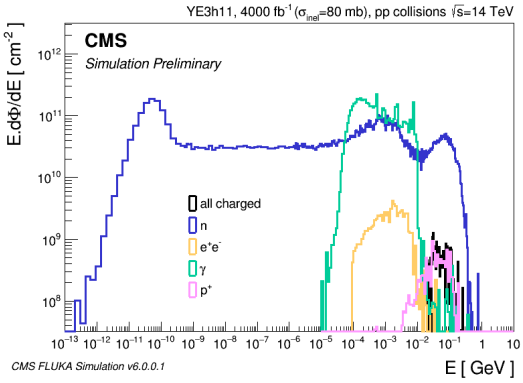

Figure 47: Energy spectra in scoring region YE3h11 normalised to 4000 fb^{-1} with Run 4 CMS FLUKA geometry.

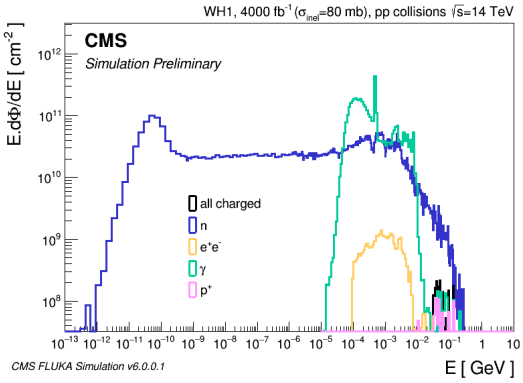

Figure 48: Energy spectra in scoring region WH1 normalised to 4000 fb^{-1} with Run 4 CMS FLUKA geometry.